Observatório Nacional

Divisão de Programas de Pós-Graduação

GEOELECTRICAL IMAGING OF THE PARNAÍBA BASIN USING DETERMINISTIC AND BAYESIAN MAGNETOTELLURIC INVERSION

Gonzalo Gadafi Romero Beltran

Tese apresentada ao Programa de Pós-graduação em Geofísica do Observatório Nacional, como parte dos requisitos necessários à obtenção do título de Doutor em Geofísica.

Orientador(a): Dr. Emanuele F. La Terra

Co-orientadores: Dra. Liliane P. Panetto
(ON - Brazil)
Dr. Hoël Seillé
(CSIRO - Australia)

Rio de Janeiro
Julho de 2026

In memory of my mother, Deizy Beltran

Acknowledgements

I would like to express my sincere gratitude to all the colleagues who have supported me throughout these years. Although it is impossible to mention them all, I would like to take this opportunity to acknowledge those who have been especially important during the past few years.

I would like to express my deepest gratitude to my supervisor, Emanuele F. La Terra, for his continuous guidance, valuable advice, and unwavering support throughout my doctoral studies. His constant availability and open-door attitude were essential for my academic development, and he also gave me the opportunity to actively engage in research from the very beginning of my arrival in Brazil.

I am also very grateful to my first co-supervisor, Liliane P. Panetto, for her constant support, guidance, and valuable contributions, which were fundamental for the rigorous processing of the magnetotelluric data.

I would also like to thank my second co-supervisor, Hoël Seillé, for his critical insights, detailed comments, and academic rigor, which significantly strengthened my professional development. His guidance helped me to become more rigorous in data analysis, and I learned a great deal from him about magnetotellurics in general. I am especially thankful to him for hosting me at the CSIRO facilities in Perth, Australia, during my PhD stay. This experience was invaluable, not only for advancing my knowledge in Bayesian inversion methods but also on a personal level, through the shared experiences, travels, and memorable moments.

Finally, I would like to thank my family for their love, support, and encouragement throughout my life. To my father and my siblings, Nikolai, Varoski, Amilcar, and Stefany, for always being there. And especially to my wife, Rossi, for her patience, understanding, and constant support, even during the most demanding periods of my research, when long hours of work kept me at home. Thank you for giving me the greatest gift of my life—our son, Leandro, who is now our greatest motivation.

Abstract of the Thesis presented to the National Observatory's Graduate Program in Geophysics as a partial fulfillment of the requirements for the degree of Doctor in Geophysics.

GEOELECTRICAL IMAGING OF THE PARNAÍBA BASIN USING DETERMINISTIC AND BAYESIAN MAGNETOTELLURIC INVERSION

Gonzalo Gadafi Romero Beltran

Julho/2026

The objective of this thesis is to improve the understanding of the internal structure and tectonic framework of the Parnaíba Basin by applying the magnetotelluric (MT) method, within the framework of the Parnaíba Basin Analysis Project (PBAP). The Parnaíba Basin is located in northeastern Brazil, where a thick Phanerozoic sedimentary sequence covers most of the basin, and the presence of magmatic intrusions represents a key element in the geodynamic evolution of the basin.

The MT dataset used in this research consists of 218 broadband magnetotelluric (BBMT) stations and 37 long-period magnetotelluric (LMT) stations, distributed along a profile crossing the basin in an E–W direction. The data were analyzed and processed using robust techniques, ensuring the quality and reliability of the resulting magnetotelluric responses. Subsequently, the data were modeled and inverted using both deterministic and probabilistic inversion methodologies. In this context, this thesis is organized into two main parts, each focusing on the characterization of the deep structure of the Parnaíba Basin at different scales of analysis.

The first part consists of obtaining crustal-scale resistivity models through 3D deterministic inversion strategies. The inversion results reveal the presence of three contiguous lithospheric blocks that constitute the Parnaíba Basin. From west to east, these correspond to the Amazonian Craton, the Parnaíba Block, and the Borborema Province, separated by lithospheric-scale resistive discontinuities. Within each block, the models display distinct geoelectrical characteristics. The Amazonian Craton exhibits a conductive domain, possibly associated with the replacement or modification of a previously delaminated lithosphere. The Parnaíba Block, in turn,

is composed of two distinct tectonic domains: the highly resistive Grajaú Block and the more conductive Teresina Block. This resistivity contrast is primarily related to magmatic activity, which is more pronounced in the Teresina domain, although it may also be influenced by Cretaceous extensional events associated with the opening of the South Atlantic Ocean. In the Borborema Province, resistive and conductive signatures observed at lower crustal depths provide evidence of collisional processes associated with its Neoproterozoic formation. Overall, these deep resistivity models provide new insights into the crustal amalgamation of the Parnaíba Basin and contribute to a better understanding of the tectonic processes that shaped Western Gondwana.

The second part of this research focuses on the characterization of the shallow structure of the basin ($\sim$ 3–4 km depth) through the application of 1D Bayesian trans-dimensional inversion approaches based on Markov chain Monte Carlo (MCMC), which allow uncertainties associated with non-1D effects in the data to be properly accounted for. Furthermore, by integrating magnetotelluric data with structural information and well data, and through the application of the Bayesian Estimate Fusion (BEF) approach, it was possible to construct a robust model of basement geometry.

This approach also enabled the identification of the sedimentary cover-basement interface, as well as highly conductive anomalies within the sedimentary sequence, particularly associated with the Poti and Cabeças formations, which are linked to hydrocarbon reservoirs in the Parnaíba Basin. These results provide a more detailed view of the shallow architecture of the basin and its economic potential.

Overall, the results obtained in this thesis significantly contribute to the understanding of both the deep and shallow structure of the Parnaíba Basin, providing key insights into its tectonic evolution as well as valuable information for future hydrocarbon exploration.

Resumo da Tese apresentada Abstract of the Thesis presented ao Programa de Pós-Graduação em Geofísica do Observatório Nacional como parte dos requisitos necessários para a obtenção do título de Doutor em Geofísica.

IMAGEAMENTO GEOELÉTRICO DA BACIA DO PARNAÍBA POR MEIO DA INVERSÃO MAGNETOTELÚRICA DETERMINÍSTICA E BAYESIANA

Gonzalo Gadafi Romero Beltran

July/2026

O objetivo desta tese é aprimorar a compreensão da estrutura interna e do contexto tectônico da Bacia do Parnaíba por meio da aplicação do método magnetotelúrico (MT), no âmbito do Projeto de Análise da Bacia do Parnaíba (PBAP). A Bacia do Parnaíba está localizada no nordeste do Brasil, onde uma espessa sequência sedimentar fanerozoica recobre a maior parte da bacia, e a presença de intrusões magmáticas representa um elemento-chave na sua evolução geodinâmica.

O conjunto de dados MT utilizado nesta pesquisa é composto por 218 estações magnetotelúricas de banda larga (BBMT) e 37 estações magnetotelúricas de longo período (LMT), distribuídas ao longo de um perfil que atravessa a bacia na direção leste-oeste (E–W). Os dados foram analisados e processados por meio de técnicas robustas, garantindo a qualidade e a confiabilidade das respostas magnetotelúricas obtidas. Posteriormente, foram modelados e invertidos utilizando metodologias de inversão tanto determinísticas quanto probabilísticas. Nesse contexto, esta tese está organizada em duas partes principais, cada uma voltada à caracterização da estrutura da Bacia do Parnaíba em diferentes escalas de análise.

A primeira parte consiste na obtenção de modelos de resistividade em escala crustal por meio de estratégias de inversão determinística tridimensional (3D). Os resultados da inversão revelam a presença de três blocos litosféricos contíguos que compõem a Bacia do Parnaíba. De oeste para leste, esses blocos correspondem ao Cráton Amazônico, ao Bloco Parnaíba e à Província Borborema, separados por descontinuidades resistivas em escala litosférica. Em cada bloco, os modelos apresentam características geoelétricas distintas. O Cráton Amazônico exibe um domínio condutivo, possivelmente associado à substituição ou modificação de uma

litosfera previamente delaminada. O Bloco Parnaíba, por sua vez, é constituído por dois domínios tectônicos distintos: o Bloco Grajaú, altamente resistivo, e o Bloco Teresina, mais condutivo. Esse contraste de resistividade está relacionado principalmente à atividade magmática, mais intensa no domínio Teresina, embora também possa ter sido influenciado pelos eventos extensionais do Cretáceo associados à abertura do Oceano Atlântico Sul. Na Província Borborema, as assinaturas resistivas e condutivas observadas em profundidades correspondentes à crosta inferior fornecem evidências de processos colisionais associados à sua formação durante o Neoproterozoico. Em conjunto, esses modelos profundos de resistividade fornecem novos insights sobre a amalgamação crustal da Bacia do Parnaíba e contribuem para uma melhor compreensão dos processos tectônicos responsáveis pela formação do Gondwana Ocidental.

A segunda parte desta pesquisa concentra-se na caracterização da estrutura rasa da bacia ($\sim$ 3–4 km de profundidade) por meio da aplicação de algoritmos de inversão Bayesiana unidimensional (1D), especificamente abordagens transdimensionais baseadas em Cadeias de Markov Monte Carlo (MCMC), que permitem considerar adequadamente as incertezas associadas aos efeitos não unidimensionais presentes nos dados. Além disso, por meio da integração de dados magnetotelúricos com informações estruturais e dados de poços, e da aplicação da abordagem Bayesian Estimate Fusion (BEF), foi possível construir um modelo robusto da geometria do embasamento.

Essa abordagem também possibilitou identificar a interface entre a cobertura sedimentar e o embasamento, bem como anomalias altamente condutivas no interior da sequência sedimentar, particularmente associadas às formações Poti e Cabeças, que estão relacionadas a reservatórios de hidrocarbonetos na Bacia do Parnaíba. Esses resultados fornecem uma visão mais detalhada da arquitetura rasa da bacia e de seu potencial econômico.

De modo geral, os resultados obtidos nesta tese contribuem significativamente para a compreensão tanto da estrutura profunda quanto da estrutura rasa da Bacia do Parnaíba, fornecendo informações fundamentais sobre sua evolução tectônica e uma base sólida para futuras atividades de exploração de hidrocarbonetos.

Contents

1 Introduction **1**

1.1 Thesis structure . . . 3

2 The Magnetotelluric method **4**

2.1 Governing Equations . . . 5

2.2 The Impedance Tensor . . . 9

2.3 Magnetotelluric models of Earth induction . . . 9

2.4 Transfer function estimation . . . 10

2.4.1 Least square method . . . 11

2.4.2 Robust Processing . . . 12

2.5 MT data analysis . . . 14

2.5.1 Processing MT data . . . 14

2.5.2 Dimensionality and directionality analysis . . . 16

2.5.3 Strike Analysis . . . 16

2.6 MT data inversion . . . 19

2.6.1 Deterministic Inversion . . . 20

2.6.1.1 Limitation of Deterministic inversion . . . 23

2.6.2 Probabilistic inversion method . . . 24

2.6.2.1 1D Bayesian inversion . . . 26

2.6.2.2 Bayesian Estimate Fusion . . . 29

3 Tectonic and Geological Setting **32**

3.1 West Gondwana Orogen . . . 32

3.2 Geological contexts . . . 34

3.3 Parnaíba basement . . . 36

4 Magnetotelluric imaging of the Parnaíba Basin: Implications to the West Gondwana formation **39**

4.0.1 General Outline . . . 39

4.0.2 Scientific Paper 1 . . . 39

5 Structure of the Parnaíba Basin inferred from Bayesian inversion of magnetotelluric data 69

5.0.1 General Outline 69

5.0.2 Scientific Paper 2 69

6 Discussion, conclusion and future work 120

6.1 3D deterministic and 1D probabilistic models 120

6.2 Conclusion 123

6.3 Future Work 124

Bibliography 126

Chapter 1

Introduction

Magnetotellurics (MT) is a passive electromagnetic method that involves measuring fluctuations in the natural electric, E, and magnetic, H, fields in orthogonal directions at surface of the Earth as a mean of determining the conductivity structure of the Earth at depths ranging from a few tens of meters to several hundreds of kilometers (Simpson and Bahr, 2005). Conductivity in the crust and upper mantle is closely linked to the tectonic and magmatic evolution of the geological units that constitute them. Therefore, MT has been widely used to constrain deep architecture and to delineate distinct structural domains in cratons, intracratonic basins, and adjacent mobile belts (e.g., Padilha et al. 1992; Bologna et al., 2005; Panetto et al., 2018).

As part of the Parnaíba Basin Analysis Project (PBAP), a multidisciplinary project funded by BP-Brasil, the work presented in this thesis investigates the MT dataset acquired across the Parnaíba Basin. An approximately 1400 km long profile, oriented in an E–W direction and crossing the basin, was modeled in order to characterize its structure at crustal and upper mantle depths by deterministic three-dimensional (3D) inversion. The spatial distribution of the MT stations used in this study is presented in Figure 1.1.

In this thesis, the MT method has been used to characterize crustal-scale geoelectrical structures associated with the collision of different tectonic units that led to the formation of the Parnaíba Basin, within the context of the assembly of Western Gondwana. The results presented in this study are based on new MT data, as well as on a re-evaluation of MT study conducted by Solon et al. (2018). This re-evaluation was motivated by the availability of the complete MT dataset, including Broadband (BBMT) and Long-period (LMT) stations. In Solon et al. (2018), only a limited subset of long-period station data was considered.

The use of the full set of available stations in this study allows for the construction of resistivity models with significantly improved resolution along the entire profile. It also enables the identification of structures that could not be previously resolved due to the limited data coverage. In particular, the integration of BBMT and LMT data enhances sensitivity to both shallow and deep structures, allowing for a more comprehensive characterization of the subsurface.

The thesis also focuses on the characterization of the shallow structure ($\sim$ 3–4 km depth) of the sedimentary basin using 1D probabilistic inversion approaches ased on transdimensional MCMC schemes. The adopted methodology is described, and resistivity models are presented in integration with structural information and drillhole data, using the Bayesian Estimate Fusion (BEF) approach to construct a probabilistic model of the basement.

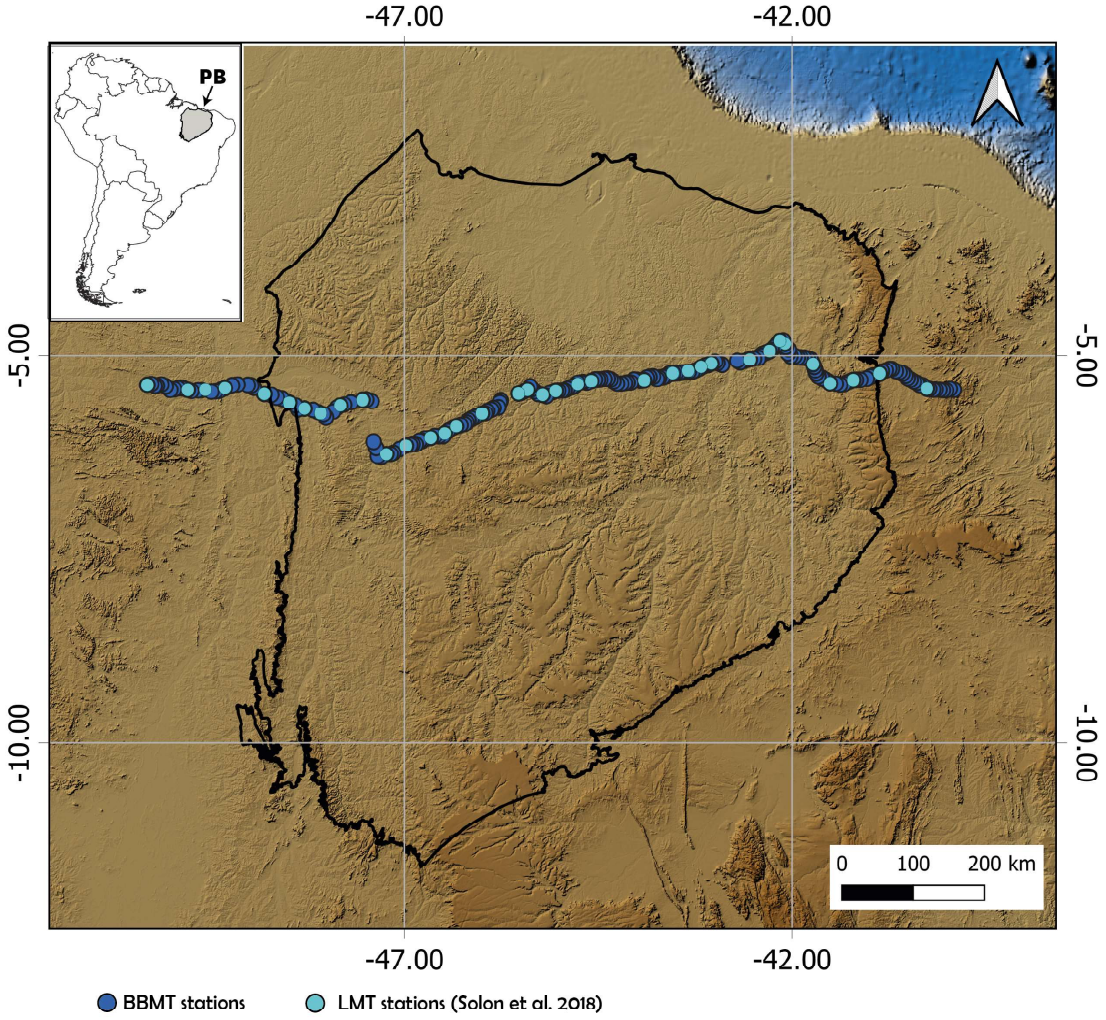


Figure 1.1: Location of the MT stations used in this thesis. The abbreviation PB in the South America reference map corresponds to the Parnaíba Basin.

1.1 Thesis structure

This thesis is structured as a compendium of two scientific articles, one of which has already been published and the second is currently under review. In both cases, the manuscripts have been submitted to international scientific journals indexed in the Journal Citation Reports (ISI).

The published article presents the application of the MT method to characterize the electrical structure of the Parnaíba Basin at crustal and lithospheric scales. The results reveal the coupling of three major tectonic units that compose the basin: the Amazonian Craton, the Parnaíba Block, and the Borborema Province. Each of these domains exhibits distinct resistivity signatures, reflecting differences in their geological evolution and providing insights into the tectonic and magmatic processes associated with the basin's development within the context of Western Gondwana.

The second article, currently under review, focuses on the study of the shallow structure of the basin through the application of Bayesian inversion techniques. This probabilistic approach enables a more accurate characterization of the sedimentary layers and the basement topography, overcoming the limitations inherent to traditional deterministic methods.

The first part presents the results obtained in the characterization of the electrical lithosphere of the Parnaíba Basin using BBMT and LMT data. In this study, previously proposed results by Solon et al. (2018) have been improved. The article associated with this study is: **Romero-Beltran, G.**, La Terra, E. F., Panetto, L. P., & Seillé, H. (2025). Magnetotelluric imaging of the Parnaíba Basin: Implications to the West Gondwana formation. Tectonophysics, 909, 230777.

The second part of the thesis presents the results from the MT study, but in this opportunity, through the application of Bayesian inversion processes and Bayesian Ensemble Fusion techniques. This approach has enabled the characterization of the shallow geo-electrical structures of the region, as well as the determination of the geometry of the sedimentary cover and the topography of the underlying basement. This study highlights the advantages of probabilistic inversion methods over deterministic approaches for the characterization of structures within a 1D domain, as is the case for the shallow levels of the Parnaíba Basin. The article associated with this study is: **Romero-Beltran, G.**, Seillé, H., La Terra, E., Panetto, L., &Visser, G., (2026). Structure of the Parnaíba Basin inferred from Bayesian inversion of MT data. Geophysical Journal International (Under review).

Chapter 2

The Magnetotelluric method

The magnetotelluric method or usually called MT is a passive electromagnetic geophysical technique, which allows to electrically characterize the subsurface to the depths of the upper mantle (Garcia et al., 2019). The method is based on the phenomenon of electromagnetic induction, where the temporal fluctuations in the Earth's external magnetic field with the electrycally conductive rocks of the planet generates internal secondary electrical and magnetic fields (Figure 2.1a). In the MT measurements, the magnetic and electric field variations are measured in the orthogonal directions, x and y. Commonly x, y represent the North-South and East-West orientation, respectively. In some magnetotelluric soundings, the geomagnetic variations in the vertical direction, z, are also acquired.

The theoretical part of this method was developed by the Japanese Rikitake (1948), who proposed a relation between electric and magnetic fields at long period. However, it was the Russian Tikhonov (1950) who formally defined the relationship of electromagnetic fields by means of the Impedance tensor, Z. Years later, it was the Frenchman Cagniard (1953), who first used the term "magnetotelluric" and the first application of the method to the study of sedimentary basins. Currently, it is a great geophysical exploration tool widely applied for the knowledge of aquifers, geothermal sources, tectonic studies, mining exploration and study of active faults.

Natural electromagnetic (EM) signals are generated by different sources ranging from the core of the earth to distant galaxies and they are originated in different processess (Vozoff, 1991). The frequency range in which the MT method is comprised is between $10^{-4} - 10^{4}$ Hz. There are two important source regions for this frequency range: i) for frequencies above 1 Hz, the electromagnetic waves are produced by atmospheric storms, where the signal travels as a guided wave between the ionosphere and the Earth's surface, and ii) for frequencies below 1 Hz, the signal is generated by ionospheric currents, resulting from the interaction between the solar

wind and the magnetosphere. Penetration of the geomagnetic field int the Earth's crust is determined by the ground conductivity and frequency of the geomagnetic field variations. That is to say, the rate of attenuation of the induced electric field is dependent on the vertical distribution of the resistivity of the ground, and the period considered (Ngwira and Pulkkinen (2019), Figure 2.1b).

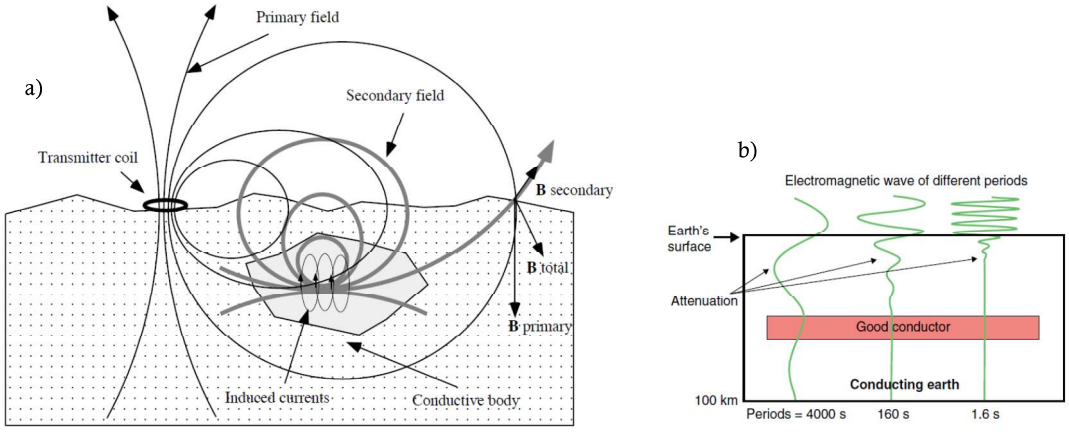


Figure 2.1: a) A schematic diagram illustrating the principle of Electromagnetic induction: A magnetic field that varies in time or space induces electric currents in conductors. These currents generate secondary magnetic fields, that are in a different direction, in different magnitude and different phase than the primary phase. From Steven Constable (IAGA-Summer School 2023). b) Depiction of electromagnetic signal penetration at different periods. Long-period signals penetrate deeper into the underground than short periods. Source: Ngwira and Pulkkinen (2019).

One of the key concepts in geomagnetic induction is that of the skin depth, the characteristic length over which electromagnetic fields attenuate. The skin depth is the distance that field amplitudes are reduced to $1/e$, or about 37%. In practical units of meters, the skin depth is

$$SkinDepth = 500\sqrt{1/\sigma f} \quad (m) \tag{2.1}$$

Where f is the frequency and σ is the conductivity of the medium.

2.1 Governing Equations

To understand the generation and propagation of electric and magnetic fields it is necessary to describe the equations that govern the behavior of electromagnetic waves in a magnetisable and polarizable medium without its own electric or magnetic source, the Maxwell's equations. In the time domain, these equations are formulated as follows:

$$\nabla \times \vec{E} = -\frac{\partial \vec{B}}{\partial t} \tag{2.2}$$

$$\nabla \times \vec{H} = \vec{J} + \frac{\partial \vec{D}}{\partial t} \tag{2.3}$$

$$\nabla \cdot \vec{B} = 0 \tag{2.4}$$

$$\nabla \cdot \vec{D} = \rho \tag{2.5}$$

Where $\vec{E}$ is the electric field in $[V/m]$, $\vec{B}$ is the magnetic flux density in $[Vs/m^2]$, is the magnetic field in $[A/m]$, $\vec{D}$ is the electric displacement field in $[As/m^2]$, $\vec{J}$ is the current density in $[A/m^2]$ and ρ is the electric charge density in $[As/m^3]$.

Equation 2.2 correspond to Faraday's law, which indicates the induction of closed loop time-varying magnetic fields along the path of an electric field. The Ampere's law in equation 2.3 indicates the vector sum of electric currents (j) and time-varying electric fields generates a circulating magnetic field. Equations 2.4 representing Gauss's law for magnetism and states that magnetic monopoles do no exist. Gauss's law for electricity is expressed in eq. 2.5 and shows that the electric field is the result of the distribution of electric charges.

To solve Maxwell's equations, empirical relations known as constitutive equations are added, which explicitly indicate the linear relationship between the fields and the medium in which they propagate. These equations are valid for an isotropic medium. These relations are:

$$\vec{J} = \sigma \vec{E} \tag{2.6}$$

$$\vec{B} = \mu \vec{H} \tag{2.7}$$

$$\vec{D} = \varepsilon \vec{E} \tag{2.8}$$

Where σ is the electrical conductivity in [S/m]; μ is the magnetic permeability in [Vs/Am]; ε is the electrical permittivity in [As/Vm].

Considering the curl of equations 2.2 and 2.3

$$\nabla \times \nabla \times \vec{E} + \nabla \times \frac{\partial \vec{B}}{\partial t} = 0 \tag{2.9}$$

$$\nabla \times \nabla \times \vec{H} - \nabla \times \frac{\partial \vec{D}}{\partial t} = \nabla \times \vec{J} \tag{2.10}$$

and, making call to the constitutive relations, we obtain:

$$\nabla \times \nabla \times \vec{E} + \mu \nabla \times \frac{\partial \vec{H}}{\partial t} = 0 \tag{2.11}$$

$$\nabla \times \nabla \times \vec{H} - \varepsilon \nabla \times \frac{\partial \vec{E}}{\partial t} = \sigma \nabla \times \vec{E} \tag{2.12}$$

The first and secondary derivatives of the vector functions $\vec{E}$ and $\vec{H}$ are continuous over the entire domain. Therefore, by changing the order of the derivation operators, the equations are rewritten:

$$\nabla \times \nabla \times \vec{E} + \mu \frac{\partial}{\partial t} \nabla \times \vec{H} = 0 \tag{2.13}$$

$$\nabla \times \nabla \times \vec{H} - \varepsilon \frac{\partial}{\partial t} \nabla \times \vec{E} = \sigma \nabla \times \vec{E} \tag{2.14}$$

Substituting the $\nabla \times \vec{H}$ and $\nabla \times \vec{E}$ with their equivalences from Maxwell's equations, we obtain:

$$\nabla \times \nabla \times \vec{E} + \mu\varepsilon \frac{\partial^2 \vec{E}}{\partial^2 t} + \mu\sigma \frac{\partial \vec{E}}{\partial t} = 0 \tag{2.15}$$

$$\nabla \times \nabla \times \vec{H} + \mu\varepsilon \frac{\partial^2 \vec{H}}{\partial^2 t} + \mu\sigma \frac{\partial \vec{H}}{\partial t} = 0 \tag{2.16}$$

Considering that $\nabla \cdot j = 0$ for a weakly conducting homogeneous medium, we have that $\nabla\sigma = 0$, therefore, $\nabla \cdot \vec{E} = 0$. Considering also a quasi-stationary regime where μ is equal to μ_0, then $\nabla \cdot \vec{H} = 0$. Consequently, equations 2.15 and 2.16 can be rewritten as:

$$\Delta \vec{E} - \mu\varepsilon \frac{\partial^2 \vec{E}}{\partial^2 t} - \mu\sigma \frac{\partial \vec{E}}{\partial t} = 0 \tag{2.17}$$

$$\Delta \vec{H} - \mu\varepsilon \frac{\partial^2 \vec{H}}{\partial^2 t} - \mu\sigma \frac{\partial \vec{H}}{\partial t} = 0 \tag{2.18}$$

Assuming harmonic time dependence ( ) electric and magnetic field with the angular frequency $\omega = 2\pi f$, we express equations 2.17 and 2.18 in the frequency domain as:

$$\Delta \vec{E} + (\omega^2 \mu\varepsilon - i\omega\mu\sigma)\vec{E} = 0 \tag{2.19}$$

$$\Delta \vec{H} + (\omega^2 \mu\varepsilon - i\omega\mu\sigma)\vec{H} = 0 \tag{2.20}$$

if we consider $k = \sqrt{\omega^2 \mu\varepsilon - i\omega\mu\sigma}$, which represent the wave number, the equations 2.19 and 2.20 can be expressed as follow:

$$\Delta\vec{E} - k^2\vec{E} = 0 \tag{2.21}$$

$$\Delta\vec{H} - k^2\vec{H} = 0 \tag{2.22}$$

Where k is a complex number. Considering the assumption that the time-varying displacement currents are negligible compared to the current density, one has that $\omega\mu\sigma >> \omega^2\mu\varepsilon$, which describes the quasi-stationary regime. In this case $k^2 \approx \omega\mu\sigma$ is a pure and consequently complex imaginary, so:

$$\Delta\vec{E} - \mu\sigma\frac{\partial\vec{E}}{\partial t} = 0 \tag{2.23}$$

$$\Delta\vec{H} - \mu\sigma\frac{\partial\vec{H}}{\partial t} = 0 \tag{2.24}$$

These equations are known as the diffusion equation.

Considering the assumption that the source of the MT wave is approximate to that of a plane electromagnetic wave, the wave can be considered to vary in the z direction, being positive downwards. Therefore, the diffusion equations for both the electric and magnetic field can be described as:

$$\frac{\partial^2\vec{E}}{\partial z^2} - \mu\sigma\frac{\partial\vec{E}}{\partial t} = 0 \tag{2.25}$$

$$\frac{\partial^2\vec{H}}{\partial z^2} - \mu\sigma\frac{\partial\vec{H}}{\partial t} = 0 \tag{2.26}$$

The solutions of equations 2.25 and 2.26 are:

$$\vec{E} = \vec{E_0}\exp i(\omega t - kz) \tag{2.27}$$

$$\vec{H} = \vec{H_0}\exp i(\omega t - kz) \tag{2.28}$$

Where $\vec{E_0}$ and $\vec{H_0}$ are the amplitudes at the Earth's surface. These two equations highlight the following statements: i) the electromagnetic signal varies sinusoidally over time, ii) the electromagnetic signal oscillates as a function of depth, iii) the field amplitude decreases with depth (attenuation) and iv) the impedance tensor calculated from the orthogonality of the electric and magnetic fields are independent of the time at which the fields were recorded, with the assumption that the conductivity of the earth does not change with time at a given station.

2.2 The Impedance Tensor

The MT data processing consists of taking the recorded values of the electric and magnetic fields for the estimation the magnetotelluric transfer function, called of the Impedance Tensor, Z. In the frequency domain, at a given frequency there is a linear relationship between the horizontal variations of the electric field (E_x, E_y) and the magnetic field (H_x, H_y) through Z. This tensor is a complex number composed of a real and an imaginary part, $Z = X + iY$.

The 2x2 impedance tensor, Z, relates the horizontal electric and magnetic fields:

$$\begin{bmatrix} E_x(\omega) \\ E_y(\omega) \end{bmatrix} = \begin{bmatrix} Z_{xx} & Z_{xy} \\ Z_{yx} & Z_{yy} \end{bmatrix} \begin{bmatrix} H_x(\omega) \\ H_y(\omega) \end{bmatrix} \tag{2.29}$$

Usually, the complex impedance tensor can be interpreted through its magnitude (apparent resistivity) and phase parameters component wise (ij = xx, xy, yx, yy):

$$\rho_a(\omega) = \frac{1}{\mu_0 \omega} |Z_{ij}(\omega)|^2 \tag{2.30}$$

$$\phi_{ij}(\omega) = \tan^{-1} \frac{Im(Z_{ij})(\omega)}{Re(Z_{ij})(\omega)} \tag{2.31}$$

The apparent resistivity denoted by ρ_a (Ωm) represents the average resistivity in a volume of subsurface at a particular frequency, and the impedance phase ϕ in degree describes the phase difference between the electric and magnetic field giving additional information on the resistivity structure (Simpson and Bahr, 2005).

2.3 Magnetotelluric models of Earth induction

The tensor character of the impedance makes it possible to determine the dimensionality of the geoelectric structure of the subsurface, i.e. whether the structure is mainly one-, two-, or three-dimensional, an indispensable question for a good interpretation of the data.

In 1D earth, resistivity varies only vertically in z direction with depth. In this case, the impedance tensor shown in Equation 2.29 has zero diagonal components ($Z_{xx} = Z_{yy} = 0$), whereas the off-diagonal entries coupling the orthogonal electric and magnetic fields have equal magnitude with a sign change ($Z_{xy} = Z_{yx}$), meaning

a phase lag of 180 degrees between the xy and yx components.

In a 2D earth, resistivity is constant in one horizontal direction known as the geo-electric strike, for example, aligned parallel to the x-axis. Resistivity varies in the other horizontal direction (y) and vertically along z. At a vertical interface between two zones of differing resistivity, electric fields (E_y) become discontinuous to guarantee conservation of current across the boundary, while the other EM field components remain continuous. The impedance tensor of a 2D earth in strike coordinate (x aligned with strike) has zero off-diagonal entries.

For 3D earth, the impedance tensor has full entries that are independent of one another ($Z_{xx} \neq -Z_{yy}, Z_{xy} \neq Z_{yx}$), and resistivity can vary along the x, y and z directions.

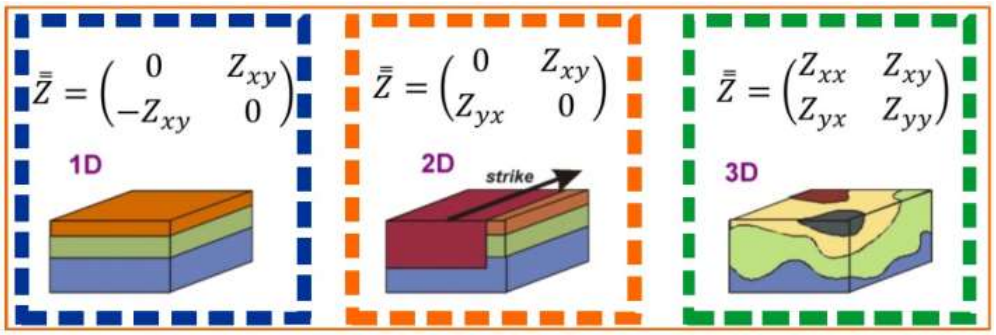


Figure 2.2: Dimensionality diagrams a their tensor representation. From Campanyá (2013)

2.4 Transfer function estimation

The theoretical development described in this section has been extensively based on the books by Zhdanov (2018) and Chave and Jones (2012). A summary explanation of the estimation of transfer functions and the mathematical methods for their derivation are presented.

Magnetotelluric data processing involves the determination of the transfer function, Z and tipper, T. In practice, the linear correlation between the components of the magnetotelluric field expressed by the functional relationships of the form of Eq. (2.29) is only approximate, not exact. In linear systems describing the conductivity of the earth, there is some noise at the time of acquisition:

The equations for calculating the impedance tensor with an additional noise term are:

$$E_x = Z_{xx}H_x + Z_{xy}H_y + r_x, \tag{2.32}$$

$$E_y = Z_{yx}H_x + Z_{yy}H_y + r_y, \tag{2.33}$$

where r_x, r_y, are the corresponding error functions (recorded noise in the respectively directions).

Considering the observations of several events, the equation 2.32 changes and it's rewritten as:

$$E_x = HZ_x + r_x \tag{2.34}$$

Where

$$E_x = \begin{bmatrix} E_{x_1} \\ E_{x_2} \\ . \\ . \\ . \\ E_{x_n} \end{bmatrix}, H = \begin{bmatrix} H_{x1} & H_{y1} \\ H_{x2} & H_{y2} \\ . & . \\ . & . \\ . & . \\ H_{x_n} & H_{y_n} \end{bmatrix}, Z_x = \begin{bmatrix} Z_{xx} \\ Z_{xy} \end{bmatrix} \tag{2.35}$$

The problem to minimize is:

$$min||HZ_x - E_x||_2^2 \tag{2.36}$$

where the subscript 2 represents the Euclidean norm.

The problem of minimising the equation 2.36 is essentially a statistical problem of establishing a linear correlation between various experimental parameters in the presence of significant noise. In the following, I will examine the most widely used data reduction methods, starting with the traditional least squares method, and progressing to the latest robust processing estimation techniques.

2.4.1 Least square method

The least squares is most commonly used method of determining the parameters defining the linear relationships between experimental data. The solution to the minimization problem is given by the least squares estimator:

$$Z_x = (H^{T*}H)^{-1}B^{T*}E_x \tag{2.37}$$

where T represents the matrix transpose and the asterisk (*) the conjugate complex. After resolving and rearranging the terms, the transfer functions Z_{xx} and Z_{xy} are given by

$$Z_{xx} = \frac{\langle H_y^* H_y \rangle \langle H_x^* E_x \rangle - \langle H_x^* H_y \rangle \langle H_y^* E_x \rangle}{\langle H_x^* H_x \rangle \langle H_y^* H_y \rangle - \langle H_x^* H_y \rangle \langle H_y^* H_x \rangle} \tag{2.38}$$

$$Z_{xy} = \frac{\langle H_y^* H_x \rangle \langle H_x^* E_x \rangle - \langle H_x^* H_x \rangle \langle H_y^* E_x \rangle}{\langle H_x^* H_x \rangle \langle H_y^* H_y \rangle - \langle H_x^* H_y \rangle \langle H_y^* H_x \rangle} \tag{2.39}$$

Similarly for Z_{yx} and Z_{yy}

$$Z_{yx} = \frac{\langle H_y^* H_y \rangle \langle H_x^* E_y \rangle - \langle H_x^* H_y \rangle \langle H_y^* E_y \rangle}{\langle H_x^* H_x \rangle \langle H_y^* H_y \rangle - \langle H_x^* H_y \rangle \langle H_y^* H_x \rangle} \tag{2.40}$$

$$Z_{yy} = \frac{\langle H_y^* H_x \rangle \langle H_x^* E_y \rangle - \langle H_x^* H_x \rangle \langle H_y^* E_y \rangle}{\langle H_x^* H_x \rangle \langle H_y^* H_y \rangle - \langle H_x^* H_y \rangle \langle H_y^* H_x \rangle} \tag{2.41}$$

Where $\langle\,\rangle$ is the average of the cross-spectra around a given frequency.

However, as solving this system of equations using the least-squares principle often delivers unreliable results when applied to real magnetotelluric data, it is hardly used in practice (Chave and Jones, 2012)

2.4.2 Robust Processing

The basis for the least-squares method is the minimization of errors in the linear relationship; that is, the error measured between a value predicted for one field component on the basis of the other observed components, and the observed values. However, within these methods, one can identify “bad” data on the basis that the error for a given point may lie at a distance of many standard deviations from a predicted value. Such bad points strongly affect the ultimate determination of the electrical conductivity function. In times past, this difficulty was avoided by arbitrary deletion of some data after a visual inspection of the field data. Egbert and Booker (1986) have suggested an approach to deletion of bad data on a statistical basis rather than by empirical selection. Having a well defined basis for deleting data facilitates the implementation on a computer of an editing process which will delete a small number of observed points.

A generalization of the robust processing approaches is described in the following according to Van Leeuwen (2016).

1. The least-squares estimate of the magnetotelluric transfer function is computed.

2. The residual r and the residual sum of squares are calculated for each channel: $r = X - (Z_1 Y_1 + Z_2 Y_2)$. Here, Z_1 and Z_2 are the leastsquares estimate of the magnetotelluric transfer function. At this point a scale factor to make r independent of the size of the input data, is calculated as well.

3. The weights and the chosen estimate, e.g. M-estimate (Chave and Thomson, 1989) or bounded influence estimate (Chave and Thomson, 2004), are computed.

4. Steps 1 to 3 are repeated until the change in the residual sum of squares is below 1%.

5. The data points with zero weight are eliminated from the data.

6. Again, steps 1 to 3 are repeated until the change in the residual sum of squares is below 1%, but this time with a fixed scale factor.

7. The data fit of this final estimate of the magnetotelluric transfer function to the measured magnetotelluric data is evaluated and the confidence bands are calculated.

Robust processing approaches, such as those introduced by Egbert and Booker (1986), Chave and Thomson (1989), Chave and Thomson (2004), Larsen et al. (1996), and Smaï and Wawrzyniak (2020), are some of the methodologies employed in the literature to estimate the magnetotelluric transfer function. Nevertheless, this thesis adopts the processing approach proposed by Egbert and Booker (1986), which will be described in the following section.

2.5 MT data analysis

2.5.1 Processing MT data

The processing of MT data was executed using the EFMT package (Egbert and Booker, 1986). This implementation follows a practical and robust approach based on multivariate statistical methods. This methodology leverages data from all channels to enhance signal-to-noise ratios and diagnose potential biases originating from coherent noise. Within the processing program, two sub-routines are executed: *dnff* and *tranMT*. Given that the MT data exist in the frequency domain, the transformation of the acquired time series into this domain is achieved through the discrete Fourier transform. For spectral analysis, the *dnff* routine is employed to derive Fourier coefficients from the recorded time series. In this process, the time series is partitioned into multiple windows, the size of which represents a compromise between the largest period intended for extraction and the resolution and precision of estimations. A higher sampling frequency leads to a greater number of samples within each window, which facilitates spectral analysis. Nevertheless, this value is not fixed in practical applications, allowing the user to validate various window sizes.

For this study, for each frequency band (e.g., 128, 512, and 4096 Hz), the *dnff* routine was applied to distinct windows to identify the window that yields smoother resistivity and phase curves, thereby enhancing the signal-to-noise ratio. The *tranMT* routine, immediately employed, conducts robust statistical processing to eliminate outliers from each segment. The final outcome of this analytical process is the estimation of the impedance tensor components, from which apparent resistivity and phase values are subsequently derived. Figure 2.3 shows an example of apparent resistivity and phase curves, illustrating the processing by frequency bands and the subsequent data selection of frequencies to obtain the final curves.

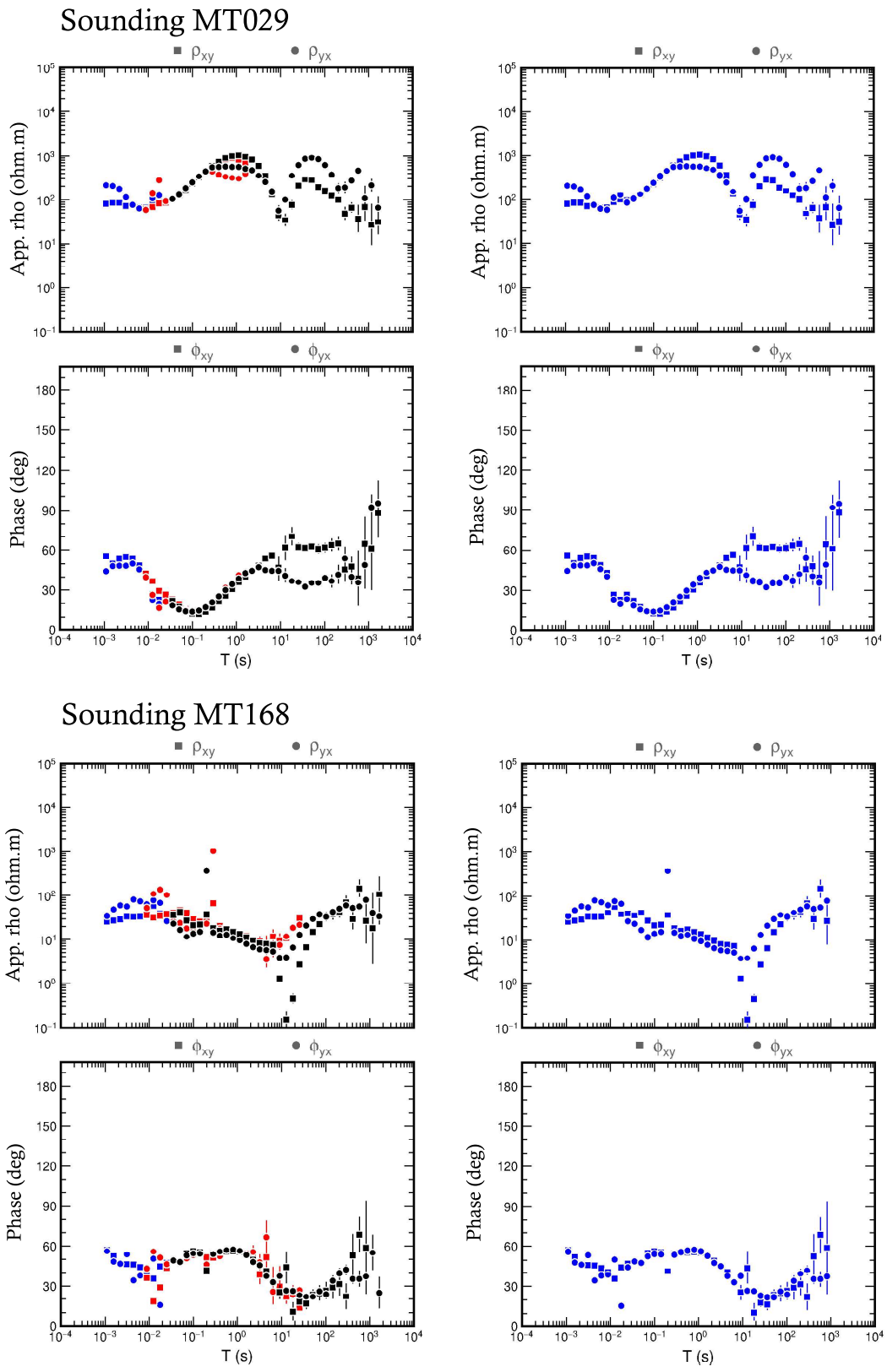


Figure 2.3: Apparent resistivity and phase curves from the sounding MT029 (upper) and MT168 (down). The left panels correspond to the processing performed for each frequency band of 4096 Hz (bleu), 512 Hz (red) and 128 Hz (black). The right panels show the frequencies that were retain a smoothed behaviour of the curves.

2.5.2 Dimensionality and directionality analysis

The impedance tensor's inherent tensorial nature facilitates the determination of the earth's internal structure dimensionality – whether it predominantly exhibits one, two, or three-dimensional behavior. This analysis, conducted prior to MT data modeling or inversion, holds paramount importance. Opting for a dimensionality lower than that dictated by the MT data and proceeding with analysis can lead to undesirable effects in inversion models, such as artifacts, which may complicate or mislead interpretations (Simpson and Bahr, 2005). This assessment can be executed through either of the following methods:

i) Tensor Decomposition: This approach, commonly employed, involves determining how effectively the measured MT impedance data can be fitted to a 2D geoelectric model. It yields estimates of the geoelectric strike direction (Unsworth, 2007).

ii) Tensorial Components Relationship: Techniques like WALDIM (Martí et al., 2013) or the Phase Tensor approach (Caldwell et al., 2004) fall within this category. The WALDIM method is a Fortran code used to conduct dimensionality analysis on a set of MT data, utilizing the WAL rotational invariants criteria. These criteria are rooted in the potential annulment of MT tensor invariants, enabling the extraction of maximal information from the tensor without presuming any a priori dimensionality. On the other hand, the Phase Tensor approach, elucidates alterations in the phase relationship between electric and magnetic fields concerning polarization in scenarios featuring a 3D conductivity structure.

2.5.3 Strike Analysis

The determination of the strike direction is a key aspect in the interpretation of MT data, as it allows the identification of the preferred orientation of subsurface conductivity structures. This direction represents the orientation along which the geoelectrical structure, and often the electromagnetic field response, exhibit the greatest degree of consistency or coherence (Chave and Weidelt, 2012).

Several approaches can be used to estimate the strike from MT data. A classical method involves the decomposition of the impedance tensor, which separates galvanic and structural effects (Groom and Bailey (1989), Bahr (1988), Mcneice and Jones (2001)). Another approach is based on the use of impedance tensor invariants, which are independent of the coordinate system and provide a more stable estimate of structural orientation (Weaver et al. (2000)). In addition, the phase tensor repre-

sentation has become a widely used tool, as it is less sensitive to galvanic distortion and provides a robust description of the geometry of conductive structures (Caldwell et al. (2004)).

In this study, the methods based on impedance tensor invariants and the phase tensor are adopted due to their robustness and their ability to provide more reliable estimates of the strike direction, as demonstrated by previous numerical studies (Delgadillo (2019)).

Figure 2.4 shows the regional distribution of the strike direction calculated from rotation invariants and the phase tensor for the entire dataset, represented using rose diagrams by decades within the period range of 0.001 to 1000 seconds. In both methodologies, the analysis results indicate a predominant strike orientation between 50° and 60° (with the inherent 90° ambiguity) in the 10^{-3} to 10^{-2} second range, although with noticeable dispersion. However, this direction becomes less well defined at longer periods, exhibiting greater dispersion and a broader range of strike angles, except for the diagram corresponding to the full range between 10^{-3} and 10^{3} seconds.

In light of the observations presented in Figure 2.4, where no clearly predominant strike direction can be identified, an independent analysis was carried out for each segment (as illustrated in Fig. 2.5). The objective of this approach is to evaluate whether any specific orientation can be identified for each of the three structural domains that make up the Parnaíba Basin.

The results show that only Profile 1 exhibits a partially discernible orientation, trending either NE or NW. However, the high degree of dispersion associated with this orientation prevents the definition of a reliable strike angle. For the other two profiles, the results display an even higher level of dispersion, with no clear clustering around a preferred direction.

Consequently, it can be concluded that the study area does not exhibit a predominant strike direction. The absence of a clear and well-defined orientation highlights the lack of a preferential structural trend, suggesting that the subsurface conductivity distribution is complex and cannot be adequately represented by a simplified 2D approximation.

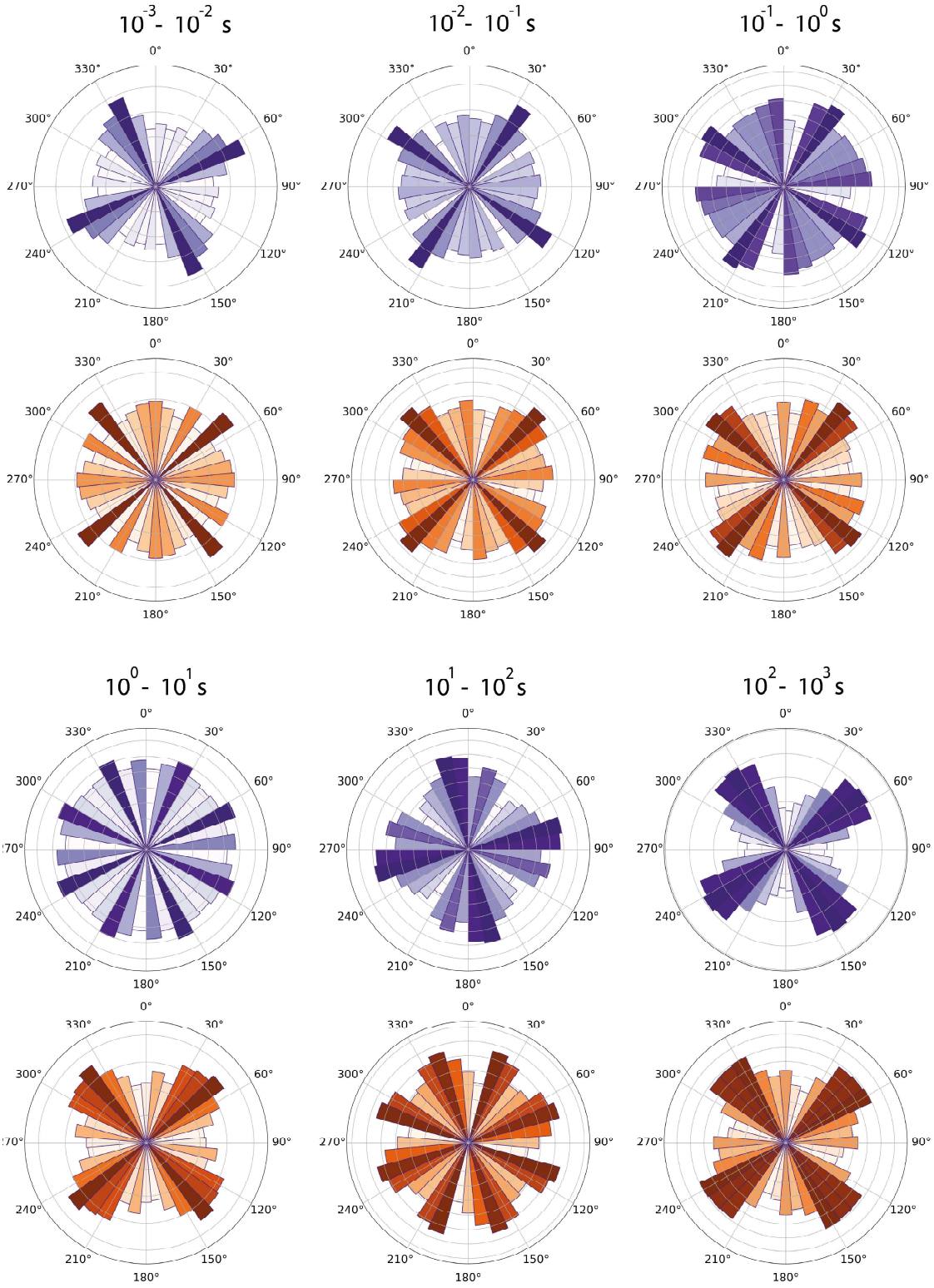


Figure 2.4: Multi-frequency and multi-station strike direction by decade for the main profile using the method described by Phase Tensor -in purple and Invariants of rotation in orange.

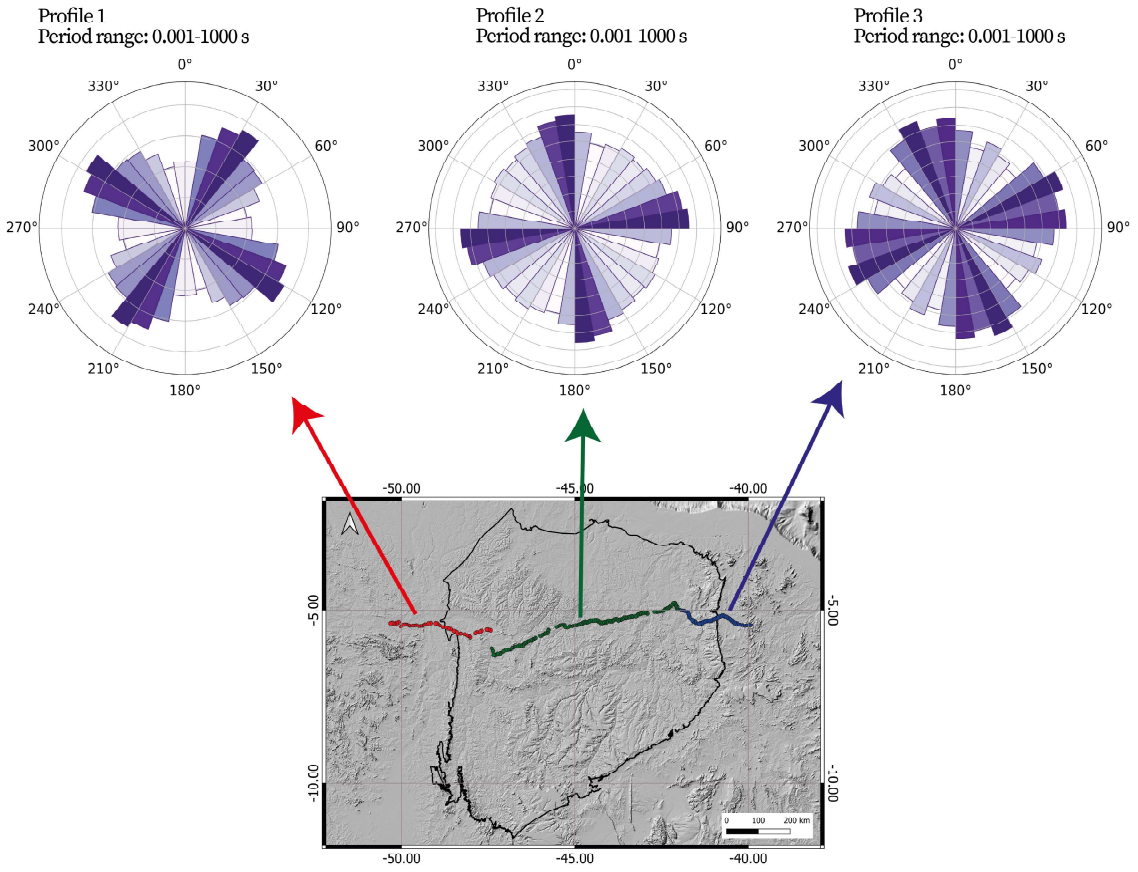


Figure 2.5: Strike direction in the period range 0.001 - 1000 s for each segment using the phase tensor (Caldwell et al., 2004)

2.6 MT data inversion

Following the processing and analysis of MT data, the dataset becomes suitable for modelling. Forward modelling and inversion techniques are then applied to construct 1D, 2D, or 3D models that describe the subsurface conductivity distribution. These models enable the integration of resistivity structures with geological information and other geophysical datasets, thereby providing insights into the present state of the subsurface and offering constraints on geodynamic processes and the Earth's evolutionary history.

Two main inversion frameworks are commonly employed: deterministic and probabilistic approaches. Deterministic inversion methods, typically based on gradient optimization techniques, seek a single model that best fits the observed data according to a predefined objective function. These approaches are computationally efficient and widely used; however, they are inherently affected by non-uniqueness and generally do not provide a direct assessment of model uncertainty. In contrast, probabilistic inversion methods adopt a statistical framework, often based on

Bayesian inference, to explore a range of models that are consistent with both the data and prior information. Rather than yielding a single solution, these approaches provide a distribution of possible models, allowing for a more comprehensive characterization of uncertainty and improving the robustness of geological interpretations.

In this thesis, Deterministic 3D and Bayesian 1D inversion approaches are employed to characterize the geoelectrical structure at different scales. In the following sections, the theoretical framework underlying each of these approaches is presented, together with their main principles, capabilities, and limitations.

2.6.1 Deterministic Inversion

The following theoretical description of MT data inversion is based on Chapter 8 written by Rodi and Mackie in the book *The Magnetotelluric Method* by Chave & Jones (2012).

The purpose of geophysical methods is to characterize the internal structure of the Earth by considering the different physical properties of rocks. Initially, this characterization is addressed through the forward problem, in which the geophysical response of a known geological model is compared with the observed field data. However, in most cases, the geological model is unknown, which is precisely the main objective of geophysics: to propose a model based on the acquired data. Therefore, an inversion process must be carried out. This process is iterative and aims to find a model whose predicted response best fits the observed data. Unfortunately, this is not rigorously achievable, as only a limited amount of data can be recorded and these data are affected by errors. Consequently, the results of an inverse problem are non-unique, since different models can fit the observed data equally well. Thus, the estimated solution must be constrained using additional information.

In the magnetotelluric inverse problem, a resistivity model is defined by a set of parameters m_j, $j = 1, ..., M$, which are real values. In the 1D case, these parameters may correspond to the resistivities of M homogeneous layers. In the 2D or 3D case, m_j may represent resistivities of M homogeneous blocks or values defined at M points arranged on a 2D or 3D grid.

The data acquired in the field can be expressed as a finite sequence of real numbers, d_i, $i = 1, ..., N$. The quantity d_i may correspond to the real and imaginary parts, or the amplitude and phase, of the impedance tensor or the tipper at each frequency.

Consequently, the inverse problem can be formulated as:

$$d_i = F_i(m_1 + m_2 + \cdots + m_M) + e_i \qquad i = 1, 2, \ldots, N \tag{2.42}$$

where F_i is the forward operator that predicts the data for a given Earth model, and e_i represents the data error. The inverse problem then consists of solving this equation for the model parameters m_j. To solve this equation, the least-squares method is commonly employed.

The best least-squares solution is the one that minimizes the discrepancy between d and $F(m)$. In geophysics, this discrepancy is commonly referred to as the *misfit*. This misfit can be expressed through a penalty function:

$$\Phi(m) = (d - F(m))^T W (d - F(m)) \tag{2.43}$$

where W is a weighting matrix containing predefined weights. This formulation is valid for determined systems; however, the magnetotelluric inverse problem is underdetermined, meaning that the number of unknown parameters exceeds the number of observations, $M \gg N$. Therefore, an additional constraint is introduced to obtain a stable and unique solution:

$$\Omega(m) \leq \mu \tag{2.44}$$

where $\mu > 0$ and $\Omega(m)$ is a stabilizing function with positive values. This function penalizes undesirable features of the model. The stabilizing function is typically a measure of model smoothness, defined as:

$$\Omega(m) = (m - m_0)^T C_m^{-1} (m - m_0) \tag{2.45}$$

where C_m is the model covariance matrix and m_0 is a reference (prior) model, penalizing deviations of m from m_0.

Consequently, the objective of inversion is to minimize the total objective function, defined as the sum of both terms:

$$\Psi(m) = \Phi(m) + \lambda \Omega(m) \tag{2.46}$$

where λ is the regularization parameter, determined by μ, which controls the relative weight between the data misfit and the stabilizing term.

The incorporation of 3D inversion methodologies is imperative due to its efficacy in representing the Earth's internal structure, given the inherently three-dimensional

nature of our planet. Starting from the 2000s, significant strides were made in the advancement of 3D algorithms, largely attributed to computational progress (e.g., Zhdanov et al. (2000), Newman and Alumbaugh (2000)). These 3D Magnetotelluric (MT) algorithms have adopted a conventional approach rooted in minimizing a functional that penalizes both data misfit and model complexity. This involves the computation of gradient components to minimize the penalizing functional, adjusting model parameters, and numerically solving the complete forward problem to assess model congruence (Siripunvaraporn et al., 2005).

Another tool for 3D inversion is the WSINV3DMT code (Siripunvaraporn and Egbert, 2009), an algorithm closely aligned with the two-dimensional data space Occam's inversion framework introduced by Siripunvaraporn and Egbert (2000). In WSINV3DMT, electric fields are computed by numerically solving the second-order Maxwell's equations through a staggered grid finite difference method. This open-access code serves the MT research community and is freely available for use. However, in the context of this thesis, I decide to use the ModEM code (Kelbert et al., 2014), a modular electromagnetic inversion system developed at Oregon State University. ModEM has gained substantial traction within academia in recent years and is accessible to academic institutions. Programmed in Fortran 77, it employs the non-linear conjugate gradient method to minimize the objective function. It incorporates numerical discretization modules based on finite difference solutions of the quasi-static Maxwell's equations in the frequency domain. The ModEM approach offers an advantageous feature wherein Jacobian computations are segregated into discrete steps encompassing data functionals, forward and adjoint solvers, and model parameter mappings. This stratagem expedites computation and renders ModEM particularly suitable for large-scale inversions (Cherevatova et al., 2015). ModEM is parallelized, capable of leveraging multiple CPUs. The optimal CPU count for each execution (Dataset) is equivalent to twice the number of periods in the data plus one. For example, with 20 periods in the dataset, 41 CPUs would be requisite.

In this thesis, the configuration of MT stations along a singular profile may be deemed non-ideal for a 3D geophysical inversion process, given the typical association of a 3D model with a grid-like distribution of soundings. Nonetheless, for the MT method, the arrangement of soundings along a profile does not impede the formulation of a 3D inversion model. Siripunvaraporn et al. (2005), employing synthetic data, demonstrated the advantages of utilizing a 3D algorithm to interpret MT data from a single profile. Their outcomes exhibited notably more plausible images of the subsurface structure beneath the profile data, even allowing for a degree of resolution for nearby off-profile features. This concept was further extended by

Patro and Egbert (2011), who conducted a 3D study utilizing real data from two profiles on the Indian subcontinent. These researchers contend that 3-D inversion facilitates a broader spectrum of solutions, contributing to a more lucid delineation of acceptable models. Moreover, 3D inversion endeavors shed light on the extent and characteristics of three-dimensional effects present in the data, constituting a valuable complement to the conventional 2D interpretation tool.

2.6.1.1 Limitation of Deterministic inversion

The limitations of deterministic inversion processes, resulting from regularisation, make it difficult to achieve a precise surface resolution, as they favour smoothed models, preventing a clear representation of the subsurface. To illustrate this issue, a simplified synthetic model was designed to represent the shallow internal structure of the Parnaíba Basin. This model, shown in Figure 2.6a, consists of a conductive layer of 50 Ωm, representing the sediments, and an underlying basement with a resistivity of 1000 Ωm. A 2D forward modelling process was carried out to generate synthetic data performed with Geotools software. These data were then subjected to a 1D deterministic inversion process employed the Occam inversion (Constable et al., 1987), which derived model is presented in Figure 2.6b. The inversion results reveal that it fails to correctly characterise the abrupt transition between the sedimentary layer and the basement, instead displaying a gradual transition, which could be misinterpreted as the presence of an additional structure. These findings highlight the need for an alternative approach, in this case, a Bayesian inversion, which allows for a more accurate characterisation of abrupt subsurface changes.

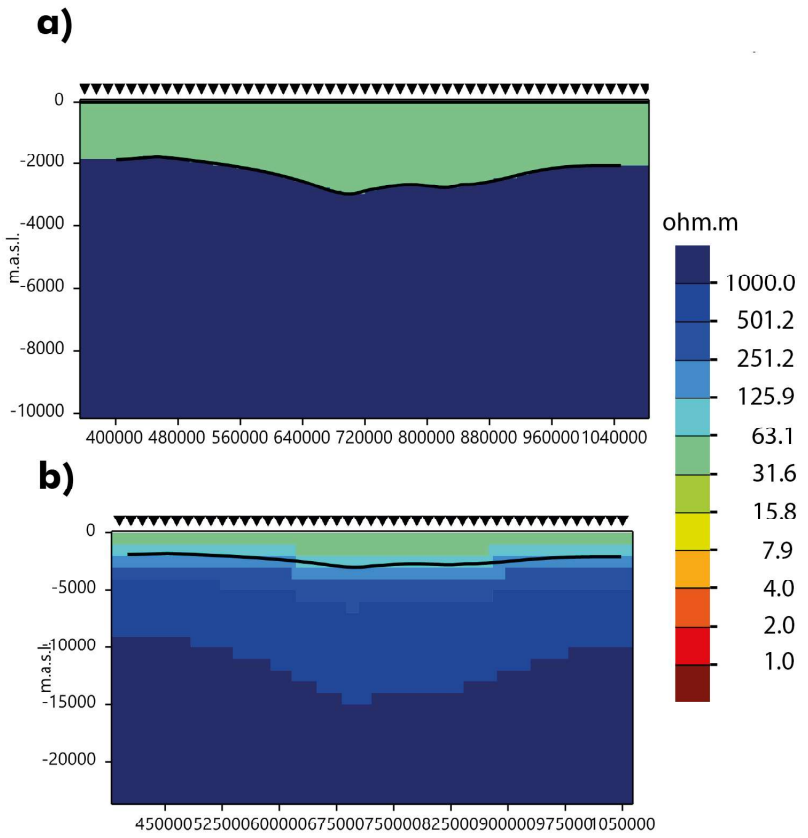


Figure 2.6: a) Synthetic model representing the shallow surface geometry of the Parnaíba Basin. b) 1D deterministic inversion model based on the synthetic data generated from the synthetic model. The solid black line represents the basement topography according to Daly et al. (2014)

.

2.6.2 Probabilistic inversion method

The following theoretical description of Bayesian inversion has been greatly inspired by the works of Manasero (2019), Manassero et al. (2020) and Rosas-Carbajal (2014).

One of the major disadvantages of deterministic inversion methodologies is that the solution often depends on the model and the initially chosen parameters, which may limit the information about the uncertainties and may also introduce a "bias", causing some features of the true model to be unresolved. Furthermore, the process of linearizing the problem and employing optimization algorithms in deterministic inversions is specifically designed for finding a single optimal or best-fitting model. Consequently, this approach makes it challenging, and in some cases impossible, to conduct comprehensive statistical assessments of model uncertainties and, perhaps even more critically, non-uniqueness. A different approach to solve inverse problems consists in considering a probabilistic framework, which do not focus on single best solutions but rather on providing a full probability distribution over the whole

model parameter space (Tarantola and Valette, 1981). This distribution, known as the posterior distribution, contains all the information about the unknown parameters given data and modelling assumptions and thus, it represents the most general solution to the inverse problem.

The probabilistic inversion, also know as the Bayesian approach, acknowledges that both the data (d) and the model parameters (m) describing the system are inherently uncertain. It treats them as random variables represented by associated probability distributions.

The application of Bayes theorem states that the posterior probability distribution function PDF of the model conditional on the data, $p(m|d)$, is given by:

$$p(m|d) = \frac{p(m)p(d|m)}{p(d)} \tag{2.47}$$

where $p(m|d)$ is the posterior conditional PDF of m given d. $p(d|m)$ is the conditional PDF of d given m, $p(m)$ is the prior PDF of the model parameters m and $p(d)$ is the prior PDF of the data. When a particular observation is made, $p(d|m)$ is considered a function of m and referred to as the likelihood.The likelihood function assesses the model's ability to explain the data, with higher likelihood associated with model predictions ($f(m)$) that closely match the observed data (d).

In many real-world applications, it's not feasible to obtain the posterior probability density function (PDF) through analytical means. Instead, extensive exploration of the potential model space is required, especially when dealing with a large number of model parameters where a basic grid search becomes impractical. To address these challenges, random exploration techniques, commonly known as Monte Carlo (MC) methods, are often employed. In higher-dimensional spaces, exhaustive random sampling is inefficient, and more sophisticated search techniques like Markov chain Monte Carlo (MCMC) simulations are necessary to accelerate the exploration of the desired distribution. The fundamental concept is to conduct a random walk, similar to Brownian motion, which, if left unaltered, would sample an initial probability distribution. However, by applying a probabilistic rule, the walk is adjusted (some proposed steps are accepted, while others are rejected) in a manner that transforms the random walk into a sampler of the target distribution (Tarantola, 2005).

2.6.2.1 1D Bayesian inversion

In the last decade, the application of probabilistic methods in magnetotelluric inversion problems has been extensively addressed, both for 1D (Conway et al. (2018), Brodie and Jiang (2018), Ardid Segura et al. (2021)) and 2D (Rosas-Carbajal et al. (2014), Chen et al. (2012)) studies. For 3D contextual studies, it remains impractical to date due to the substantial computational cost it entails (Rosas-Carbajal et al. (2015), Scalzo et al. (2019)). In 1D Earth approximation studies, the calculation can expedite the forward problem in Bayesian inversion. However, this approach can introduce bias in the results when the assumption is not met.

Recently, Seillé and Visser (2020) propose a new method to quantitatively correct the bias resulting from the 1D Earth assumption using a 1D trans-dimensional Markov chain Monte Carlo sampler. The workflow developed by the authors is shown in Figure 2.7. The main objective of their methodologyy is to derive 1-D probabilistic ensembles that account for violations of the assumption of a strictly one-dimensional Earth, which commonly arise due to the presence of complex 2-D and 3-D geoelectrical structures. While 1-D inversion offers significant computational advantages, it may lead to biased results if these dimensionality effects are not properly considered.

To address this limitation, the first stage of the workflow focuses on defining an appropriate likelihood function to be used within a trans-dimensional Markov chain Monte Carlo (MCMC) sampler. This stage, referred to as "Learning Dimensionality Compensation", aims to quantify the uncertainty associated with departures from a strictly 1-D response. This is achieved by establishing a relationship between specific attributes of the magnetotelluric data and the modelling error introduced by dimensionality effects.

The dimensionality of the subsurface is characterized using the phase tensor (β) and ellipticity (λ), which provide a robust and distortion-free description of the geometrical dimensionality of the conductivity structure as a function of frequency. These parameters allow the identification of quasi-1-D, 2-D, and 3-D behaviours in the data and therefore constitute key inputs for modelling dimensionality-related uncertainty. The discrepancy between the true 3-D response and its 1-D approximation represents a major source of uncertainty that is not adequately captured by conventional approaches based on fixed error floors. To model this effect, a machine-learning approach is employed, in which a regression tree is used to construct a Dimensionality Discrepancy Model (DDM). This model predicts a frequency-

dependent description of the modelling error conditioned on the dimensionality attributes (β and λ), effectively linking the degree of dimensionality to the expected data misfit.

Within a Bayesian framework, the likelihood function is formulated under the assumption that both the processing noise and the dimensionality discrepancy follow Gaussian distributions. The total data error is therefore described by a covariance matrix composed of two contributions: (i) a noise covariance matrix derived from MT data processing, and (ii) a model discrepancy covariance matrix predicted by the DDM. This formulation allows for frequency-dependent and correlated errors, reflecting the fact that dimensionality effects are not independent across frequencies. The DDM is trained using synthetic 3-D conductivity models designed to reproduce realistic geological scenarios, ensuring that the relationship between dimensionality parameters and modelling error is statistically representative. Once trained, the DDM can be directly applied to datasets acquired in similar geological contexts, without requiring the learning stage to be repeated.

In the second stage of the workflow, the dimensionality of the observed data is evaluated using the phase tensor invariants β and λ, and site-specific likelihood functions are derived from the trained DDM. These likelihood functions are then incorporated into a trans-dimensional MCMC inversion scheme, allowing the generation of ensembles of plausible 1-D models and enabling a quantitative assessment of uncertainty while accounting for dimensionality effects.

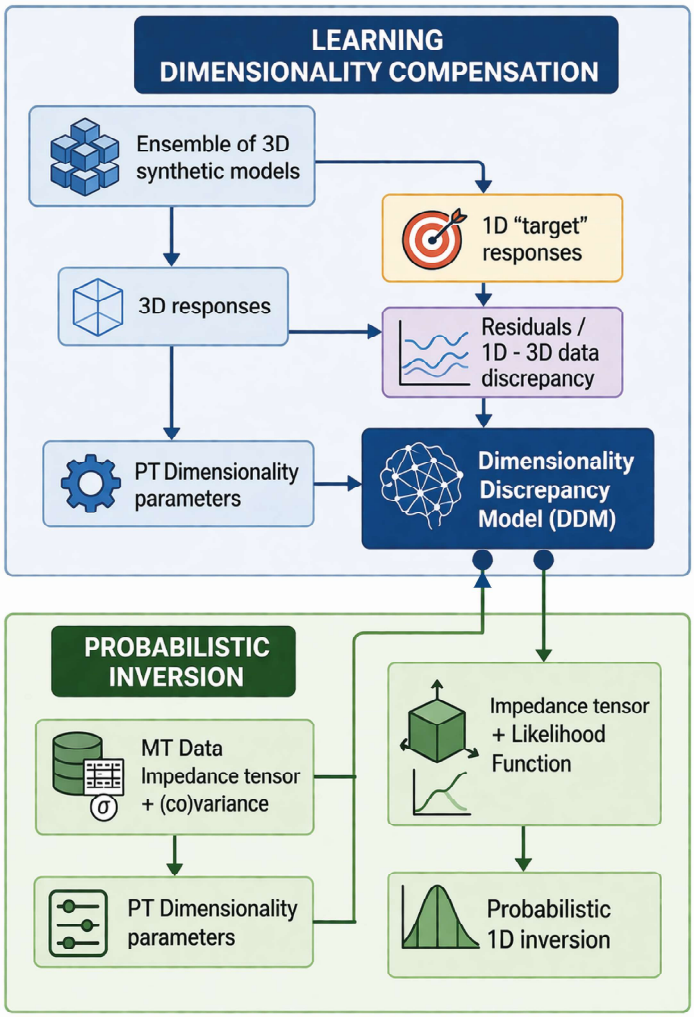


Figure 2.7: Workflow developed by Seillé and Visser (2020) to derive the likelihood function to feed into the trans-dimensional algorithm. The Dimensionality Discrepancy Model (DDM) model built in the first part of the workflow is used to estimate the error to be use in the second part of the workflow, the probabilistic inversion.

.

Based on these considerations, the likelihood used by Seillé and Visser (2020) is defined as:

$$p(d \mid m) \propto \exp\left(-\frac{1}{2}(d_{\text{obs}} - g(m))^T C_d^{-1} (d_{\text{obs}} - g(m))\right) \tag{2.48}$$

The misfit corresponds to the term inside the exponential of the likelihood function, where $g(m)$ represents the forward response associated with a model m, and C_d is the data covariance matrix. This matrix plays a central role in Bayesian inversion, as it controls how uncertainties are weighted during the inversion process.

In this study, the data covariance C_d accounts for two main sources of uncertainty. The first corresponds to measurement errors, which are estimated during

MT data processing. These errors are represented by a covariance matrix C_p, which is assumed to be diagonal since correlated noise is neglected.

The second source of uncertainty arises from the limitations of the forward modeling approach. Specifically, the use of a 1D Earth assumption to represent inherently 2D or 3D structures introduces an additional error, commonly referred to as model discrepancy. To account for this effect, we adopt the approach proposed by Seillé and Visser (2020), applied independently to each MT sounding.

This approach consists of two main steps. First, the geometrical dimensionality of the subsurface is estimated directly from the observed data using phase tensor parameters, particularly the skew angle β and the ellipticity λ. These parameters provide information about deviations from 1D behavior. To improve robustness, the phase tensor parameters are smoothed using a median filter, which reduces the influence of outliers typically associated with noisy impedance estimates.

Second, the estimated dimensionality is translated into an additional, frequency-dependent covariance term C_{dim}, which quantifies the uncertainty associated with the violation of the 1D assumption. This mapping is performed using a decision tree specifically designed for geophysical applications, such as depth-to-basement estimation. The decision tree was calibrated using synthetic 3D models that incorporate a wide range of expected 2D and 3D geological features. It links threshold values of the phase tensor parameters to corresponding levels of dimensionality-related noise (see Seillé and Visser (2020)).

The total data covariance used in the inversion is then defined as:

$$C_d = C_p + C_{\text{dim}} \tag{2.49}$$

In general, the relative contribution of these two terms varies with frequency. At high frequencies, where 3D effects are more pronounced, C_{dim} tends to dominate. In contrast, at low frequencies, the processing error C_p may become more significant, particularly when the data are noisy.

2.6.2.2 Bayesian Estimate Fusion

Estimating the depth to the interface between sedimentary cover and crystalline basement is a key objective in geophysical and exploration studies. This task is inherently challenging due to the indirect nature of geophysical observations, the

presence of noise, and the non-uniqueness of inversion results. In such a context, integrating multiple sources of information—each characterized by different levels of uncertainty and resolution—requires a robust framework capable of explicitly accounting for these uncertainties. To address this problem, this study adopts the Bayesian Estimate Fusion (BEF) approach proposed by Visser and Markov (2019), which provides a probabilistic framework for integrating diverse estimates of basement depth. In contrast to traditional interpolation methods, such as kriging, which rely on Gaussian assumptions and simplified representations of uncertainty, the BEF approach allows for more flexible and realistic uncertainty modelling, while also incorporating prior geological knowledge.

The method is formulated within the Bayesian inference framework, where the goal is to estimate the posterior distribution of the interface by combining prior information with observed data. The interface is treated as a spatially continuous variable, whose lateral variability is described using Gaussian processes, enabling the modelling of spatial continuity in geological structures. A key feature of the BEF approach is the introduction of proxies, defined as estimates or measurements that provide indirect information about the surface of interest. These may include drillhole observations, resistivity models derived from magnetotelluric inversion, or depth estimates obtained from potential field data. Each proxy is represented through a probabilistic model (proxy model), which imposes constraints on the possible location of the interface. A schematic representation of these probabilistic input estimates, together with realizations of the interface drawn from the posterior distribution, is shown in Figure 2.8.

The definition of these proxy models is a critical component of the methodology, as it allows for the explicit incorporation of various sources of uncertainty, including measurement errors, data processing uncertainties, model inadequacies, and ambiguities in geological interpretation. To systematize this process, Visser and Markov (2019) introduce the concept of proxy aspects, which describe key statistical characteristics of the data, such as independent noise, depth-dependent uncertainty, the presence of outliers, and structural constraints. Given the complexity of the problem and the lack of analytical solutions for the posterior distribution, the method relies on Markov Chain Monte Carlo (MCMC) sampling, specifically using the Metropolis–Hastings algorithm, to generate an ensemble of interface realizations that are consistent with both the data and prior assumptions. This posterior ensemble not only provides an estimate of the most likely interface geometry but also enables a quantitative assessment of the associated uncertainty.

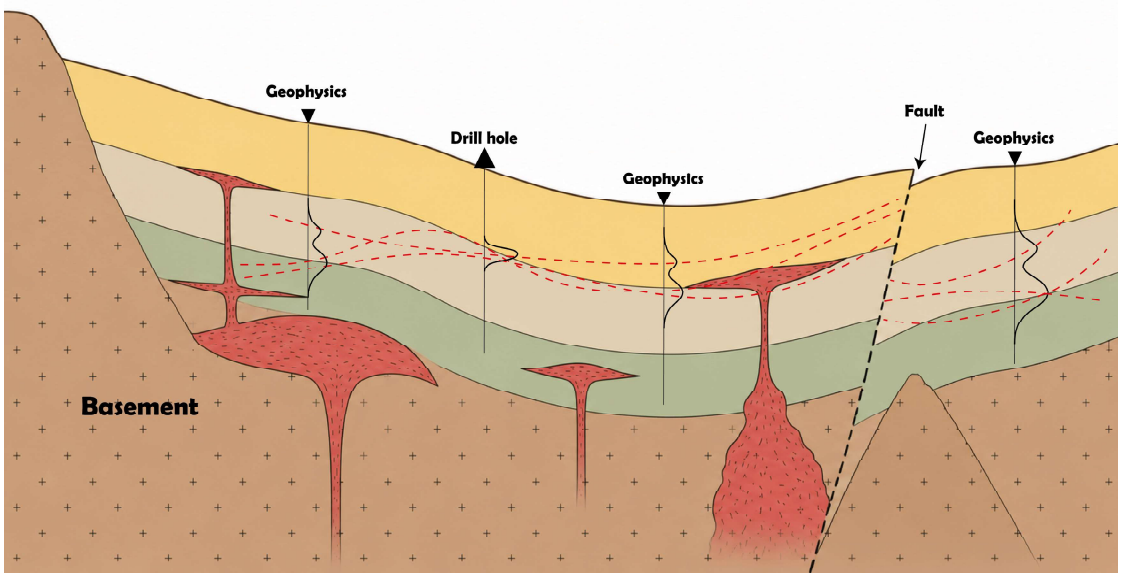


Figure 2.8: Schematic representation of the probabilistic input estimates used in this study. The red interfaces correspond to realizations drawn from the posterior distribution of interfaces, derived using the Bayesian Estimate Fusion (BEF) method. Modified from Seillé et al. (2024)

.

Chapter 3

Tectonic and Geological Setting

3.1 West Gondwana Orogen

The geological and structural comprehension of the Parnaíba Basin is founded upon the historical context of West Gondwana's genesis, a supercontinent created by the amalgamation of diverse building blocks of varying sizes, brought together through a sequence of continental collisions spanning over 150 million years (de Wit et al. (2008); Schmitt et al. (2018); Figure 3.1). A majority of these blocks originated from the fragmentation of Rodinia, encompassing a progressive convergence of Neoproterozoic landmasses that culminated during the Early Paleozoic period (Li et al., 2008). The outcome was a intricate assemblage of cratons and orogenic belts exhibiting a ductile to ductile-brittle architecture that intricately aligns with the cratons themselves (Schmitt et al., 2023). In the view of Caxito (2023), the proposed evolutionary models for this region address three fundamental inquiries, which are revisited and rigorously debated: (i) the essence of the Brasiliano/Pan-African orogenic systems, specifically whether they emerged from the subduction and collision of oceanic lithosphere, predominantly through intracontinental processes, or as a fusion of both; (ii) the ancestral origin of the continental masses involved, represented by cratons and crustal blocks of varying dimensions, and whether they were components of ancient supercontinents such as Rodinia and Columbia; (iii) the chronological order in which this amalgamation unfolded.

The West Gondwana Orogen came into existence through the convergence of two distinct sets of landmasses: the Amazonia-West African cratons and the Central African blocks (Saharan, São Francisco-Congo, Kalahari, and Rio de La Plata; see 3.1). The subsequent closure of the Goais-Pharusian Ocean is evidenced by high-pressure subduction-related rock formations along the orogen, alongside certain mafic oceanic units (Schmitt et al., 2018). This geological transformation is

defined by the establishment of the NE-SW Transbrazilian lineament, a strike-slip fault that traverses the continent on a grand scale, extending from northeastern Brazil to Argentina (Fuck et al., 2014). The distinctive NE-SW trajectory of this fault is discernible through robust magnetic anomalies within the crust (de Castro et al. (2014), Castro et al. (2016)) and reduced S-wave velocities in the mantle (Feng et al. (2007)), indicative of potential lithospheric thinning. This continental framework extends further into the African landmass along the Kandi Lineament (Figure 3.1).

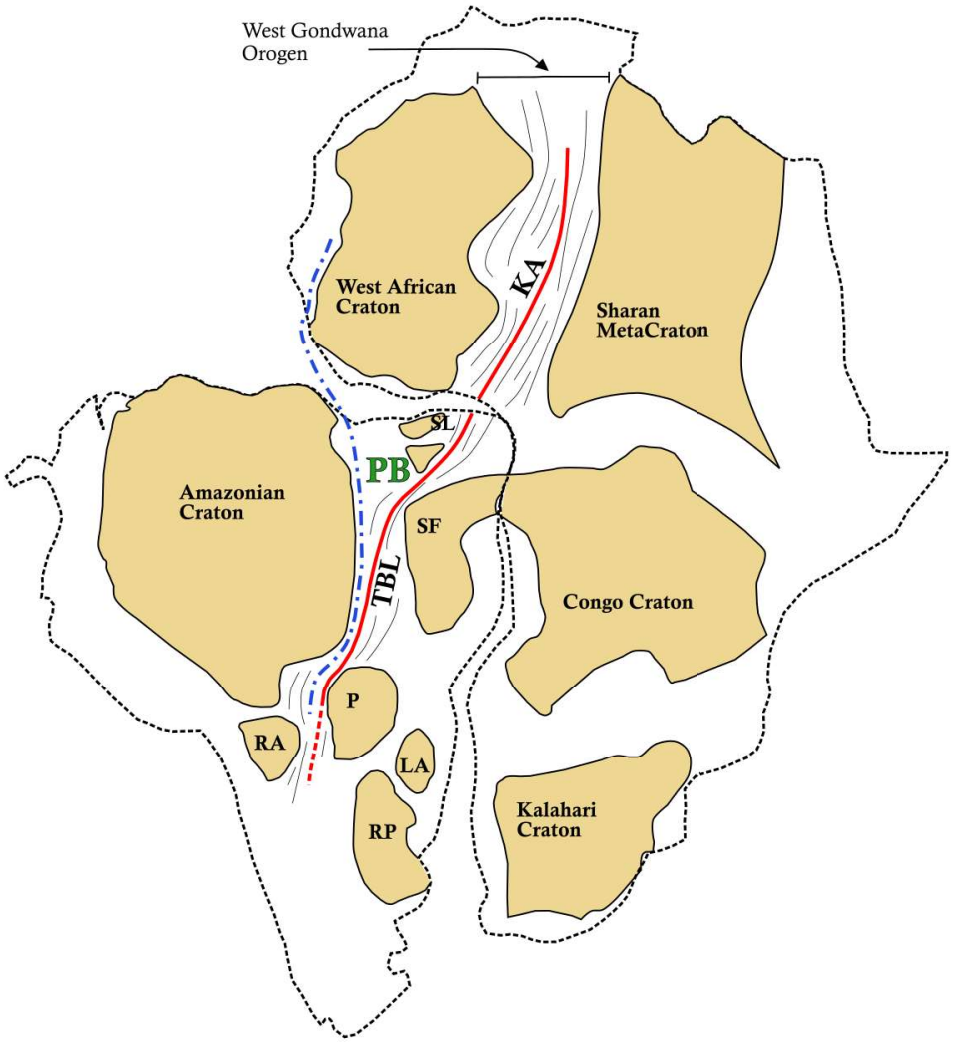


Figure 3.1: Sketch of West Gondwana reconstruction with the major tectonic elements. Abbreviations: TBL-Transbrazilian Linenament; KA-Kandi Lineanament. Cratons and cratonic fragments: PB-Parnaíba block; SL-Sao Luiz; SF-Sao Francisco; RP-Rio de la Plata; P-Paranapanema; RA-Rio Apa; LA-Luis Alves. Compilations from studies of Cordani et al. (2013) and Oriolo et al. (2017).

3.2 Geological contexts

The Parnaíba basin is one of the largest cratonic basins in the West Gondwana South American platform. This roughly circular sag basin is broadly saucer-shaped and featured relatively slow, long-lived subsidence events ($\sim$ 355 Myr in duration) from the Silurian to the late Cretaceous (Goés and Feijó, 1994). Preceding the sag sedimentation, fault reactivation of the Brasiliano shear zones controlled the formation of a set of rift basins (Jaibaras, Cococi, Sao Raimundo Nonato; Figure 3.4). The evolution of the Parnaíba basin involved tree primary tectono-sedimentary sequence delimited by unconformities, of which the first two has been largely controlled by the Transbrasilian and the Picos Santa Inés Lineaments. The first of marine influence, corresponds to the Serra Grande Group (Silurian), deposited under continental conditions, represented by a completed 1st order transgressive-regressive cycle (Assis et al., 2019). The second one is the Canindé group, where the pretoleum system of the Parnaíba basin is associated. This sequence is associated a climate events caused a global trend of rising sea level in the Devonian period, resulting in the formation of epicontinental seas and the deposition of sedimentary sequences with high transgressive trends (Torsvik et al. (2012), Torsvik and Cocks (2013)). The Canindé Group of the Parnaíba basin records one of the most important marine incursions in the South American platform (Góes et al., 1990). The third sedimentary sequence (Neocarbonifere-Eotriasic) is the Balsas Group. This sequence represents a succession of rocks deposited in a complex shallow-sea clastic/evaporitic environment, gradating to a continental environment dominated by lacustrine and desert systems (Vaz et al., 2007).

A simplified geological map of the Parnaíba basin is presented in Figure 3.2a. Due to the intricate nature of comprehending the sedimentary framework of the Parnaíba basin, Góes (1995) undertook a reevaluation of the geotectonic structures within the basin. This reevaluation accounts for their diverse genesis and tectonic evolution, as depicted in Figure 3.2b. The author designated the entire tectonic ensemble as the "Parnaíba Province," encompassing the Parnaíba, Alpercatas, Grajaú, and Espigão-Mestre basins as constituents of the "Province Parnaíba." However, it is noteworthy that this nomenclature is infrequently employed in scholarly discourse and thus shall not be utilized in this thesis.

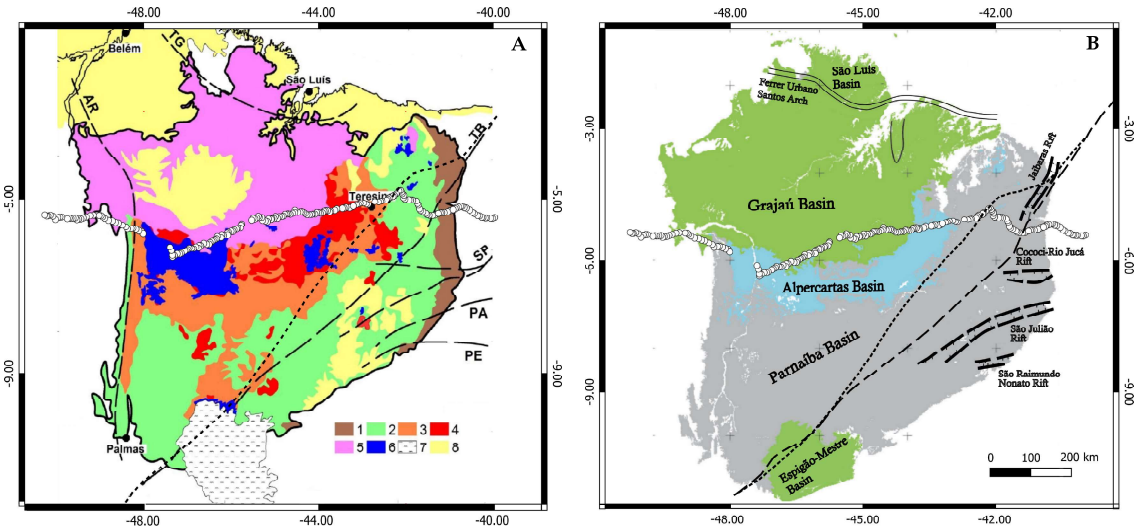


Figure 3.2: A) Simplified geological map of the Parnaíba basin (Adapted from Castro et al. (2016)). Stratigraphic units: 1 – Silurian; 2 – Devonian– Carboniferous; 3 – Permian–Triassic; 4 – Jurassic; 5 – Cretaceous; 6 – volcanic rocks; 7 – early Cretaceous São Franciscana basin; 8 – Cenozoic to recent sedimentary cover. Brasiliano shear zones: AR – Araguaia; PA – Patos; PE – Pernambuco; SP – Senador Pompeu; TB – Transbrasiliano; TG – Tentugal. B) Geotectonic units of the Parnaíba Province. Adapted from Góes et al. (1990), The white points correspond to MT soundings.

Changes in the depocentre's location throughout the basin's evolution have been extensively documented in the literature (Vaz et al. (2007), and references therein; see Figure 3.3). Initiated during the Early Paleozoic, this shift relocated the basin's depocentre to the central realm in the Early Carboniferous to Jurassic period. Subsequently, during the Cretaceous, there was a renewed northwestward migration of the depocentre. The first two sequences are shown to have been controlled by the Transbrazilian Lineament, where their maximum thickness is located in the part in the Teresina domain (Porto, 2021). While in the case of the Balsa sequence, its depocentre is located in the central part of the basin, corresponding to the Grajaú domain (Porto, 2021). These depocentres have been spatially reduced in time and show a counterclockwise structural displacement.

Regarding the magmatic processes that occurred in the Parnaíba Basin, Filho et al. (2008a) synthesizes numerous researches about the intrusive and extrusive events in the sedimentary basins sedimentary basins in Brazil. Three major magmatic episodes occurred in the basin: In the Triassic, Jurassic and in the lower Cretaceous. The first two were composed of toleitic composition (magma generated at shallow depths of 20 km) and the third one of toleitic and intermediate composition. The Triassic magmatic event, on a global scale, has been the beginning of

the continental break-up between the South American and African continents (Filho et al. (2008b)). The Jurassic event is denoted by the Mosquito formation, associated with magmatic intrusions in the central and western basin. The Cretaceous event is denoted by the Sardinha Formation, associated with the opening of the South Atlantic opening (Baksi and Archibald, 1997).

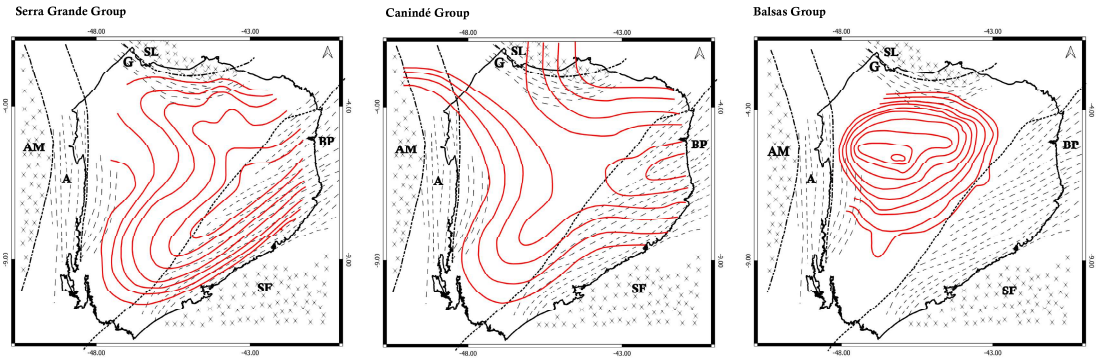


Figure 3.3: Isopachs of the three sedimentary sequences: Serra Grande, Canindé and Balsas. Geotectonic units: AM- Amazon craton; A-Araguaia belt; SL- Sao Luis craton; BP-Borborema Province; SF-Sao Francisco craton

3.3 Parnaíba basement

The presence of a subterranean block beneath the Parnaíba basin has been a subject of prolonged debate over the years. Initially, Brito Neves et al. (1984) and Cordani et al. (1984) postulated the existence of an expansive triangular block situated at the heart of the basin. This block, constituting a Precambrian crystalline basement, underlies the sedimentary sequences that were subsequently reworked during the Brazilian orogenic cycle. Cordani et al. (2009), revisiting and refining his earlier research, took into account the most recent geophysical and geological investigations into the Parnaíba Basin. In light of these developments, the authors advanced a more comprehensive conceptualization by proposing four distinct "geotectonic provinces" characterizing the basement structure. These provinces encompass Granja Norte, Granja Sul, Parnaíba or Xambioá, Monte Alegre-Conceição. Three of the largest masses identified as foundational elements of the basin (Granja Norte, Granja Sul and Monte Alegre-Conceição) are constructed from metamorphic rocks of medium to high grade. Radiometric analyses of exposed portions within the basin suggest an origin in the early Paleoproterozoic era. Drawing an analogous inference, the central block (Parnaíba Massif), located entirely beneath the subsurface and lacking direct data, is provisionally assigned to the Paleoproterozoic period. Despite the absence of contemporary tectonic records, these substantial and rigid crustal enti-

ties are postulated to have arisen through the fragmentation of the supercontinent Rodínia, an event that transpired approximately 900 million years ago, predating the formation of the Brazilian folding belts (Cordani et al., 2009). Likewise, De Castro et al. (2014) based on magnetic and gravity signatures, introduces a novel structural framework for the basement, delineating the Parnaíba massif into three distinct blocks: northern, southern, and Teresina. All these interpretations, as indicated by the various authors mentioned above, are illustrated in Figure 3.4.

Soares et al. (2018) further refines this interpretation by subdividing the central Parnaíba Block into two well-defined domains: Grajaú and Teresina. Among these, the Teresina domain is particularly significant, as it hosts the highest concentration of exploratory deposits identified in the region. Futhermore, Solon et al. (2018) reports a prominent west-dipping conductivity anomaly located between both domains at mid- to lower-crustal depths, suggesting the presence of deep-seated structures that may play a key role in controlling the geodynamic evolution of the area. The authors interpret this anomaly as a paleosuture. Schiffer et al. (2021) corroborates this interpretation by identifying a high Vp/Vs ratio (1.76) associated with one of the three Neoproterozoic suture regions underlying the Parnaíba basin. Expanding on these findings, Porto et al. (2022) conducts a more extensive analysis of the geological dataset within the Parnaíba Basin. The author interprets this conductivity anomaly as a suture zone positioned between the Grajaú and Teresina Blocks. Furthermore, Porto et al. (2022) substantiates this assertion by highlighting distinctive characteristics of the two blocks: the Grajaú block features a low gravity anomaly and a thicker crust measuring 41-45 km, while the Teresina block possesses a slightly thinner crust (39-41 km) accompanied by elevated gravity and magnetic anomaly values.

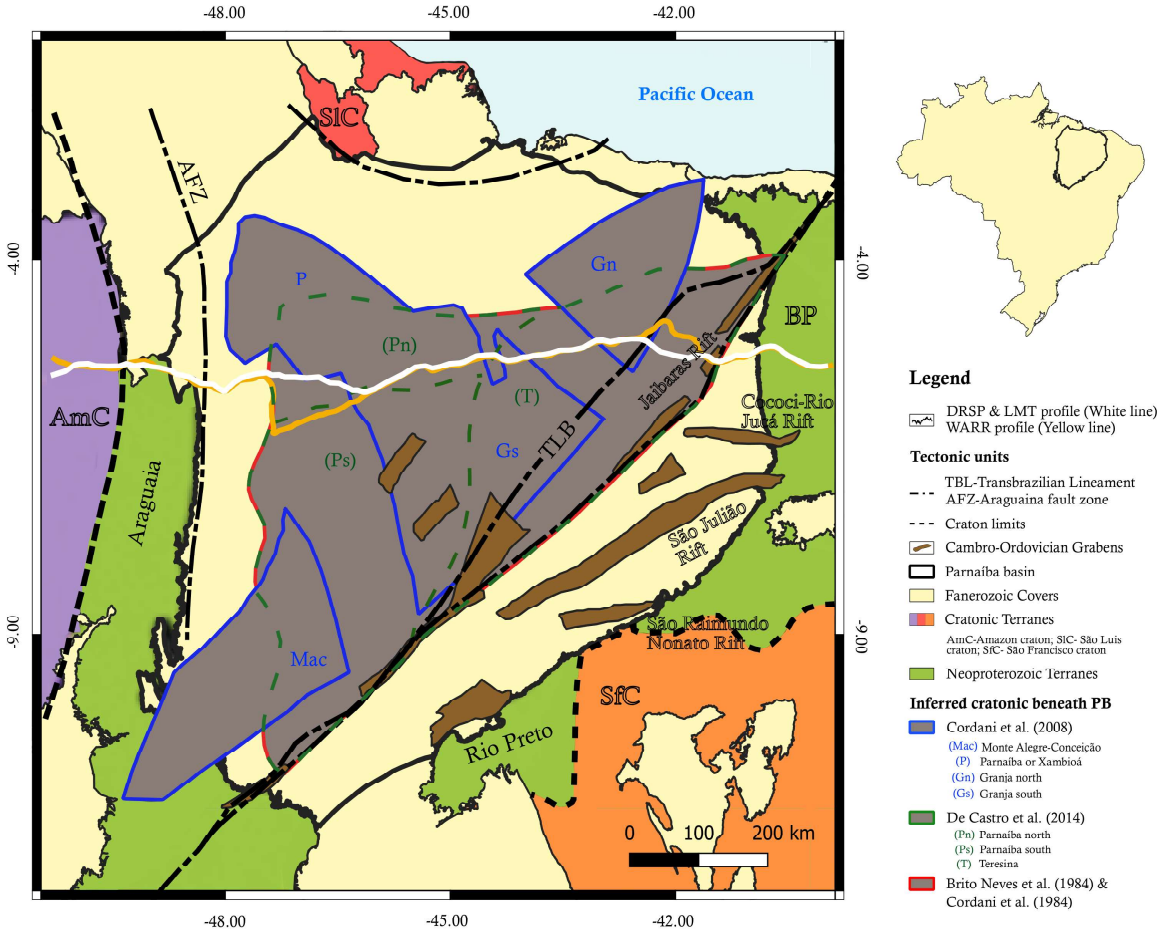


Figure 3.4: Inferred cratonic basement below the Parnaíba Basin according three interpretations (Adapted from Porto (2021)). The Crambro-Ordovician grabens are in agreement with the results of De Castro et al. (2014). The white line represents the DRSP and LMT studies of Daly et al. (2014) and Solon et al. (2018), respectively. The yellow line corresponds to the WARR study of Soares et al. (2018).

Chapter 4

Magnetotelluric imaging of the Parnaíba Basin: Implications to the West Gondwana formation

4.0.1 General Outline

This chapter presents the first publication of this thesis (called here as the "Scientific Paper 1"), entitled as: "Magnetotelluric imaging of the Parnaíba Basin: Implications to the West Gondwana formation ". This paper was published in July 2025 in the journal **Tectonophysics**.

"Scientific Paper 1" demonstrates that the application of three-dimensional magnetotelluric investigation enables a robust characterization of the internal configuration of the Parnaíba Basin, providing key insights into its tectonic evolution. The resulting resistivity models reveal the crustal and lithospheric architecture and highlight the presence of distinct tectonic domains, offering new constraints on the processes involved in the assembly and reworking of the basin.

Our study contributes to a better understanding of the role of the Parnaíba Basin within the broader geodynamic framework of Western Gondwana. By integrating deep geoelectrical information with existing geological and geophysical data, the results provide a more comprehensive view of crustal amalgamation processes and lithospheric evolution. Consequently, this work offers a valuable reference for future studies aiming to investigate similar intracratonic basins and their significance in large-scale tectonic reconstructions.

4.0.2 Scientific Paper 1

Magnetotelluric imaging of the Parnaíba Basin: Implications to the West Gondwana formation

Gonzalo Romero-Beltran [a,*], Emanuele F. La Terra [a], Liliane P. Panetto [a,b], Hoël Seillé [c]

[a] National Observatory, Department of Geophysics, Rua Jose Cristino 77, Rio de Janeiro, Brazil
[b] Department of Petrology and Geotectonics, Federal Rural University of Rio de Janeiro, Seropédica, Rio de Janeiro, Brazil
[c] CSIRO Mineral Resources, Kensington, WA, Australia

ARTICLE INFO

Keywords:
3-D inversion
Parnaíba basin
Magnetotellurics
West Gondwana
Basement
Resistivity

ABSTRACT

The Parnaíba Basin, in northeastern Brazil, is one of the most significant intracratonic basins on the South American platform. Its formation, driven by vertical thermal and mechanical processes has been extensively studied, however, the internal structural configuration remains subject of debate. Magnetotellurics (MT) is a geophysical method that provides information about the geo-electric internal distribution. As part of the multi-physics Parnaíba Basin Analysis Project (PBAP), 218 broadband and 37 long-period MT stations were deployed along an *E*-W transect profile of ~ 1400 *km*. The MT data were inverted to produce 3-D resistivity models. Lateral resistivity variations were identified along the profile and interpreted as the amalgamation of the three blocks, from west to east: Amazonian Craton, Parnaíba block, and Borborema Province. Within each block, the models reveal differentiated geoelectric behaviours. The Amazonian Craton exhibits a high-conductivity domain associated with the replacement of a delaminated lithosphere. The Parnaíba block comprises two distinct tectonic domains: the resistive Grajaú block and the conductive Teresina block. Their resistivity contrast is associated with magmatic activity, which is more intense in Teresina. However, Cretaceous extensional events related to the opening of the South Atlantic may have also influenced it. In the Borborema Province, resistive and conductive signatures at lower crustal depth are identified, providing evidence of collisional events associated with its formation in the Neoproterozoic. These deep resistivity models provide new evidence for the crustal amalgamation of the Parnaíba Basin and offer insights into the tectonic processes that shaped Western Gondwana.

1. Introduction

According to the classification of sedimentary basins—whether intraplate, divergent, convergent, or other tectonic types—there are significant differences in their composition and structure at the crustal and upper mantle depths (Ingersoll, 2011). These differences manifest in the mechanisms of basin formation and the mineral composition of their internal structures, which play a critical role in basin evolution. The formation of intracratonic basins, in particular, is still an active subject of investigation because of its complex and poorly understood mechanisms. In this paper, we propose to image and understand the internal configuration of the Phanerozoic intracratonic Parnaíba Basin in northeastern Brazil, one of the largest and most geologically significant basins on the South American platform.

The crustal and lithospheric configuration of the Parnaíba Basin has been the focus of geophysical studies conducted as part of the Parnaíba Basin Analysis Project (PBAP), a multidisciplinary initiative integrating data from deep seismic reflection (DSR), wide-angle reflection-refraction (WARR), and magnetotelluric (MT) methods. These studies were carried out along an approximately 1400 *km* long *E*-W oriented profile across the basin. More details on these studies and their corresponding models are provided in Text S1 and Figs. S1-S2 in the Supplementary Material. Recently, based on seismic data, the configuration of the basement has been associated with the collision of two distinct tectonic blocks: Grajaú and Teresina (Soares et al., 2018; Schiffer et al., 2021). This result aligns with the presence of a heterogeneous lithospheric structure beneath the basin, characterized by a high-velocity feature under its northern portion and a gradual decrease in velocity towards the south (Nascimento et al., 2024). However, these models contradict the hypothesis previously proposed by De Castro et al. (2014), who suggest that the concealed basement beneath the sediments consists of a single and stable cratonic block, characterized by dominantly

north–south-oriented low gravity anomalies. Such discrepancies highlight the need for further geophysical investigations to constrain the tectonic evolution of the basin. On the other hand, the formation of the basin, which is associated with the absence of regional extension or evidence of lithospheric stretching (Daly et al., 2018; Daly et al., 2019) is still subject to debate. Recent geophysical studies suggest that the basin originated through vertical lithospheric subsidence driven by thermal or mechanical processes (Watts et al., 2018; McKenzie and Rodríguez Tribaldos, 2018; Tozer et al., 2017). These flexural and subsidence models, however, present certain inconsistencies, as they propose the presence of extensive igneous intrusions that, upon solidification, would have exerted a load on the crust and lithosphere. This interpretation does not align with the 6.8 km/s velocity recorded in the lower crust by Soares et al. (2018), as this characteristic value for a mafic composition deviate from the expected range of 6.9–7.2 km/s, which is typically associated with igneous intrusions (Rudnick and Fountain, 1995; Christensen and Mooney, 1995). This discrepancy raises questions about the true nature of the lower crust and its role in the evolution of the basin's subsidence.

The magnetotelluric method (MT) provides unique insights into anomalies associated with fluids, faults, suture zones, and mineralogical composition, using the variations of the electrical properties of the subsurface. An initial MT study by Solon et al. (2018), using 37 long-period magnetotelluric data, provided a deep geoelectrical model of the basin's lithospheric structure. However, given the limited coverage of MT stations and considering the vast dimensions and size of the basin ($600{,}000\ km^2$), the resolution at crust and upper mantle depths remains insufficient and far from fully resolved. This paper presents the modelling of a new dataset consisting of 218 broadband magnetotelluric stations, distributed along an *E*-W transect profile of approximately 1400 km (Fig. 1). This dataset is complemented by the 37 long-period MT stations used in Solon et al. (2018). The whole dataset was collected under the Parnaíba Basin Analysis Project. The new magnetotelluric images presented here will enable a more detailed characterization of the crust and uppermost mantle beneath the basin, offering new perspectives on the lithospheric evolution of the region. Similar studies have shown that deep geoelectric signatures can preserve ancient tectonic histories, as observed in other cratonic regions such as the Dharwar Craton (Naganjaneyulu and Santosh, 2012) and the Canadian Shield (e.g., Spratt et al., 2014). Our results provide new insights into understanding alternative amalgamation models and their implications for the formation of Western Gondwana.

2. Tectonic and geological settings

The geological and structural comprehension of the Parnaíba Basin is founded upon the historical context of West Gondwana's genesis, part of a supercontinent created by the amalgamation of diverse building blocks of varying sizes, brought together through a sequence of continental collisions spanning over 150 million years (De Wit et al., 2008; Schmitt et al., 2018; Fig. 2). A majority of these blocks originated from the fragmentation of Rodinia, encompassing a progressive convergence of Neoproterozoic landmasses that culminated during the Early Paleozoic period (Li et al., 2008). The outcome was an intricate assemblage of cratons and orogenic belts exhibiting a ductile to ductile-brittle architecture that intricately aligns with the cratons themselves (Schmitt et al., 2023). The West Gondwana Orogen came into existence through the convergence of two distinct sets of landmasses: the Amazonian-West African cratons and the Central African blocks (Saharan, São Francisco-Congo, Kalahari, and Rio de La Plata; Fig. 2a); with the Goiás-Pharusian Ocean as the separation between both sets of cratonic blocks. The subsequent closure of this ocean and the establishment of the NE-SW Transbrasiliano Lineament (TBL) represent the final stage of the formation of Western Gondwana in the Neoproterozoic.

The Parnaíba basin spans three Precambrian major tectonic and terrane units (Daly et al., 2014; Tozer et al., 2017; Soares et al., 2018; Solon et al., 2018; Schiffer et al., 2021). From west to east these blocks are the Amazonian Craton, Parnaíba block and Borborema Province. They are surrounded and separated by orogenic belts formed through collision and accretion events during the Neoproterozoic, as part of the Brasiliano Orogenic collage (Brito Neves and Fuck, 2013; Brito Neves et al., 2014). The basin exhibits a roughly circular sag basin morphology, and it has experienced slow but prolonged subsidence for approximately 355 million years, beginning in the Silurian and continuing into the Late Cretaceous (Góes and Feijó, 1994). The basin's evolution is reflected in three major tectono-sedimentary sequences,

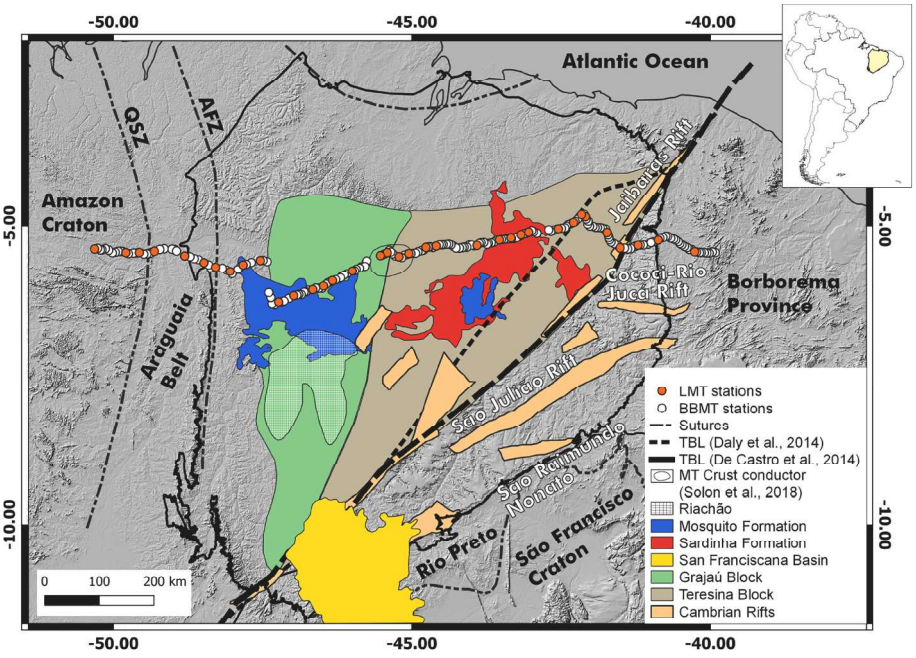


Fig. 1. MT stations distribution map over the simplified tectonic configuration of the Parnaíba Basin. The white circles correspond to BBMT data and the orange ones represent the LMT station correspond the data used in Solon et al. (2018) and which are reutilized in this study. Tectonic units: AC - Amazonian Craton, BP - Borborema Province, SFC – São Francisco Craton. Suture zones: QSZ - Quatipuru shear zone; AFZ - Araguaia fault zone.

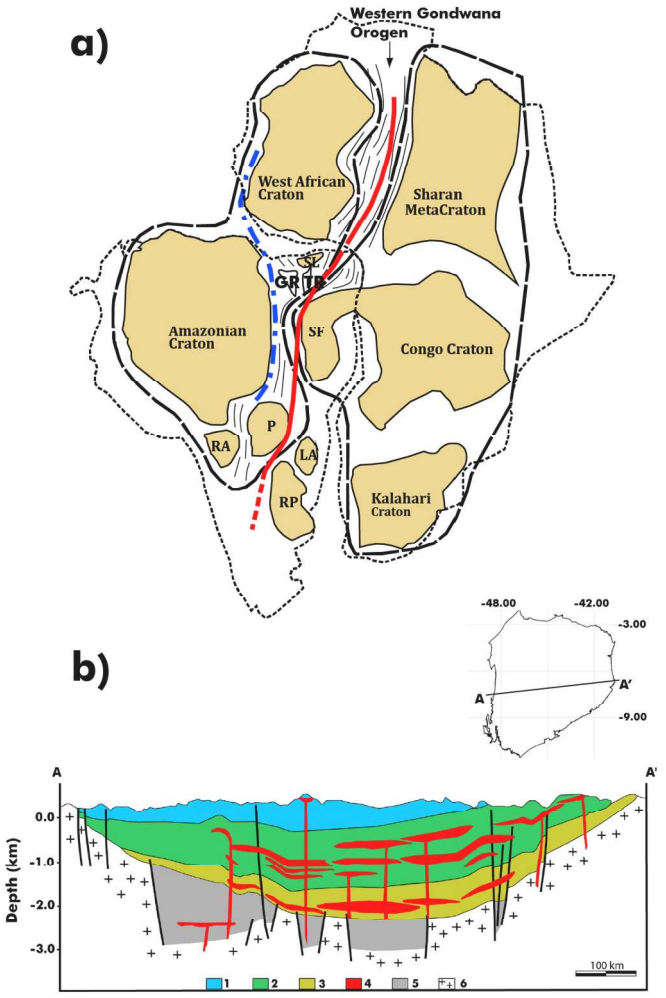


Fig. 2. a) Sketch of West Gondwana reconstruction with the major tectonic elements. Cratons and cratonic fragments: GR-Grajaú block; TR-Teresina block; SL-São Luiz; S-São Francisco Craton; RP-Rio de la Plata; P-Paranapanema; RA-Rio Apa; LA-Luis Alves. The red line corresponds to the Transbrasiliano and Kandi Lineaments. The blue dashed line represents the location of the suture of the Cambrian Clymene Ocean as proposed by Tohver et al. (2012). b) Cross geological section of the Parnaíba basin after Góes and Feijó (1994). 1-Balsas Group; 2-Canindé Group; 3-Serra Grande Group; 4-Magmatic intrusions; 5-pre-Silurian rifts; 6- Basement.

each separated by unconformities. The first sequence, influenced by marine conditions, corresponds to the Serra Grande Group (Silurian), featuring a complete first-order transgressive-regressive cycle (Assis et al., 2019). The second sequence, the Canindé Group, is notable for its association with the basin's hydrocarbon system and is linked to a global sea-level rise during the Devonian (Torsvik et al., 2012; Torsvik and Cocks, 2013). The Canindé Group records one of the most significant marine incursions in the South American platform (Góes et al., 1990). The third sequence, the Balsas Group (Late Carboniferous-Early Triassic), represents a succession of rocks deposited in a complex shallow-sea clastic/evaporitic environment, gradually transitioning to a continental environment dominated by lacustrine and desert systems (Vaz et al., 2007). Beyond these sedimentary sequences, the basin witnessed two major magmatic events related to the opening of the Atlantic Ocean at the Triassic–Jurassic boundary and in the early Cretaceous. The early Jurassic (ca. 200 Ma) lava flows of the Mosquito Formation occurs essentially in the western and southern basin. In contrast, sill complexes and dike swarms of the Early Cretaceous (129–124 Ma), Sardinha Formation occur in the eastern part of the basin and are chrono-correlated to the large Paraná–Etendeka igneous province and to the Rio Ceará–Mirim Dike Swarm (De Castro et al., 2018). Fig. 2b shows a representative geological cross-section of the Parnaíba Basin.

The Transbrasiliano Lineament (TBL) is a strike-slip fault that traverses the continent framework on a grand scale, extending from northeastern Brazil to Argentina (Fuck et al., 2014) and extends further into the African landmass along the Kandi Lineament. Its tectonic significance has traditionally been interpreted as a shear zone, although it has also been described as a Neoproterozoic cryptic suture (Arthaud et al., 2008). The distinctive NE-SW trajectory of this fault is discernible through robust magnetic anomalies within the crust (De Castro et al., 2014; De Castro et al., 2016) and reduced S-wave velocities in the mantle (Feng et al., 2007; Nascimento et al., 2024), indicative of potential lithospheric thinning. Daly et al. (2014), based on deep seismic reflection (DSR) data, propose that the TBL marks the boundary between the Parnaíba block and the Borborema Province, where the position of the lineament is located approximately 100 km west of its traditionally recognized position based on potential field data (De Castro et al., 2014; Fig. 1). The magnetotelluric model presented by Solon et al. (2018), both traces of the lineament are identified through resistive signatures extending from the surface to lithospheric depths, suggesting that the TBL corresponds to a deformation zone. During the early Paleozoic, the reactivation of the TBL triggered the formation of pre-existing strike-slip faults, leading to the development of the Ediacaran-Cambrian continental rift system, composed of several small NE-SW aligned rift basins, including Jaibaras, Cococi-Rio Jucá, São Julião, and São Raimundo Nonato (Brito Neves et al., 1984; Oliveira and Mohriak, 2003; Fig. 1). Furthermore, seismic data have revealed remnants of Cambrian basins formed in a foreland setting, such as the Riachão Basin (Porto et al., 2018; area delimited in the southwestern part in Fig. 1). The Araguaia belt is bounded to the west by the Quatipuru suture zone and to the east by the Araguaia shear zone (Fig. 1). This belt corresponds to the orogenic system that forms the Araguaia and Paraguay belts as part of the Tocantins Province, a Neoproterozoic orogen developed during the collision between the Amazonian, São Francisco/Congo, and West African palaeocontinents. The existence of the suture zone resulting from the closure of the Cambrian Clymene Ocean, driven by the collisional event along the Araguaia and Paraguay belts, has been a subject of debate (Cordani et al., 2013). However, the presence of ophiolites located 200 *km* south of the profile provides evidence of remnants of oceanic lithosphere, as reported by Paixão and Nilson (2002) and Kotschoubey et al. (2005).

2.1. *Magnetotelluric exploration in the Parnaíba Basin*

The magnetotelluric method (MT) is a passive electromagnetic geophysical technique that enables the characterization of the geoelectric properties of the Earth, from the near surface to the depths of the upper mantle (Garcia et al., 2019; Simpson and Bahr, 2005). MT data are highly sensitive to variations in electrical conductivity both laterally and vertically (Jones, 1992), providing images of electrical resistivity. This parameter is particularly sensitive to (a) temperature and (b) the presence of highly conductive phases, such as water, melt, sulphides, or graphite (Unsworth, 2010). In sedimentary basin contexts, magnetotelluric studies have proven to be essential for characterizing internal structures and contributing to the understanding of their tectonic evolution (e.g., Hautot et al., 2000; Bologna et al., 2013; Padilha et al., 2015).

In the Parnaíba Basin, as part of the PBAP initiative, Solon et al. (2018) performed a magnetotelluric study using data collected from 37 long-period MT stations. The study identified three distinctive basements underlie the Parnaíba Basin: The Amazonian Craton, the Parnaíba block and the Borborema Province. These units were delineated by identifying subvertical resistive signatures associated with the Quatipuru suture zone, the Araguaia shear zone, and the Transbrasiliano Lineament. The authors reported that the Parnaíba block is characterized as a conductive domain, where conductivity anomalies had

previously been identified by Arora et al. (1999). Both groups of authors interpret this region as lithospheric impregnation by conductive minerals associated with tectonic processes, potentially linked to Brasiliano orogenic events or magmatic residues from persistent igneous intrusions during the Triassic-Jurassic and Cretaceous periods. Furthermore, Solon et al. (2018) identified an elongated crustal conductor in the central region of the Parnaíba block, which deepens eastward and is interpreted as a paleo-suture (see slight black ellipsoid in the center of the profile in Fig. 1). The deep resistivity model does not identify the presence of the concealed basement beneath the Parnaíba Basin, and the crustal resolution within the three blocks remains far from being fully resolved.

Other MT studies in the Parnaíba Basin have primarily focused on its southeastern margin (Rocha et al., 2019; Romero et al., 2019) and the northern part of the basin (Uchoa et al., 2020). Investigations along the southeastern margin identified crustal conductive anomalies associated with suture zones, providing evidence of the amalgamation of the eastern margin basement of the Parnaíba Basin with the Borborema Province and the São Francisco Craton. These studies also revealed the presence of Cambro-Ordovician rift-grabens, primarily located along the Transbrasiliano Lineament (Fig. 1). In turn, Uchoa et al. (2020) correlated the resistivity structure of the São Luís craton with the West African Craton for metallogenetic purposes. Similarly, magnetotelluric investigations in the northwestern portion of the Borborema Province, including the eastern margin of the Parnaíba Basin, have identified high-resistivity zones at the crustal and upper-mantle depth, interpreted as remnants of Neoproterozoic subduction zones. Additionally, crustal

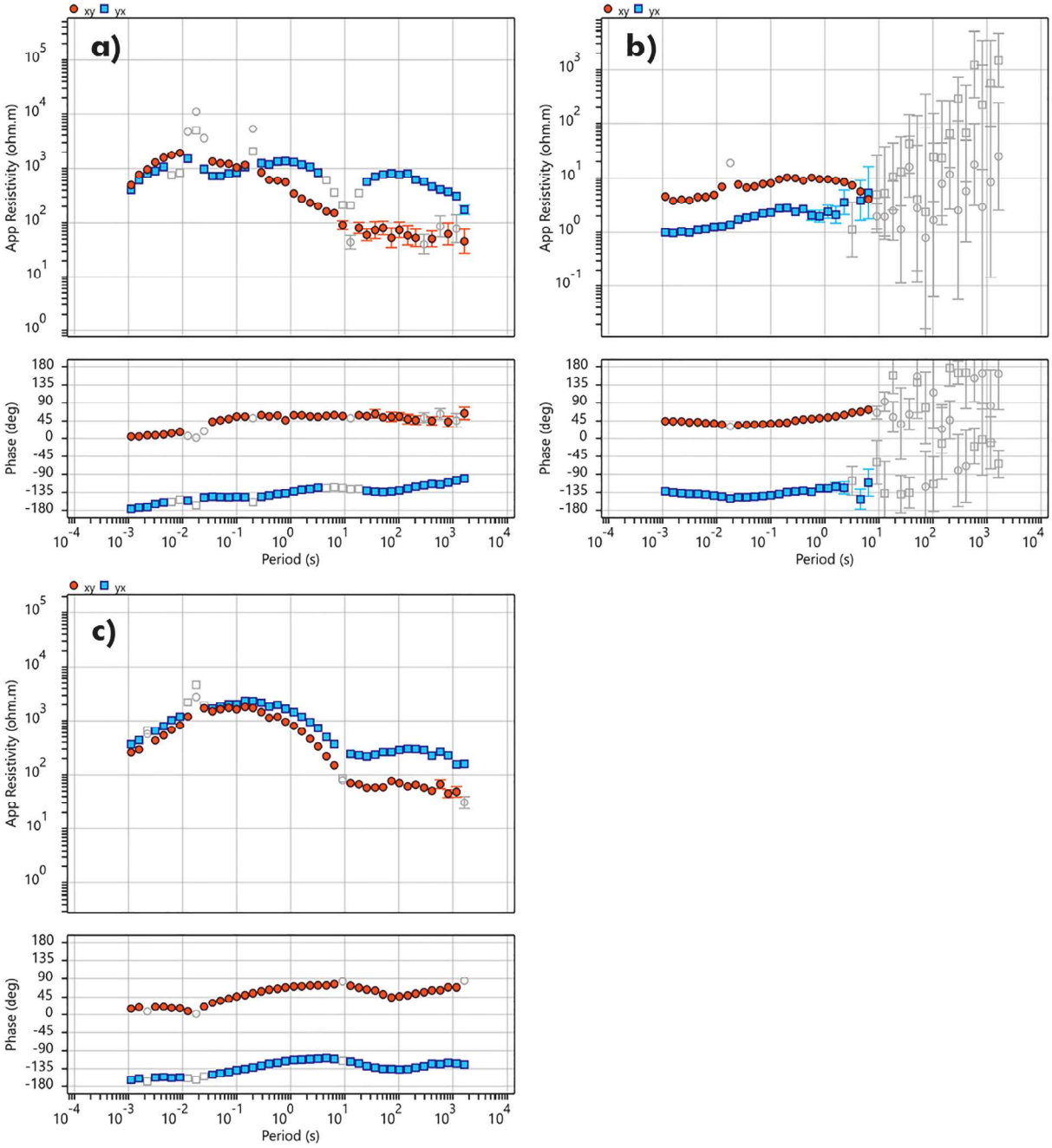


Fig. 3. Apparent resistivity and phase curves of three representative stations: a)-station MT011 located in the extreme east of the profile, in the Borborema Province; b) - station MT122, located in the central part of the basin (Parnaíba block) and c) - station MT263, located in the western part of profile, within the Araguaia Belt. The deactivated data, represented in gray, correspond to frequencies removed for being noisy data and data falling within the dead-band.

conductivity anomalies have been linked to collisional and accretionary processes during the Neoproterozoic, providing valuable insights into the tectonic evolution and formation of the Borborema Province (Padilha et al., 2014; Padilha et al., 2017). The MT profiles from these studies are shown in Fig. S1 of the Supplementary Material. As stated above, this paper presents a MT profile that explores and studies, at the crustal and upper mantle depths, the entire east-west extent of the Parnaíba Basin.

3. MT data modelling

3.1. Magnetotelluric data

MT data were collected as part of the PBAP project between 2013 and 2014, using Metronix ADU-07 and LEMI instruments for broadband and long-period data, respectively. The magnetotelluric dataset comprises 218 new broadband stations and the 37 long-period stations used by Solon et al. (2018). The distribution of the stations is shown in Fig. 1. Broadband stations were spaced approximately 5 *km* apart, and the profile extended over 1400 *km* in an *E*-W direction, spanning from the Amazonian Craton to the Borborema Province. The MT data were processed using the robust method of Egbert (1997). This processing employed a practical and robust approach based on multivariate statistical methods, leveraging data from all channels to enhance the signal-to-noise ratio and diagnose potential biases from coherent noise. The data processing involves obtaining the impedance tensor, graphically represented by apparent resistivity and phase curves derived from the tensor. The response curves underwent an editing stage to analyze and retain only the frequencies with a physically meaningful magnetotelluric interpretation. Specifically, frequencies exhibiting a smooth variation, characteristic of the electromagnetic diffusion phenomenon, were selected. Additionally, low-quality data within the "dead band" (1–10 s) were removed. Fig. 3 illustrates this procedure as applied to three representative MT stations for the XY and YX polarizations, in geographic coordinates with the x-direction defined as north and the y-direction as east. Most of the data collected in the central region of the basin (Parnaíba block) exhibited poor quality, with significant noise in the frequency range from 1 to 10 s, primarily because of the low-resistivity material at the surface that resulted in weak electric fields. In contrast, stations located at the ends of the profile (Amazonian Craton and Borborema Province) generally provided good-quality and lower-noise data. Where long-period data were available they were merged with the broadband data (37 stations in total, Fig. 1).

3.2. Dimensionality and directionality analysis

The impedance tensor's inherent tensorial nature facilitates the determination of the Earth's internal structure dimensionality – whether it dominantly exhibits one, two, or three-dimensional behaviour. This analysis, conducted prior to MT data modelling or inversion, is essential to prevent undesirable effects in inversion models, such as artifacts, which can complicate or mislead interpretations (Simpson and Bahr, 2005).

In this paper, we employed Phase Tensor analysis, because it is not affected by galvanic distortion and does not make any assumptions about the underlying conductivity structure (Caldwell et al., 2004). Mathematically, the phase tensor can be defined as $\Phi = X^{-1}Y$, where X is the real and Y the imaginary part of the impedance tensor; and graphically the phase tensor is represented as an ellipse, with Φ_{max} and Φ_{min} representing the maximum and minimum axis of the ellipse, respectively. Additionally, Caldwell et al. (2004) introduced the parameter skew (β), which indicates the dimensionality of the structure. For 1-D regional conductivity structures, the phase tensor is represented almost as a circle and $\beta = 0$. If the regional conductivity structure is 2-D, the phase tensor is symmetric ($\beta = 0$) with one of its principal axes aligned parallel to the strike axis of the regional structure. In the 3-D case, the phase tensor is nonsymmetric ($\beta \neq 0$) and results in ellipses. The phase tensor analysis is displayed in pseudo-sections in Fig. 4a. Caldwell et al. (2004) recommended a value of $|\beta| > \pm 3^{\circ}$ to justify a 3-D interpretation.

In the Amazonian Craton, high skew magnitudes ($> 3^{\circ}$) are observed at both low and high periods, indicating a locally 3-D resistivity structure at shallow and deep depths. In the central region of the profile, corresponding to the Parnaíba Block, the dimensionality analysis for periods <0.1 s shows $|\beta|$ values below 3° and circular phase tensor shapes, which indicate a dominantly 1-D structure. For periods >1 s, a frequency gap is observed, attributed to the data exclusion process discussed in the previous section. In the Borborema Province, between 0.001 and 1 s, a more complex pattern is observed, with elliptical phase tensor shapes indicating 2-D and 3-D resistivity structures without a clear preferred strike direction. For periods >1 s, a more consistent pattern is identified, characterized by high skew values ($> -3^{\circ}$). These results suggest that the Parnaíba Basin dominantly exhibits a one-dimensional resistivity structure at high frequencies, transitioning to a three-dimensional behaviour at longer periods (greater depths) along the entire profile.

The skew angle analysis establishes an understanding of the dimensionality along the profile, but the phase tensor itself can be plotted as an ellipse, with the major and minor axis depicting the invariant maximum and minimum phase, Φ_{max} and Φ_{min}, respectively (Caldwell et al., 2004). The direction of the major axis of the ellipse indicates the direction of major horizontal current flow. The ellipses analysis with Φ_{max} is presented in Fig. 4b. For periods <1 s, stations located in the Parnaíba block show ellipses with low ellipticity and maximum phases between 40°–70°, indicating relatively homogeneous structures. Ellipses in the domain of the Amazonian Craton and the Borborema Province exhibit high ellipticity and maximum phases below 30°, illustrating a strong increase in resistivity with depth. As we move towards the central part of the basin from the eastern and western edges of the profile, ellipticity is high and maximum phases range between 40° and 80°. These results reveal the structural complexity of the basin, which is consistent with the dimensionality analysis performed using the skew. Furthermore, changes in the values of Φ_{min} indicate vertical gradients in the conductivity structure. The analysis of the phase tensor using Φ_{min} is presented in Fig. 4c. Values with $\Phi_{min} > 45^{\circ}$ represent decreasing resistivity with depth, while $\Phi_{min} < 45^{\circ}$ indicates increasing resistivity with depth (Caldwell et al., 2004). Towards the central part of the basin, Φ_{min} presents values >45°, which, based on its shape, correlate with the sedimentary sequences. In contrast, beneath these sequences, Φ_{min} shows values <45°, likely associated with the crystalline basement of the basin. At even longer periods, Φ_{min} increase again, revealing conductive anomalies related to the tectonic history of the basin's formation. In general, Φ_{min} provides a clear representation of the geometric shape of the basin.

On the other hand, a geo-electrical strike analysis was implemented using the phase tensor methodology within a frequency range of 0.001 s – 1000 s. The results, illustrated in Fig. 4d as a rose diagram generated with the MTpy code package (Kirkby et al., 2019), reveal a significant degree of dispersion, indicating the absence of a preferred strike direction. Therefore, based on the results of ellipticity, the dimensionality analysis, and the strike analysis, it can be concluded that the region underlying the Parnaíba Basin is dominantly complex and heterogeneous, indicating that the most appropriate process is a 3-Dinversion.

3.3. 3-D inversion

The MT data were inverted using the ModEM code (Kelbert et al., 2014), a modular electromagnetic inversion system. It employs the nonlinear conjugate gradient method to minimize the objective function (see eq. 1). It incorporates numerical discretization modules based on finite difference solutions of the quasi-static Maxwell's equations in the frequency domain. ModEM particularly is suitable for large-scale

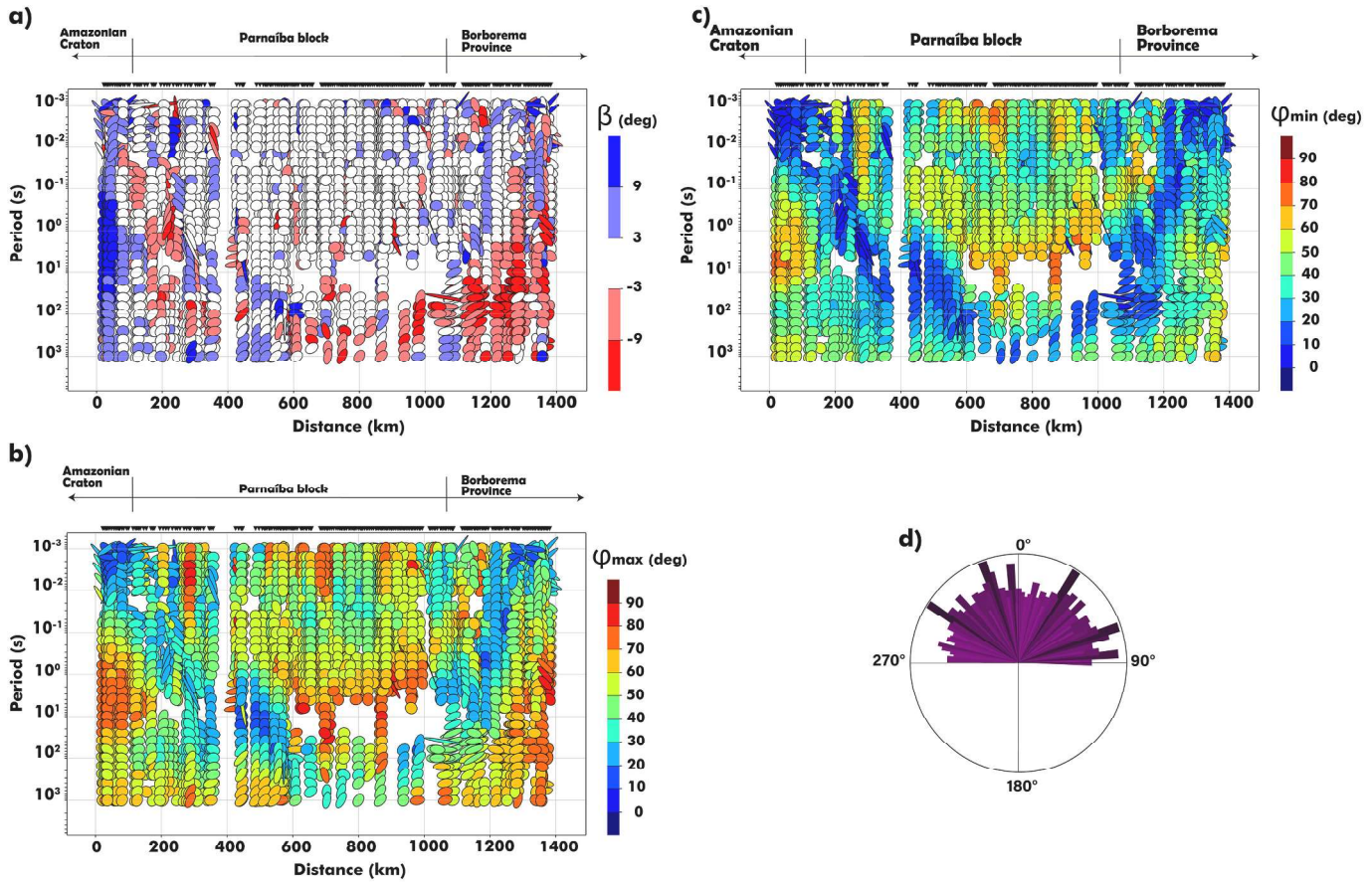


Fig. 4. a) Dimensionality analysis section applying the phase tensor methodology along the MT profile. The ellipses are coloured according to the normalised skew value. b) Phase tensor analysis with ϕ_{max}, where values close to 0° indicate significant variations in the horizontal direction, meaning the medium is electrically isotropic or uniformly stratified. Intermediate values suggest the presence of an elongated structure or a directional variation in electrical conductivity, such as faults, fractures, or geological boundaries, guiding the current flow in a preferential direction. Values close to 90° represent three-dimensional heterogeneity. c) Phase tensor analysis coloured with ϕ_{min}, where warm colors indicate conductive structures, and cool colors indicate resistive structures. d) Strike analysis according to the phase tensor methodology for the entire MT dataset within a frequency range of 0.001 to 1000 s.

inversion routines (Cherevatova et al., 2015). The configuration of MT stations along a singular profile may be deemed non-ideal for a 3-D geophysical inversion process, given the typical association of a 3-D model with a grid-like distribution of soundings. Nonetheless, in the MT method, the arrangement of soundings along a profile does not impede the formulation of a 3-D inversion model. Siripunvaraporn et al. (2005), employing synthetic data, demonstrated the advantages of utilizing a 3-D algorithm to interpret MT data from a single profile. Their outcomes exhibited notably more plausible images of the subsurface structure beneath the profile data, even allowing for a degree of resolution for nearby off-profile features. This concept was further extended by Patro and Egbert (2011), who conducted a 3-D study utilizing real data from profiles on the Indian subcontinent. Based on this, 3-D inversion routines along profiles are widely applied to MT studies in tectonic contexts (e.g. Brasse et al., 2015; Seillé et al., 2022). The inversion problem can be formulated by the equation:

$$\delta(m) = (d - F(m))^T W (d - F(m)) + \lambda (m - m_0)^T K (m - m_0) \quad (1)$$

where d is the data space - a vector containing the observed data, F is forward function predicting the theoretical values of the data of a hypothetical representation of the Earth, m represents the space model which contains the real resistivity values of Earth, W is the weight matrix containing pre-assigned weigh, or the data covariance matrix (Egbert and Kelbert, 2012), λ is the regularization parameter, m_0 is a prior or initial model and K is positive-definite matrix referred to as model covariance matrix. The structure of penalty K can be interpreted as an inverse a prior model covariance matrix.

3.4. Inversion strategy

In this work, one of the main challenges encountered in the implementation of the 3-D inversion process was the large number of MT stations and the extensive area to be considered, which results in a large mesh size and consequently a significant increase in computational cost. Therefore, the entire profile was divided into three sub-profiles: i) Profile 1, consisting of 45 stations numbered from MT274 to MT205, spans largely the eastern edge of the Amazonian Craton and the Araguaia Belt, ii) Profile 2, comprising 123 stations numbered from MT192 to MT054, primarily covers the Parnaíba block; and finally, iii) Profile 3, which includes 61 stations numbered from MT064 to MT001, extends from the Transbrasiliano Lineament to the western edge of the Borborema Province. Note that there is an overlap of 11 stations between Profiles 2 and 3 in order to improve lateral correlation between the resulting models. The distribution of stations, considering the subdivision into the three profiles, is shown in Fig. 5a.

3.5. Inversion parameters

One of the primary challenges inherent in the deterministic inversion process is the potential existence of a substantial multitude of models capable of conforming to the observed data, commonly referred as the non-uniqueness of the inverse problem. Consequently, identifying the

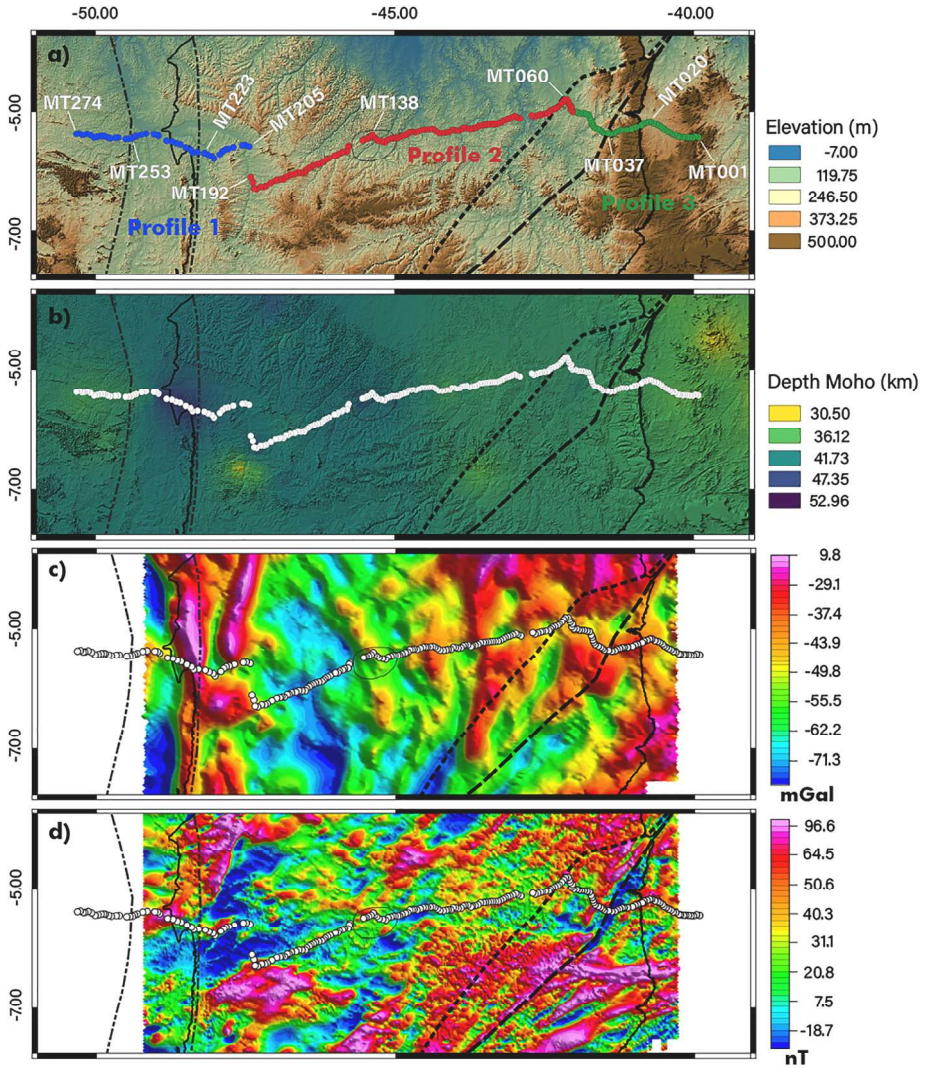


Fig. 5. a) Distribution of MT stations over the topographic map, illustrating the division of the profile into three sub-profiles, with the names of some representative stations also displayed for interpretative and reference purposes. The region outlined by the black line in the central part of Profile 2 represents, in this figure and the following three, the location of the conductive anomaly identified by Solon et al. (2018). b) Moho depth map derived from compiled seismic data (see Text S2 and Fig. S3 of Supplementary Material for more information). Note that the depth of the Moho in the eastern section of the Parnaíba Basin is shallower compared to the western section. c) Bouguer anomaly map, and d) Total magnetic field map, derived from aerogravimetric and aeromagnetic data acquired by the Agência Nacional do Petróleo.

optimal parameters to discern the most fitting model consistently poses a daunting task. For this reason, we conducted a series of 3-D inversion tests to identify the appropriate initial model and the covariance value. We performed inversion tests on Profile 1, whose results have been extrapolated to profiles 2 and 3. The selected parameters are detailed below, along with the justification for their choice based on the inversion tests performed.

We tested three homogeneous half-space initial models of 50, 100, and 200 Ωm, as shown in Fig. S4 of the Supplementary Material. The corresponding nRMS values were 1.49, 1.54, and 1.94, respectively. In general, the resistivity models capture similar features at both shallow and deep depths. However, the choice of initial resistivity has a significant impact on the results, following the trend that a more resistive starting model tends to produce a more resistive final model. We selected an initial resistivity of 100 Ωm, as it provides an acceptable nRMS value and represents a balanced approximation of resistivity and conductivity structures in the Earth's subsurface. This value is commonly used in magnetotelluric studies with high station density across large regional areas, as it is considered representative of resistivity in tectonic contexts. Similar approaches have been adopted in large-scale studies such as USArray and AusLAMP MT (e.g., Thiel et al., 2020; Meqbel et al., 2014; Bedrosian and Feucht, 2014; Patro and Egbert, 2008). The initial model for each profile included seawater, locked at resistivity of 0.3 Ωm, taken from https://maps.ngdc.noaa.gov/ . More details on the ocean's influence on the MT data, refer to Text S3 and Figs. S6 and S7 of the Supplementary Material.

The model covariance matrix K penalizes deviations from a prior model (Egbert and Kelbert, 2012) and it provides a priori constraints on the magnitude and spatial smoothness of conductivity variations (Meqbel, 2009). This matrix partly depends on the parameters α (not shown in eq. 1), which control model smoothness in each coordinate direction. The smoothing parameter can be defined between a range from 0 to 1, where higher values derive smoother models. We conducted two inversion tests using covariance values of 0.2 and 0.3. The resulting models are shown in Fig. S5 of the Supplementary Material. The model with a covariance value of 0.2 achieved an nRMS of 1.62, while the model with 0.3 attained 1.54. We selected the value of 0.3 for two main reasons: i) it yields the lowest nRMS, and ii) it is recommended for achieving an optimal balance between model roughness and smoothness (Kelbert et al., 2014; Samrock et al., 2015).

ModEM employs a structured 3-D cubic mesh oriented in the geographic Cartesian system (*X, Y* in the horizontal direction, and *Z*, positive downwards) for the numerical discretization of electric and magnetic fields. For each profile model, the mesh was densified in the area of interest and became less dense as we moved away from this area. The model for each profile encompassed a sufficiently large surrounding space to adequately address the boundary conditions associated with electromagnetic wave propagation. In the *X* and *Y* directions, we try to maintain discretization in the area of interest with three to four cells between adjacent stations, in order to find a compromise between a fine grid and reasonable computation time. In the *Z* -direction, the initial layer was set to 25 m thick, which satisfy the skin-depth condition using the highest frequency modelled. The vertical grid spacing increased geometrically with a factor of 1.2. The corresponding model for the Profile 1 grid consists of 86 × 296 × 51 cells in the two horizontal and the vertical directions, respectively. For the Profile 3, we set 104 × 251 × 51 cells as mesh. In the case of Profile 2, where the stations are distributed approximately in a NE-SW direction, the mesh generation still resulted in a relatively dense grid in both the *X* and *Y* directions. To reduce the computational cost of the inversion process for this profile, the mesh was rotated by 13° eastward. In order to compensate for this mesh rotation, the impedance tensor was also rotated in the opposite direction by −13°, meaning towards the west. This significantly reduced the computational cost of the inversion process. For profile 2, we set 84 × 354 × 51 cells as the grid size.

The inversion process was conducted exclusively considering the four components of the impedance tensor $(Z_{xx}, Z_{xy}, Z_{yx}, Z_{yy})$, in the period range from 0.001 to 1000 s with a reduced set of 31 frequencies. We set an error floor of 5 % on anti-diagonal (Z_{xy}, Z_{yx}) and 10 % on the main diagonal (Z_{xx}, Z_{yy}), values that fall within the range commonly applied in 3-D inversion processes (Miensopust, 2017). Data errors were established from $\sqrt{abs(Z_{xy}{}^{*}Z_{yx})}$ for each component.

3.6. Inversion results

The inversion process for Profile 1 began with an initial nRMS of 11.95, which improved significantly to 1.54 after 113 iterations. For Profile 2, the initial nRMS was 20.29, decreasing to a final value of 2.1 after 237 iterations. Similarly, Profile 3 started with an nRMS of 8.27, which was reduced to 1.32 after 149 iterations. The data fit for each profile and for all four components of the impedance tensor are presented in Fig. 6. In general, the fit distribution is highly satisfactory for most stations within Profiles 1 and 3. In Profile 2, some components did not achieve an optimal fit; however, the total nRMS value of 2.11, which is a generally acceptable tolerance for MT modelling, given the poor data quality. To further analyze the fit results, the nRMS was examined by frequency for each profile and component, as shown in Fig. 7. The results reveal that nRMS variations are well distributed across both high and low frequencies. Some fitting curves of apparent resistivity and phase for representative stations are shown in Fig. S8 of the Supporting Material. These results reinforce confidence in the reliability and robustness of the obtained models.

3.7. Depth sensibility test

The stations primarily located in Profile 2 do not reach periods as long as those in profiles 1 and 3. Therefore, a sensitivity test was conducted to evaluate the reliability of the depth resolution for each profile. This test involved inserting a superconducting feature (10^{-8} Ωm) into the final model at various depths. Padilha et al. (2013) applied this procedure to study sensitivity in a 2-D inversion model in central Brazil. In our case, the superconducting layer was designed to cover a significant area of each profile, with depths ranging from 10 to 100 *km* in 10 *km* intervals. The forward response of the perturbed model was calculated, and the nRMS error was compared to that of the final inversion model at each station. An nRMS error equal to that of the inversion model indicates that the maximum depth of penetration has not yet been reached. By progressively reducing the depth of the conductor, a depth was identified at which the nRMS error increased. To interpret the models consistently and with geological significance, a grid interpolation was estimated based on the maximum resolution depths from each station. The depth at which the model has no sensitivity is represented in the models in Fig. 8 as a whitened area.

3.8. Resistivity models

The models performed for each of the three profiles are shown in

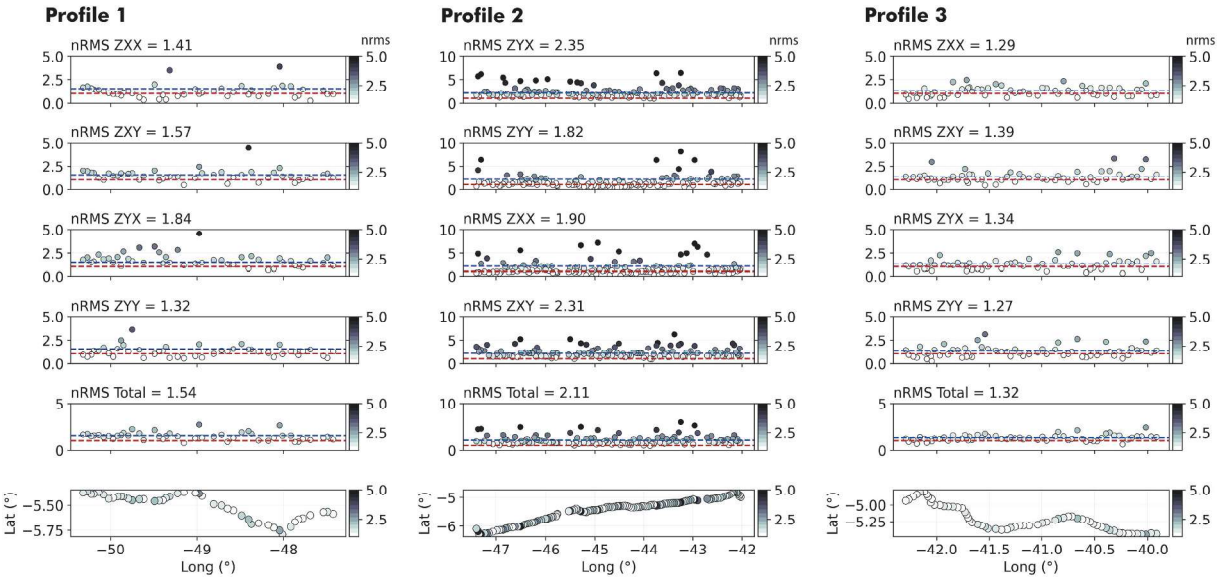


Fig. 6. Data fit for station-by-station and component-by-component analysis for each profile. The nRMS values obtained for each component are displayed at the top of each diagram. The red and blue dashed lines in each panel represent a fit equal to 1 and the total fit for each profile, respectively. Note the good fit in most stations of Profiles 1 and 3. The overall fit in Profile 2 is quite acceptable, despite some stations exhibiting a more significant misfit depending on the impedance tensor component analyzed.

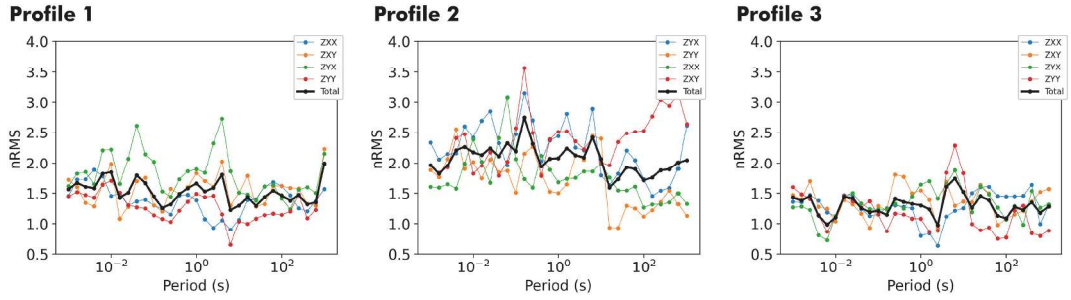


Fig. 7. Analysis of the fit by frequency and component for each profile.

Fig. 8. Resistive and conductive anomalies observed in the models and their tectonic implications are explained below. Conductive anomalies are represented by warm colors, while resistive anomalies are depicted in cool colors.

3.8.1. Profile 1 (West profile)

The resistivity model of profile 1 (Fig. 8a) reveals significant lateral resistivity variations at crustal and upper mantle depth, supporting the concept of the amalgamation of distinct tectonic units. In the Amazonian Craton, a series of conductive features is observed at ~ 10 *km*, suggesting the presence of an intracrustal detachment zone (Bai and Meju, 2003). These anomalies are likely associated with a significant change in mechanical behaviour within the transition zone between the upper and lower crust, facilitating the redistribution of tectonic stress during phases of compression or extension (Jödicke, 1992). Beneath MT253 station, a subvertical resistive anomaly is identified, extending from the surface to depths of approximately 40 *km*. This resistive structure is spatially aligned with the Quatipuru suture zone, which does not exhibit the broad low-resistivity structure typically expected for a suture zone. This behaviour can be attributed to the brittle nature of the region's material, which concentrates deformation within a narrow zone. The limited presence of organic material and sediments transported during the collision process may also contribute to the increase in resistivity.

The central segment of the profile corresponds to the Araguaia Belt, bounded by the Quatipuru suture zone to the west and the Araguaia fault zone to the east. Within this belt, two isolated conductivity features are detected at mid-crust depth (CF1 and CF2), interpreted as sediments incorporated into the crust during the orogenic formation process. In the Parnaíba block, a shallow surface conductive layer is observed, corresponding to the sedimentary sequence, which gradually deepens towards the east (towards the depocentre). This layer overlies a resistive domain associated with the cratonic basement of the Parnaíba Basin. The bottom of this resistive region coincides with the maximum depth of the Quatipuru suture zone, marking a transitional boundary between the brittle behaviour of the crust and the ductile properties of the upper mantle.

3.8.2. Profile 2 (Central profile)

In the central part of Profile 2 (Fig. 8b), within the region corresponding to the Teresina block, we identify a homogeneous and dominantly conductive domain. In contrast, the Grajaú block exhibits a resistive electrical behaviour. The boundary between the two blocks, an elongated conductive anomaly is observed, extending from the surface to the mid-crust, labelled as C1. Beneath the MT064 station, we identify a subvertical boundary that reveals a marked lateral contrast between the conductive domain of the Teresina block and the resistive block of the Borborema Province. This boundary correlates with the trace of the Transbrasiliano Lineament proposed by Daly et al. (2014).

3.8.3. Profile 3 (East profile)

The model for Profile 3 (Fig. 8c) shows a resistive domain at its western extremity, referred to as R1. This domain spans much of the region and reaches a depth of approximately 40 *km*. Two conductive zones flank R1, highlighting a sharp resistivity contrast resulting from the juxtaposition of lithospheric blocks with distinct conductive properties. In the central section of the model, the trace of the Transbrasiliano Lineament (TBL) according to De Castro et al. (2014) is identified. This boundary is inferred from gravimetric and magnetic data and separates a resistive domain from a conductive one. To the east of the TBL, between stations MT043 and MT033, an elongated conductive structure, labelled C2, stands out. This anomaly bears a strong resemblance to a structure with similar geometry and resistivity characteristics described in the magnetotelluric study by Padilha et al. (2017) in the northern Borborema Province. The authors interpret this feature as a cryptic suture concealed beneath the sediments of the Parnaíba Basin, formed during the amalgamation of blocks that shaped the Borborema Province in its Neoproterozoic evolution. Further east, the model reveals a succession of conductive and resistive features within the crust depth. These patterns reflect block accretion processes, as described by Jones (1992) and Unsworth (2010).

3.9. Conductance

One of the primary challenges in interpreting magnetotelluric models is determining the resistivity values associated with anomalies. Given that the MT method is more sensitive to conductive rather than resistive structures, it may be more appropriate to utilize conductance—defined as the product of conductivity and thickness—when assessing bulk conductivity across different structural scales within the Earth, particularly in the upper, middle, and lower crust. Thus, we conducted a study of conductance across three profiles covering upper crustal (0–20 *km*) and lower crustal depth (20–40 *km*). The results are illustrated in Fig. 9.

Within the Amazonian Craton at 0 and 20 *km* depth (Profile 1), conductance analysis reveals highly conductive structures with values ranging from 400 to 2500 S. In contrast, between the Quatipuru Suture Zone (QSZ) and the Araguaia Fault Zone (AFZ), which corresponds to the Araguaia Belt, a heterogeneous domain is observed, featuring both conductive and resistive structures. In the Grajaú Block, a slightly more uniform conductive domain is identified. At depths of 20 to 40 *km*, the geoelectric distribution also shows distinct conductance values along the profile, providing evidence of the amalgamation of the Amazonian Craton, the Araguaia Belt, and the Grajaú block.

In Profile 2, at depths of 0 to 20 km, highly concentrated conductive structures are identified beneath the MT stations distributed in the central part of the profile. In contrast, at depths of 20 to 40 *km*, three distinct geoelectric domains are observed: a central conductive domain flanked by resistive domains at the extremes, to the west by the Barra do Corda and to the east by the TLB. This behaviour reveals the amalgamation of the Grajaú block and the Teresina block. Porto et al. (2022) introduce the term "Barra do Corda" as an orogen representing the transition zone between the Grajaú and Teresina blocks.

In Profile 3, at depths of 0–20 *km*, conductance analysis reveals a heterogeneity of conductive and resistive anomalies along the profile. At

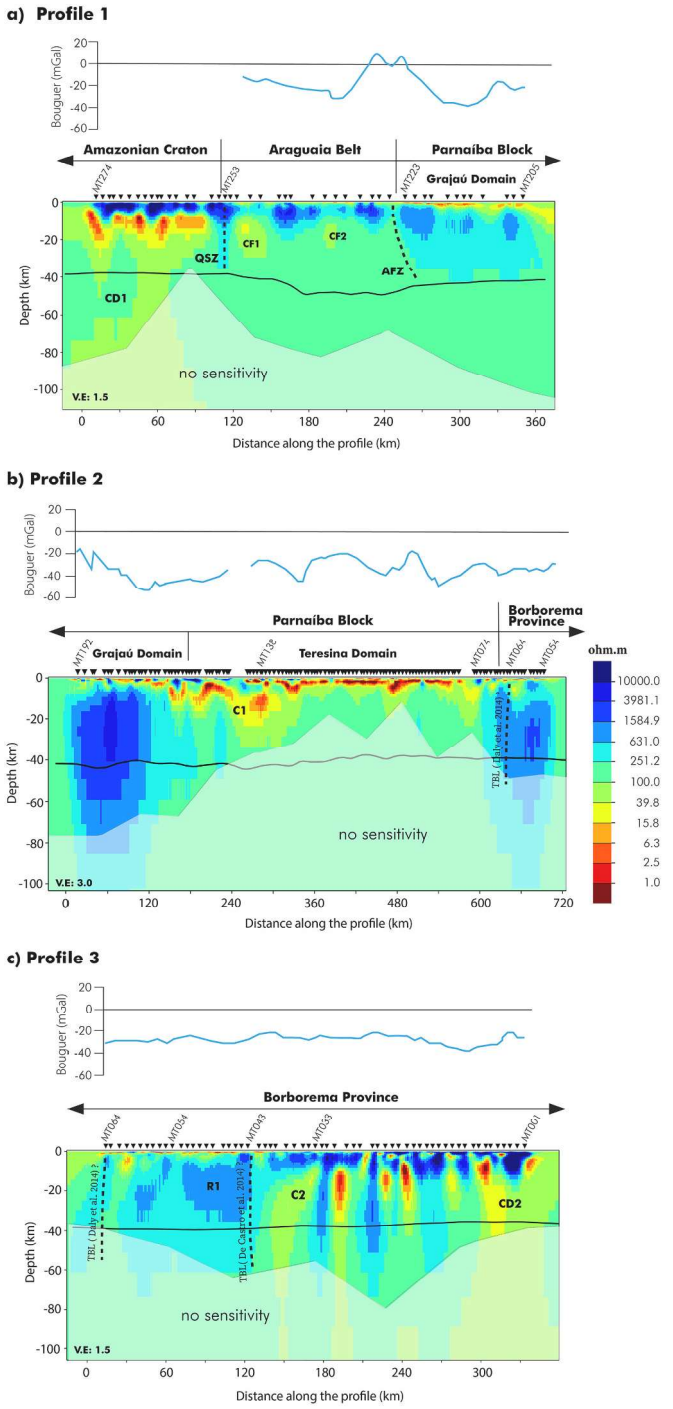


Fig. 8. Vertical sections of the 3-D resistivity model along the three profiles. The inverted triangles at the top of each model represent the MT stations, with some station names included for interpretative purposes. Surface limits of the geological domains are indicated. At the top of each model, variations in the Bouguer anomaly with the long-wavelength component removed are shown, as derived from Tozer (2017). The solid black line displayed over each resistivity model indicates the depth of the Moho, obtained from Fig. 5b. The conductive domains CD1 and CD2 correspond to conductive regions located in the lower crust and upper mantle depths, as discussed in the text. Conductor C1 corresponds to the suture zone between the Grajaú and Teresina domains. The R1 anomaly and the CF1, CF2, and C2 anomalies represent resistive and conductive features, respectively, which are analyzed in the text. The abbreviations QSZ and AFZ refer to the Quatipuru suture zone and Araguaia fault zone, respectively. The area marked as "no sensitivity" is derived from the sensitivity analysis applied. Refer to the text for further details.

depths of 20 to 40 *km*, a resistive domain is observed between the two interpretations of the Transbrasiliano Lineament, along with a heterogeneous domain at the eastern end of the profile. These geoelectric characteristics indicate that the eastern end of the profile shows significant tectonic deformation caused by accretion events during the formation of the Borborema Province. These deformations are associated with the presence of north-south-oriented faults and suture zones, concealed beneath the Phanerozoic sediments of the Parnaíba Basin. The results suggest that these processes did not impact the western end of the profile, although the reasons behind this apparent stability remain unclear. This interpretation appears plausible when considering that this region exhibits conductance values between 40 and 400 S, which are typical of tectonically stable areas (Jones, 1992). In contrast, tectonically active regions, such as the Tibetan Plateau, display significantly higher conductance values (Li et al., 2003).

4. Discussion/tectonic implications

When analysing the inversion models of each profile, we aim for an integrated interpretation of all identified resistive and conductive anomalies in the models. At the crustal and upper mantle depths, various explanations exist for interpreting conductive regions, including the presence of free aqueous fluids, partial melting, graphite, metallic sulphides, as well as hydrogen diffusion in upper mantle minerals (Jones, 1992; Nover, 2005). Conductive regions are generally associated with extensively deformed areas (shear and suture zones) that exhibit thermal elevation, mineralisation, or metasomatism, whereas resistive regions tend to be linked to stable cratons, volcanic-plutonic complexes, or oceanic lithosphere (see reviews by Jones, 1992; Unsworth, 2010; Selway, 2014). The depth of the Moho in the Parnaíba Basin was determined based on a compilation of seismic data, and the resulting map is shown in Fig. 5b. The elaboration of this map is described in Text S2 of the Supplementary Material. Likewise, the Bouguer anomaly and Total Magnetic Field maps, derived from aerogravimetric and aeromagnetic data acquired by the Agência Nacional do Petróleo, are presented in Fig. 5c and d, respectively.

4.1. Amazonian Craton and Borborema Province resistivity signatures

Two conductivity domains are identified in the upper mantle depth of the Amazonian Craton (CD1) and the westernmost edge of the Borborema Province (CD2), which deviates from the resistivity values typically observed in continental shields (Heinson, 1999). In the Amazonian Craton, V_p wave velocities of 8.0 km/s at upper mantle depth have been reported (Soares et al., 2018), similar to those observed by Soares et al. (2006) in central Brazil. Both groups of authors suggest that these velocities may be associated with a lithospheric root of likely mafic-ultramafic composition. The reduction in resistivity values could be explained by several factors. One such factor is the presence of water in the upper mantle of the Amazonian Craton. Small amounts of water (hydrogen) dissolved in minerals such as olivine can significantly lower electrical resistivity. However, this raises challenges related to fluid residence time, as stable continental crust requires a recharge and sealing mechanism to maintain fluid content (Selway, 2014). Other potential factors include the presence of graphite, sulphides, and partial melting. Graphite and sulphides, in particular, are associated with increased conductivity in the lower crust and/or upper mantle, especially in contexts such as terrane boundaries, suture zones, faults or orogenic zones. These are often interpreted as deeply trapped metasedimentary rocks rich in graphite or sulphides. In the case of the conductive domain beneath the eastern part of the Amazonian Craton, small amounts of interconnected graphite could significantly enhance overall conductivity. However, evidence supporting the existence of extensive regions of interconnected graphite remains limited (Glover, 1996). Furthermore, interpreting low resistivity in terms of sulphides would require concrete evidence of their occurrence in the study area,

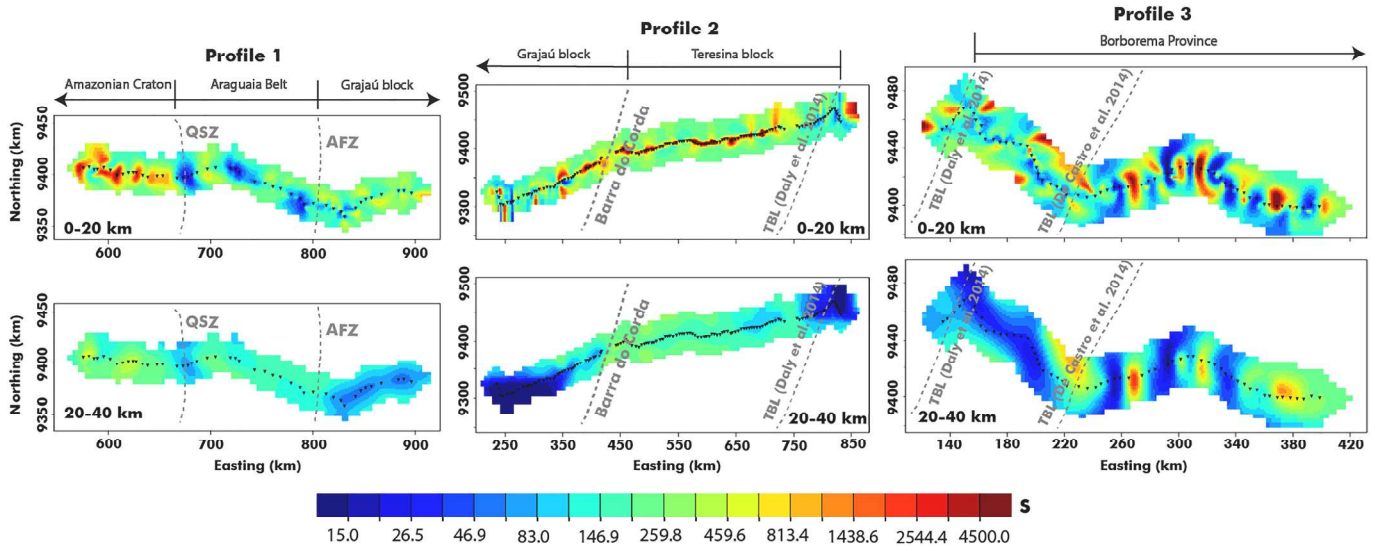


Fig. 9. Conductance models for each profile at upper crustal (0–20 *km*) and lower crustal depth (20–40 *km*). Labels: QSZ-Quatipuru shear zone, AFZ-Araguaia shear zone.

which is not the case here. Thus, to explain the conductive domain CD1, partial melting is a plausible explanation, though this would require an influx of molten material associated with rifting process. A rifting process would imply the existence of a deep mantle plume capable of causing lithospheric thinning, uplift, and intraplate volcanism. While this hypothesis cannot be entirely dismissed, there is limited evidence of significant volcanic activity in this region. Conversely, crustal delamination represents a more consistent hypothesis, especially considering that the lithospheric domain of the Amazonian Craton displays a relatively shallow Moho and thickening in the Araguaia belt and in the Quatipuru suture zone (see Fig. 8a), where it also coincides with gravity highs that could be explained by igneous intrusions in the lower crust. This process could be associated with the replacement of delaminated lithosphere by more fertile, volatile-rich sublithospheric mantle material. Similar interpretations of high conductivity in the upper mantle have been reported in regions presumed to have undergone delamination, such as southern India (Rao and Prasad, 2006), central Brazil (Dutra et al., 2024; Padilha et al., 2013; Bologna et al., 2006), and the western Mediterranean (Rosell et al., 2011).

The conductive domain CD2, located at the easternmost edge of the Borborema Province at upper mantle depths, exhibits a more pronounced conductive signature compared to the CD1 domain. This region coincides with the Jaguaribe domain within the Borborema Province, where lithospheric thinning is observed (Agurto-Detzel et al., 2017). A magnetotelluric (MT) study conducted by Padilha et al. (2013) in the northwestern part of the Borborema Province identified this conductive anomaly and attributed it to extensional events during the Paleoproterozoic, followed by compressional events in the Neoproterozoic. The authors suggest that the increase in conductivity in the upper mantle is due to the introduction of carbon transported by subducted plates. West of this region, the 3-D resistivity model reveals a sequence of alternating resistive and conductive anomalies, indicative of a collisional and accretionary region, as highlighted in the conductance models. The presence of mid-crustal conductors between MT stations MT033 and MT001, may be attributed to multiple processes, including the meta morphism of organic-rich sediments trapped during *syn-* and post-orogenic stage, as well as deeper mantle-drive mechanisms such as ancient hotpost activity that introduced carbon and fluid into the lithosphere. Both scenarios result in the formation of graphite-bearing networks, which enhance conductivity and may persist over geological timescales. However, while these interpretations are supported by analogous findings in other cratonic regions (Kusham et al., 2019; Kusham et al., 2018), direct evidence for extensive interconnected graphite remains limited. Thus, the proposed models should be considered plausible but would benefit from additional indirect constraints or comparative studies to strengthen the interpretation.

4.2. *Parnaíba block*

At the western end of Profile 2, a resistive domain is identified, covering much of the region corresponding to the Grajaú block. This domain extends from the base of the Phanerozoic sedimentary sequences to approximately 80 *km* depth. This region coincides with a short-wavelength gravity low and a minimum in the total magnetic field (Figs. 5c, d). This can be interpreted as an indication of lateral density variations in the crust, with the presence of localised mafic intrusions of high density and high conductivity within the crust, associated with magmatism from the Mosquito Formation. Soares et al. (2018) from WARR data identified high mantle velocity and high-velocity lowermost in this crustal region, interpreted as linked to the intrusion of mafic material into the crust underlying the Grajaú domain. This region also coincides with seismic Vp/Vs ratios ranging from 1.76 to 1.79 and 1.77 to 1.78, observed by Schiffer et al. (2021) and Coelho et al. (2018), respectively. These values are explained by widespread small-scale mafic intrusions in the crust (Lima et al., 2019), where the Moho depth in this region shows variations >41 *km*. In the Teresina block, a conductive domain is identified at crustal and upper mantle depths. This region is characterized by higher long-wavelength gravity values and a stronger total magnetic field compared to the Grajaú domain. This implies an increase in deep density, which could be explained by a dense lower crust (Tozer et al., 2017), a relatively enriched mantle, or potentially deeper tectonic process – such as those interpreted in the Madurai Block – where low resistivity zones are associated with eclogitized subducted lithosphere (Naganjaneyulu and Santosh, 2010). Thus, the observed resistivity contrast between the Grajaú and Teresina domains could represent a fossil suture or imbricate thrust system, analogous to accretionary structures beneath other Gondwana related crustal blocks. This anomaly coincides with an area of mid-crustal reflectivity (MRC) identified in regional seismic data (Daly et al., 2014), interpreted as evidence of a lower crustal magmatic intrusion (Tozer et al., 2017), or as a remnant of a paleo-suture zone between the two blocks (Porto et al., 2022). The Vp/Vs ratio observed in this region ranges from 1.73 to 1.76 (Schiffer et al., 2021), with the lowest value (1.73) unexpectedly located in the westernmost part of the Teresina

block, where evidence of the MRC has been found. The loss of resistive signatures within the Teresina block could be attributed to post-collisional magmatic residues introducing conductive components into the crustal and lithospheric structure or changes in the electrical properties of the rocks resulting from geodynamic events associated with the onset of basin subsidence.

The basalts of the Mosquito Formation have an initial isotopic composition of $^{87}Sr/^{86}Sr$ and $^{143}Nd/^{144}Nd$ similar to that of the Sardinha Formation (Oliveira et al., 2018). Both magmatic formations are associated with an enrichment in large ion lithophile and high field strength elements relative to primitive mantle compositions (Oliveira et al., 2018). Magmatism in the Parnaíba Basin could be attributed to localised conditions of a hotter mantle due to the combined effects of edge-driven convection and large-scale mantle heating beneath the Gondwana supercontinent. Recently, Guimarães et al. (2022) provided an updated geothermal database and new mapping of terrestrial heat flow across Brazil. The corresponding map for the Parnaíba Basin is shown in Fig. S9 of the Supporting Material. According to these results, an increase in heat flow is observed in the central part of the basin, which may be explained by the presence of a deep heat source.While the involvement of a mantle plume with isotopic characteristics similar to the asthenosphere cannot be ruled out as a possible source or heat provider, this hypothesis appears less likely due to the relatively constant Moho and lithospheric depth observed in the Parnaíba block (around 150 *km*; Agurto-Detzel et al., 2017). The fact that the Grajaú Block maintains a resistivity behaviour distinct from that of the Teresina Block suggests that the Sardinha Formation experienced more prolonged and voluminous magmatic pulses than the Mosquito Formation. This could also explain the slightly shallower Moho depth in the Teresina domain compared to the Grajaú domain. However, the hypothesis of extensional events and the opening of the South Atlantic Ocean linked to the formation of the Sardinha Formation (Fodor et al., 1990) cannot be ruled out, where there is also evidence of crustal stretching in the Borborema Province (Lima et al., 2015; Luz et al., 2015). These results support the interpretation that the basement consists of two tectonic blocks with different ages and petrography, contradicting the concept of a stable craton (Daly et al., 2014; De Castro et al., 2014; Caxito et al., 2020; Ganade de Araujo et al., 2014; Caxito et al., 2021; Ganade et al., 2021).

The conductor C1 represents the suture zone between the Teresina and Grajaú blocks, whose conductivity, considering its elongated geometry and narrow thickness within the stable deep crust, suggests the presence of an interconnected network of graphite, fluid and metasomatic processes, similar to those imaged in a comparable tectonic context within the Dharwar Craton (Kusham et al., 2021). The eastward-dipping orientation of this conductor differs from the resistive model observed by Solon et al. (2018) but aligns with the seismic models of Soares et al. (2018) and Schiffer et al. (2021), as well as the geological interpretation by Porto et al. (2022) regarding the collisional events that led to the formation of Western Gondwana. The geometry and orientation of this conductive feature provides a primary constraint on the polarity of the collision zone. Thus, we suggest that this structure indicates eastward subduction polarity, during likely during the Palaeoproterozoic. The Parnaíba block would have been established as a single unit following the collision of the Grajaú and Teresina blocks in the late Neoproterozoic and early Paleozoic. The Grajaú domain likely separated from the Amazonian-West African Craton (Porto et al., 2022), while the Teresina domain is thought to have detached from the São Francisco-Congo Craton during the ribbon-like decratonisation process (Caxito et al., 2020).

5. Conclusions

The 3-D electrical resistivity models presented here, derived from MT data, provide new insights into the structure and evolution of the Parnaíba Basin. They offer compelling evidence about the basin's structure:

The MT models in this study reveal laterally differentiated geoelectrical behaviour at crustal and upper mantle depths, evidencing the amalgamation of distinct tectonic blocks from west to east: the Amazonian Craton, the Parnaíba block, and the Borborema Province.

Magmatic records along the Parnaíba block suggest more intense and voluminous magmatic pulses in the eastern part of the block, corresponding to the Teresina domain. This likely caused the loss of its resistive signature. Conversely, in the western part of the block, corresponding to the Grajaú domain, magmatism appears to have been less intense and unaffected by the Cretaceous extensional events linked to the opening of the South Atlantic Ocean.

Our results support the existence of marine pathways along the Transbrasiliano Lineament and the Araguaia Belt, which were closed during the assembly of western Gondwana in the Neoproterozoic.

The resistivity models presented here support the dynamic model of basin formation, involving a collage of allochthonous terranes, as characterized by Daly et al. (2019) within the framework of the Wilson Cycle. Our models support the concept of mechanical subsidence caused by the emplacement of a dense igneous body in the lower crust or upper mantle, related to plume activity during the lifespan of a supercontinent.

References

Agurto-Detzel, H., Assumpção, M., Bianchi, M., Pirchiner, M., 2017. Intraplate seismicity in mid-plate South America: correlations with geophysical lithospheric parameters. Geol. Soc. Lond. Spec. Publ. 432 (1), 73–90.

Arora, B.R., Padilha, A.L., Vitorello, I., Trivedi, N.B., Fontes, S.L., Rigoti, A., Chamalaun, F.H., 1999. 2-D geoelectrical model for the Parnaíba Basin conductivity

anomaly of Northeast Brazil and tectonic implications. Tectonophysics 302 (1–2), 57–69.
Arthaud, M.H., Caby, R., Fuck, R.A., Dantas, E.L., Parente, C.V., 2008. Geology of the northern Borborema Province, and its correlations with Nigeria, NW Africa. In: Pankhurst, R.J., Trouw, R.A.J., Brito Neves, B.B., De Wit, M.J. (Eds.), West Gondwama: Pre-Cenozoic Correlations across the South Atlantic Region, Geological Society of London, Special Publications, vol. 294, pp. 49–67.
Assis, A.P., Porto, A.L., Schmitt, R.S., Linol, B., Medeiros, S.R., Martins, F.C., Silva, D.S., 2019. The Ordovician-Silurian tectono-stratigraphic evolution and paleogeography of eastern Parnaiba Basin, NE Brazil. J. S. Am. Earth Sci. 95, 102241.
Bai, D., Meju, M.A., 2003. Deep structure of the Longling–Ruili fault underneath Ruili basin near the eastern Himalayan syntaxis: insights from magnetotelluric imaging. Tectonophysics 364 (3–4), 135–146.
Bedrosian, P.A., Feucht, D.W., 2014. Structure and tectonics of the northwestern United States from EarthScope USArray magnetotelluric data. Earth Planet. Sci. Lett. 402, 275–289.
Bologna, M.S., Padilha, A.L., Vitorello, Í., Fontes, S.L., 2006. Tectonic insight into a pericratonic subcrustal lithosphere affected by anorogenic cretaceous magmatism in Central Brazil inferred from long-period Magnetotellurics. Earth Planet. Sci. Lett. 241 (3–4), 603–616.
Bologna, M.S., Nunes, H.O., Padilha, A.L., Vitorello, Í., Pádua, M.B., 2013. Anomalous electrical structure in the northwestern Paraná Basin, Brazil, observed with broadband magnetotellurics. J. S. Am. Earth Sci. 42, 74–82.
Brasse, H., Schäfer, A., Díaz, D., Alvarado, G.E., Muñoz, A., Mütschard, L., 2015. Deep-crustal magma reservoirs beneath the Nicaraguan volcanic arc, revealed by 2-D and semi 3-D inversion of magnetotelluric data. Phys. Earth Planet. Inter. 248, 55–62.
Brito Neves, B.B., Fuck, R.A., 2013. Neoproterozoic evolution of the basement of the South-American platform. J. S. Am. Earth Sci. 47, 72–89.
Brito Neves, B.B., Fuck, R.A., Cordani, U.G., 1984. Influence of basement structures on the evolution of the major sedimentary basins of Brazil: a case of tectonic heritage. J. Geodyn. 1 (3–5), 495–510.
Brito Neves, B.B., Fuck, R.A., Pimentel, M.M., 2014. The Brasiliano collage in South America: a review. Braz. J. Geol. 44 (3), 493–518.
Caldwell, T.G., Bibby, H.M., Brown, C., 2004. The magnetotelluric phase tensor. Geophys. J. Int. 158 (2), 457–469.
Caxito, F.D.A., Santos, L.C.M.D.L., Ganade, C.E., Bendaoud, A., Fettous, E.H., Bouyo, M. H., 2020. Toward an integrated model of geological evolution for NE Brazil-NW Africa: the Borborema Province and its connections to the Trans-Saharan (Benino-Nigerian and Tuareg shields) and Central African orogens. Braz. J. Geol. 50, e20190122.
Caxito, F.A., Basto, C.F., de Lira Santos, L.C.M., Dantas, E.L., de Medeiros, V.C., Dias, T. G., Barrote, V., Hagemann, S., Alkmin, A.R., Lana, C., 2021. Neoproterozoic magmatic arc volcanism in the Borborema Province, NE Brazil: possible flare-ups and lulls and implications for western Gondwana assembly. Gondwana Res. 92, 1–25.
Cherevatova, M., Smirnov, M.Y., Korja, T., Pedersen, L.B., Ebbing, J., Gradmann, S., Becken, M., MaSca Working Group, 2015. Electrical conductivity structure of north-west Fennoscandia from three-dimensional inversion of magnetotelluric data. Tectonophysics 653, 20–32.
Christensen, N.I., Mooney, W.D., 1995. Seismic velocity structure and composition of the continental crust: a global view. J. Geophys. Res. Solid Earth 100 (B6), 9761–9788.
Coelho, D.L., Julià, J., Rodríguez-Tribaldos, V., White, N., 2018. Deep crustal architecture of the Parnaíba basin of NE Brazil from receiver function analysis: implications for basin subsidence. Geol. Soc. Lond. Spec. Publ. 472 (1), 83–100.
Cordani, U.G., Pimentel, M.M., Ganade de Araújo, C.E., Basei, M.A., Fuck, R.A., Girardi, V.A., 2013. Was there an Ediacaran Clymene Ocean in Central South America? Am. J. Sci. 313 (6), 517–539.
Daly, M.C., Andrade, V., Barousse, C.A., Costa, R., McDowell, K., Piggott, N., Poole, A.J., 2014. Brasiliano crustal structure and the tectonic setting of the Parnaíba basin of NE Brazil: results of a deep seismic reflection profile. Tectonics 33 (11), 2102–2120.
Daly, M.C., Fuck, R.A., Julià, J., Macdonald, D.I., Watts, A.B., 2018. Cratonic Basin Formation: A Case Study of the Parnaíba Basin of Brazil, Vol. 472, No. 1. The Geological Society of London, pp. 1–15.
Daly, M.C., Tozer, B., Watts, A.B., 2019. Cratonic basins and the Wilson cycle: a perspective from the Parnaíba Basin, Brazil. Geol. Soc. Lond. Spec. Publ. 470 (1), 463–477.
De Castro, D.L., Fuck, R.A., Phillips, J.D., Vidotti, R.M., Bezerra, F.H., Dantas, E.L., 2014. Crustal structure beneath the Paleozoic Parnaíba Basin revealed by airborne gravity and magnetic data, Brazil. Tectonophysics 614, 128–145.
De Castro, D.L., Bezerra, F.H., Fuck, R.A., Vidotti, R.M., 2016. Geophysical evidence of pre-sag rifting and post-rifting fault reactivation in the Parnaíba basin, Brazil. Solid Earth 7 (2), 529–548.
De Castro, D.L., Oliveira, D.C., Hollanda, M.H.B., 2018. Geostatistical interplay between geophysical and geochemical data: mapping litho-structural assemblages of Mesozoic igneous activities in the Parnaíba Basin (NE Brazil). Surv. Geophys. 39, 683–713.
De Wit, M.J., Stankiewicz, J., Reeves, C., 2008. Restoring Pan-African-Brasiliano connections: more Gondwana control, less trans-Atlantic corruption. Geol. Soc. Lond. Spec. Publ. 294 (1), 399–412.
Dutra, A.C., Bologna, M.S., Dragone, G.N., 2024. The electrical structure of the lithosphere in the southeastern margin of the Amazonian craton: Contribution to West Gondwana tectonics. Precambrian Res. 410, 107477.
Egbert, G.D., 1997. Robust multiple-station magnetotelluric data processing. Geophys. J. Int. 130, 475–496.
Egbert, G.D., Kelbert, A., 2012. Computational recipes for electromagnetic inverse problems. Geophys. J. Int. 189 (1), 251–267.
Feng, M., Van der Lee, S., Assumpção, M., 2007. Upper mantle structure of South America from joint inversion of waveforms and fundamental mode group velocities of Rayleigh waves. J. Geophys. Res. Solid Earth 112 (B4).
Fodor, R.V., Sial, A.N., Mukasa, S.B., McKee, E.H., 1990. Petrology, isotope characteristics, and K-Ar ages of the Maranhão, northern Brazil, Mesozoic basalt province. Contrib. Mineral. Petrol. 104, 555–567.
Fuck, R.A., Dantas, E.L., Pimentel, M.M., Botelho, N.F., Armstrong, R., Laux, J.H., Junges, S.L., Soares, J.E., Praxedes, I.F., 2014. Paleoproterozoic crust-formation and reworking events in the Tocantins Province, Central Brazil: a contribution for Atlantica supercontinent reconstruction. Precambrian Res. 244, 53–74.
Ganade de Araujo, C.E., Rubatto, D., Hermann, J., Cordani, U.G., Caby, R., Basei, M.A., 2014. Ediacaran 2,500-km-long synchronous deep continental subduction in the West Gondwana Orogen. Nat. Commun. 5 (1), 5198.
Ganade, C.E., Weinberg, R.F., Caxito, F.A., Lopes, L.B., Tesser, L.R., Costa, I.S., 2021. Decratonization by rifting enables orogenic reworking and transcurrent dispersal of old terranes in NE Brazil. Sci. Rep. 11 (1), 5719.
Garcia, X., Julià, J., Nemocón, A.M., Neukirch, M., 2019. Lithospheric thinning under the Araripe Basin (NE Brazil) from a long-period magnetotelluric survey: constraints for tectonic inversion. Gondwana Res. 68, 174–184.
Glover, P.W.J., 1996. Graphite and electrical conductivity in the lower continental crust: a review. Phys. Chem. Earth 21 (4), 279–287.
Góes, A.M., Feijó, F.J., 1994. Parnaiba Basin; Bacia do Parnaiba. Boletim de Geociências da PETROBRAS, p. 8.
Góes, A.M., de Souza, J.M.P., Teixeira, L.B., 1990. Estágio exploratório e perspectivas petrolíferas da Bacia do Parnaíba. Boletim de Geociencias da PETROBRAS 4 (1), 55–64.
Guimarães, S.N.P., Prado, E.M.G., Vieira, F.P., Lacasse, C.M., da Silva Rocha, N., de Jesus, B.L., de Souza Filho, O.A., 2022. Updated mapping of terrestrial heat flow in Brazil. J. S. Am. Earth Sci. 113, 103627.
Hautot, S., Tarits, P., Whaler, K., Le Gall, B., Tiercelin, J.J., Le Turdu, C., 2000. Deep structure of the Baringo Rift Basin (Central Kenya) from three-dimensional magnetotelluric imaging: Implications for rift evolution. J. Geophys. Res. Solid Earth 105 (B10), 23493–23518.
Heinson, G., 1999. Electromagnetic studies of the lithosphere and asthenosphere. Surv. Geophys. 20, 229–255.
Ingersoll, R.V., 2011. Tectonics of sedimentary basins, with revised nomenclature. Tectonics of sedimentary basins. Rec. Adv. 1–43.
Jödicke, H., 1992. Water and graphite in the Earth's crust—an approach to interpretation of conductivity models. Surv. Geophys. 13 (4), 381–407.
Jones, A.G., 1992. Electrical conductivity of the continental lower crust. Continental Lower Crus 81–143.
Kelbert, A., Meqbel, N., Egbert, G.D., Tandon, K., 2014. ModEM: A modular system for inversion of electromagnetic geophysical data. Comput. Geosci. 66, 40–53.
Kirkby, A.L., Zhang, F., Peacock, J., Hassan, R., Duan, J., 2019. The MTPy software package for magnetotelluric data analysis and visualisation. J. Open Source Softw. 4 (37), 1358. https://doi.org/10.21105/joss.01358.
Kotschoubey, B., Hieronymus, B., de Albuquerque, C.A.R., 2005. Disrupted peridotites and basalts from the Neoproterozoic Araguaia belt (northern Brazil): remnants of a poorly evolved oceanic crust? J. S. Am. Earth Sci. 20 (3), 211–230.
Kusham, A.P., Pradeep Naick, B., Naganjaneyulu, K., 2018. Lithospheric architecture in the Archaean Dharwar craton, India: a magnetotelluric model. J. Asian Earth Sci. 163, 43–53.
Kusham, A.P., Pradeep Naick, B., Naganjaneyulu, K., 2019. Crustal and lithospheric mantle conductivity structure in the Dharwar craton, India. J. Asian Earth Sci. 176, 253–263.
Kusham, A.P., Pradeep Naick, B., Pratap, A., Naganjaneyulu, K., 2021. Magnetotelluric 3-D full tensor inversion in the Dharwar craton, India: mapping of subduction polarity and kimberlitic melt. Phys. Earth Planet. Inter. 315, 106708.
Li, S., Unsworth, M.J., Booker, J.R., Wei, W., Tan, H., Jones, A.G., 2003. Partial melt or aqueous fluid in the mid-crust of Southern Tibet? Constraints from INDEPTH magnetotelluric data. Geophys. J. Int. 153 (2), 289–304.
Li, Z.X., Bogdanova, S., Collins, A.S., Davidson, A., De Waele, B., Ernst, R.E., Fitzsimons, I.C.W., Fuck, R.A., Gladkochub, D.P., Jacobs, J., Karlstrom, K.E., Lu, S., Natapov, L.M., Pease, V., Pisarevsky, S.A., Thrane, K., Vernikovsky, V., Vernikovsky, V., 2008. Assembly, configuration, and break-up history of Rodinia: a synthesis. Precambrian Res. 160 (1–2), 179–210.
Lima, M.V.A., Berrocal, J., Soares, J.E., Fuck, R.A., 2015. Deep seismic refraction experiment in Northeast Brazil: new constraints for Borborema province evolution. J. S. Am. Earth Sci. 58, 335–349.
Lima, M.V.A., Stephenson, R.A., Soares, J.E.P., Fuck, R.A., de Araújo, V.C., Lima, F.T., Rocha, F.A., 2019. Characterization of crustal structure by comparing reflectivity patterns of wide-angle and near vertical seismic data from the Parnaíba Basin, Brazil. Geophys. J. Int. 218 (3), 1652–1664.
Luz, R.M., Julià, J., do Nascimento, A. F., 2015. Crustal structure of the eastern Borborema Province, NE Brazil, from the joint inversion of receiver functions and surface wave dispersion: implications for plateau uplift. J. Geophys. Res. Solid Earth 120 (5), 3848–3869.
McKenzie, D., Rodríguez Tribaldos, V., 2018. Lithospheric heating by crustal thickening: a possible origin of the Parnaíba Basin. Geol. Soc. Lond. Spec. Publ. 472 (1), 37–44.
Meqbel, N., 2009. The Electrical Conductivity Structure of the Dead Sea Basin Derived from 2D and 3D Inversion of Magnetotelluric Data (Doctoral Dissertation).
Meqbel, N.M., Egbert, G.D., Wannamaker, P.E., Kelbert, A., Schultz, A., 2014. Deep electrical resistivity structure of the northwestern US derived from 3-D inversion of USArray magnetotelluric data. Earth Planet. Sci. Lett. 402, 290–304.
Miensopust, M.P., 2017. Application of 3-D electromagnetic inversion in practice: challenges, pitfalls and solution approaches. Surv. Geophys. 38, 869–933.

Naganjaneyulu, K., Santosh, M., 2010. The Cambrian collisional suture of Gondwana in southern India: a geophysical appraisal. J. Geodyn. 50 (3–4), 256–267.
Naganjaneyulu, K., Santosh, M., 2012. The nature and thickness of lithosphere beneath the Archean Dharwar Craton, southern India: a magnetotelluric model. J. Asian Earth Sci. 49, 349–361.
Nascimento, A.V., França, G.S., Chaves, C.A., Marotta, G.S., Assumpção, M., 2024. Unraveling Precambrian cratonic roots beneath South America: a contribution from surface wave tomography. Tectonophysics 230392.
Nover, G., 2005. Electrical properties of crustal and mantle rocks–a review of laboratory measurements and their explanation. Surv. Geophys. 26 (5), 593–651.
Oliveira, D.C., Mohriak, W.U., 2003. Jaibaras trough: an important element in the early tectonic evolution of the Parnaıba interior sag basin, Northern Brazil. Mar. Pet. Geol. 20 (3–4), 351–383.
Oliveira, A.L., Pimentel, M.M., Fuck, R.A., Oliveira, D.C., 2018. Petrology of Jurassic and Cretaceous basaltic formations from the Parnaíba Basin, NE Brazil: correlations and associations with large igneous provinces. Geol. Soc. Lond. Spec. Publ. 472 (1), 279–308.
Padilha, A.L., Vitorello, Í., Antunes, C.E., Pádua, M.B., 2015. Imaging three-dimensional crustal conductivity structures reflecting continental flood basalt effects hidden beneath thick intracratonic sedimentary basin. J. Geophys. Res. Solid Earth 120, 4702–4719. https://doi.org/10.1002/2014JB011657.
Padilha, A.L., Vitorello, I., Pádua, M.B., 2013. Deep conductivity structure beneath the northern Brasília belt, Central Brazil: evidence for a Neoproterozoic arc-continent collision. Gondwana Res. 23 (2), 748–758.
Padilha, A.L., Vitorello, Í., Pádua, M.B., Bologna, M.S., 2014. Electromagnetic constraints for subduction zones beneath the Northwest Borborema province: evidence for Neoproterozoic island arc–continent collision in Northeast Brazil. Geology 42 (1), 91–94.
Padilha, A.L., Vitorello, I., Pádua, M.B., Fuck, R.A., 2017. Cryptic signatures of Neoproterozoic accretionary events in Northeast Brazil imaged by magnetotellurics: implications for the assembly of West Gondwana. Tectonophysics 699, 164–177.
Paixão, M.A.P., Nilson, A.A., 2002. Fragmentos ofiolíticos da Faixa Araguaia: caracterização geológica e implicações tectônicas. Contrib. Geol. Amazôn. 3, 85–103.
Patro, P.K., Egbert, G.D., 2008. Regional conductivity structure of Cascadia: preliminary results from 3D inversion of USArray transportable array magnetotelluric data. Geophys. Res. Lett. 35 (20).
Patro, P.K., Egbert, G.D., 2011. Application of 3D inversion to magnetotelluric profile data from the Deccan Volcanic Province of Western India. Phys. Earth Planet. Inter. 187 (1–2), 33–46.
Porto, A., Daly, M.C., La Terra, E., Fontes, S., 2018. The pre-Silurian Riachão basin: a new perspective on the basement of the Parnaíba basin, NE Brazil. Geol. Soc. Lond. Spec. Publ. 472 (1), 127–145.
Porto, A., Carvalho, C., Lima, C., Heilbron, M., Caxito, F., La Terra, E., Fontes, S.L., 2022. The Neoproterozoic basement of the Parnaíba Basin (NE Brazil) from combined geophysical-geological analysis: a missing piece of the western Gondwana puzzle. Precambrian Res. 379, 106784.
Rao, V.V., Prasad, B.R., 2006. Structure and evolution of the Cauvery Shear Zone system, Southern Granulite Terrain, India: evidence from deep seismic and other geophysical studies. Gondwana Res. 10 (1–2), 29–40.
Rocha, N.S., Fontes, S.L., La Terra, E.F., Fuck, R.A., 2019. Lithosphere structures of the Parnaíba Basin and adjacent provinces revealed by deep magnetotelluric imaging. J. S. Am. Earth Sci. 92, 1–11.
Romero, G., La Terra, E.F., Panetto, L.P., Fontes, S.L., 2019. Upper crustal structures of the southeast edge of Parnaiba basin using 3D magnetotelluric data imaging. J. S. Am. Earth Sci. 96, 102392.
Rosell, O., Martí, A., Marcuello, À., Ledo, J., Queralt, P., Roca, E., Campanyà, J., 2011. Deep electrical resistivity structure of the northern Gibraltar Arc (western Mediterranean): evidence of lithospheric slab break-off. Terra Nova 23 (3), 179–186.
Rudnick, R.L., Fountain, D.M., 1995. Nature and composition of the continental crust: a lower crustal perspective. Rev. Geophys. 33 (3), 267–309.
Samrock, F., Kuvshinov, A., Bakker, J., Jackson, A., Fisseha, S., 2015. 3-D analysis and interpretation of magnetotelluric data from the Aluto-Langano geothermal field, Ethiopia. Geophys. J. Int. 202 (3), 1923–1948.
Schiffer, C., de Lima, M.V., Soares, J.E., Stephenson, R., de Araújo, V.C., Lima, F.T., Rocha, A.S., Trindade, C.R., Fuck, R.A., 2021. Vp/Vs ratios in the Parnaíba Basin from joint active-passive seismic analysis–Implications for continental amalgamation and basin formation. Tectonophysics 801, 228715.
Schmitt, R.D.S., Fragoso, R.D.A., Collins, A.S., 2018. Suturing Gondwana in the Cambrian: the orogenic events of the final amalgamation. Geol. Southwest Gondwana 411–432.
Schmitt, R.D.S., Trouw, R.A., Da Silva, E.A., de Jesus, J.V.M., da Costa, L.F.M., Passarelli, C.R., 2023. The Role of Crustal-Scale Shear Zones in SW Gondwana Consolidation–Transatlantic Correlation.
Seillé, H., Pous, J., Pedreira, D., Gallastegui, J., Romero-Ruiz, I., Pulgar, J.A., 2022. The crustal structure of the Cantabrian Mountains revealed by new magnetotelluric soundings. Tectonophysics 830, 229310.
Selway, K., 2014. On the causes of electrical conductivity anomalies in tectonically stable lithosphere. Surv. Geophys. 35, 219–257.
Simpson, F., Bahr, K., 2005. Practical Magnetotellurics. Cambridge University Press.
Siripunvaraporn, W., Egbert, G., Uyeshima, M., 2005. Interpretation of two-dimensional magnetotelluric profile data with three-dimensional inversion: synthetic examples. Geophys. J. Int. 160 (3), 804–814.
Soares, J.E., Berrocal, J., Fuck, R.A., Mooney, W.D., Ventura, D.B., 2006. Seismic characteristics of Central Brazil crust and upper mantle: a deep seismic refraction study. J. Geophys. Res. Solid Earth 111 (B12).
Soares, J.E., Stephenson, R., Fuck, R.A., De Lima, M.V., De Araújo, V.C., Lima, F.T., Rocha, A.S., Da Trindade, C.R., 2018. Structure of the crust and upper mantle beneath the Parnaíba Basin, Brazil, from wide-angle reflection–refraction data. Geol. Soc. Lond. Spec. Publ. 472 (1), 67–82.
Solon, F.F., Fontes, S.L., La Terra, E.F., 2018. Electrical conductivity structure across the Parnaíba Basin, NE Brazil. Geol. Soc. Lond. Spec. Publ. 472 (1), 109–126.
Spratt, J.E., Skulski, T., Craven, J.A., Jones, A.G., Snyder, D.B., Kiyan, D., 2014. Magnetotelluric investigations of the lithosphere beneath the central Rae craton, mainland Nunavut, Canada. J. Geophys. Res. Solid Earth 119 (3), 2415–2439.
Thiel, S., Goleby, B.R., Pawley, M.J., Heinson, G., 2020. AusLAMP 3D MT imaging of an intracontinental deformation zone, Musgrave Province, Central Australia. Earth Planets Space 72 (1), 98.
Tohver, E., Cawood, P.A., Rossello, E.A., Jourdan, F., 2012. Closure of the Clymene Ocean and formation of West Gondwana in the Cambrian: evidence from the Sierras Australes of the southernmost Rio de la Plata craton, Argentina. Gondwana Res. 21 (2–3), 394–405.
Torsvik, T.H., Cocks, L.R.M., 2013. Gondwana from top to base in space and time. Gondwana Res. 24 (3–4), 999–1030.
Torsvik, T.H., Van der Voo, R., Preeden, U., Mac Niocaill, C., Steinberger, B., Doubrovine, P.V., Van Hinsbergen, J.J., Domeier, M., Gaina, C., Tohver, E., Meert, J. G., McCausland, J.A., Cocks, L.R.M., 2012. Phanerozoic polar wander, palaeogeography and dynamics. Earth Sci. Rev. 114 (3–4), 325–368.
Tozer, B., 2017. Crustal Structure, Gravity Anomalies and Subsidence History of the Parnaíba Cratonic Basin, Northeast Brazil. PhD Thesis.. Univerisity of Oxford, Oxford.
Tozer, B., Watts, A.B., Daly, M.C., 2017. Crustal structure, gravity anomalies, and subsidence history of the Parnaíba cratonic basin, Northeast Brazil. J. Geophys. Res. Solid Earth 122 (7), 5591–5621.
Uchoa, E.B., Silva, N.C.V., Magini, C., Branco, R.M.G.C., Fuck, R.A., da Silva, F.M., Martins, J.A., Silva, C.R.M., 2020. Magnetotelluric transect across the São Luís cratonic fragment, the Gurupi belt and the Parnaíba basin, N-NE Brazil. J. S. Am. Earth Sci. 104, 102888.
Unsworth, M., 2010. Magnetotelluric studies of active continent–continent collisions. Surv. Geophys. 31 (2), 137–161.
Vaz, P.T., Wanderley Filho, J.R., Travassos, W.A.S., 2007. Bacia do parnaíba. Bol. Geociênc. PETROBRAS 15 (2), 253–263.
Watts, A.B., Tozer, B., Daly, M.C., Smith, J., 2018. A comparative study of the Parnaíba, Michigan and Congo cratonic basins. Geol. Soc. Lond. Spec. Publ. 472 (1), 45–66.

Supporting Material for

Magnetotelluric imaging of the Parnaíba Basin: Implications to the West Gondwana formation

Gonzalo Romero-Beltran[1], Emanuele F. La Terra[1], Liliane P. Panetto[1], Hoël Seillé[2],

[1] National Observatory, Department of Geophysics, Rua Jose Cristino 77, Rio de Janeiro-Brazil

[2] CSIRO Mineral Resources, Kensington, WA, Australia

Contents of this file:

Text S1 to S3

Figure S1 to S9

Table 1

Introduction

This document includes additional texts and figures that explain and justify the magnetotelluric data analysis presented in the main paper.

Text S1. Previous geophysical studies in the Parnaíba Basin

As part of the PBAP project, previous studies have employed deep seismic reflection (DSR), wide-angle reflection-refraction (WARR), receiver function (RF), and magnetotelluric (MT) methods to investigate the subsurface structure. These studies were performed approximately along an east-west profile transecting the basin of ~ 1400 km long (Figure S1). The models obtained from these studies are shown in Figure S2. Additionally, Figure S1 displays the location of the existing magnetotelluric studies described in the main paper, conducted on the southeastern edge of the basin and the northern part of the Borborema Province, partially covering the northeastern region of the Parnaíba Basin. The current study presented in this paper runs along the DSR line.

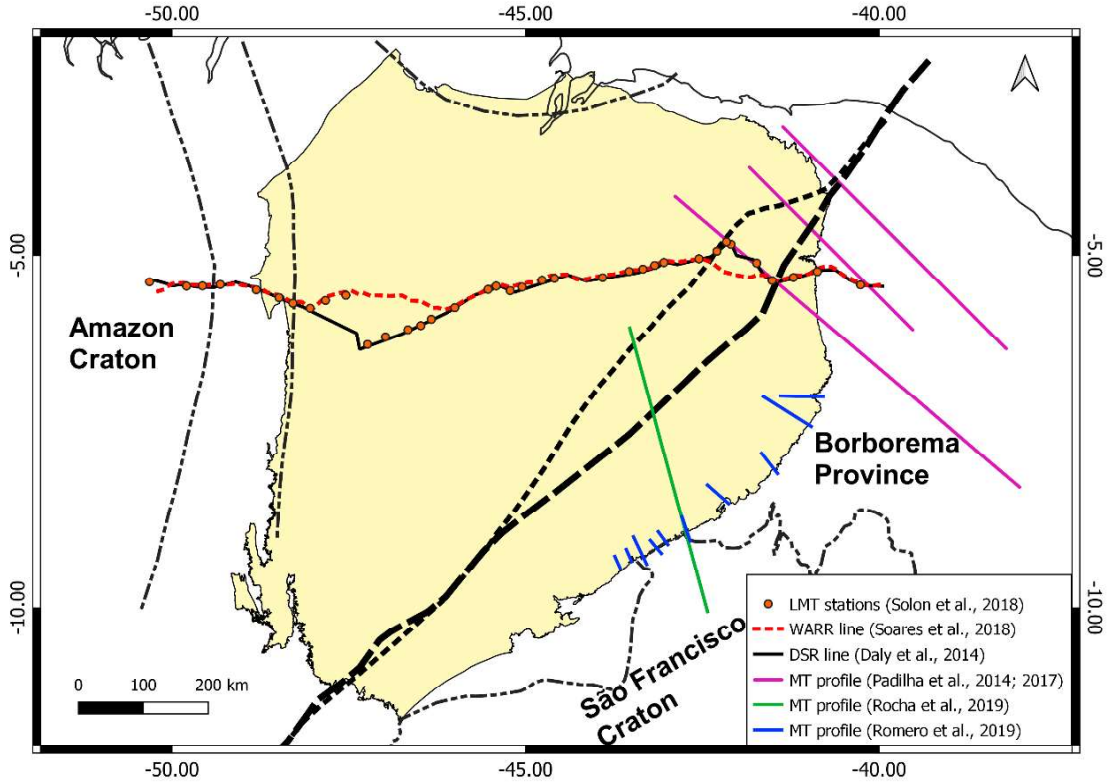


Figure S1. Map of the Parnaíba Basin showing the main tectonic units surrounding it, along with the location of long-period magnetotelluric data (orange circles), the WARR seismic line (red hatched line), and the DSR line (black continuous line). The continuous lines in purple, green, and blue represent the three different magnetotelluric profiles mentioned in the main paper.

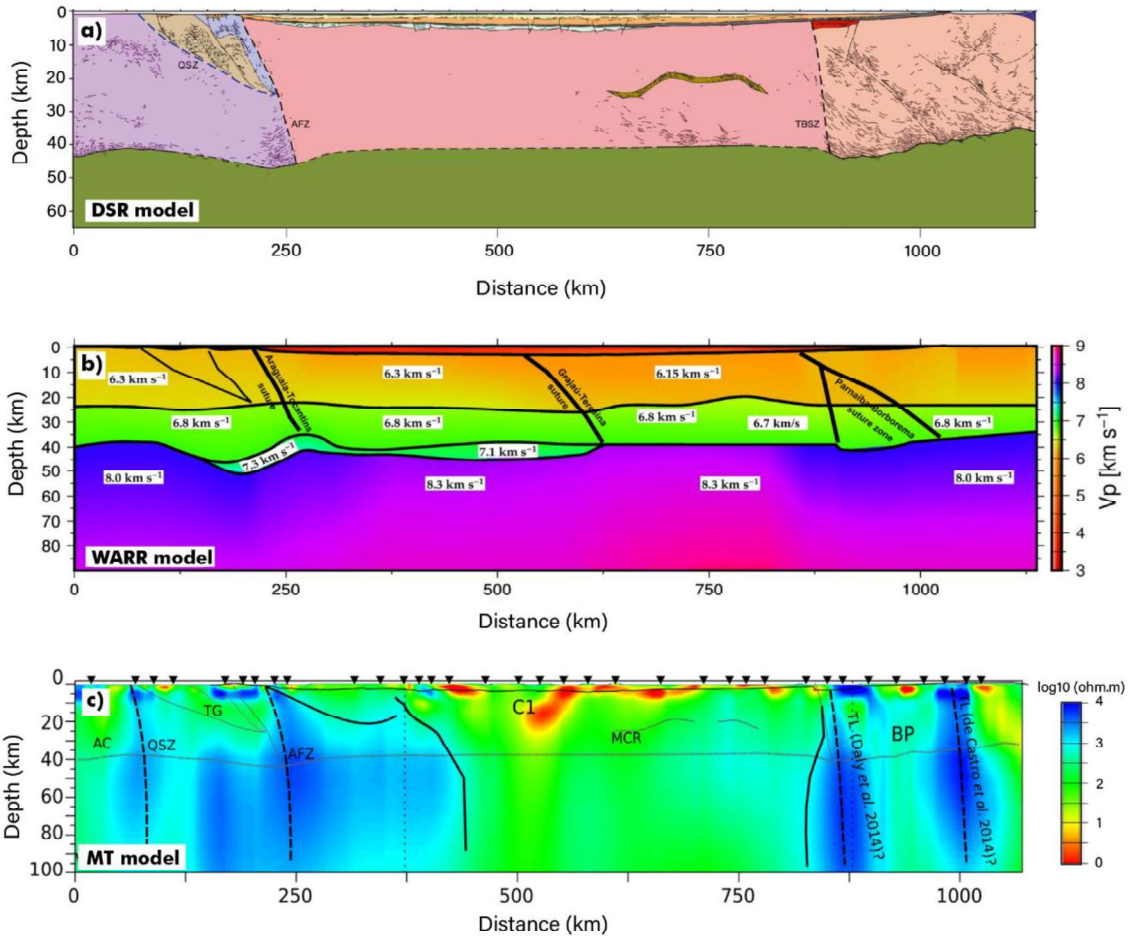


Figure S2. a) Crust and upper mantle configuration of the basin interpreted from seismic data from deep seismic reflection (DSR) profiling (Daly et al., 2014). b) Velocity model of the crust and upper mantle obtained from the wide-angle reflection/refraction data, with P-wave velocities indicated by the colour bar and interpretations from Soares et al., (2018). c) Resistivity model derived from 37 long-period magnetotelluric data by Solon et al., (2018).

Text S2. Depth to Moho map

To construct the Moho depth map shown in Figure 5b of the main paper, seismological data from various previous studies were compiled, incorporating depth estimates derived from seismometers distributed across the entire basin. This dataset is presented in Table 1 and compiled in the paper by Porto et al., (2022). To generate the map, the estimation was performed exclusively using the Moho depth values, excluding errors, through an interpolation process based on the Inverse Distance Weighted (IDW) methodology, implemented in the commercial software QGIS. The distribution of the seismometers is shown in Figure S3.

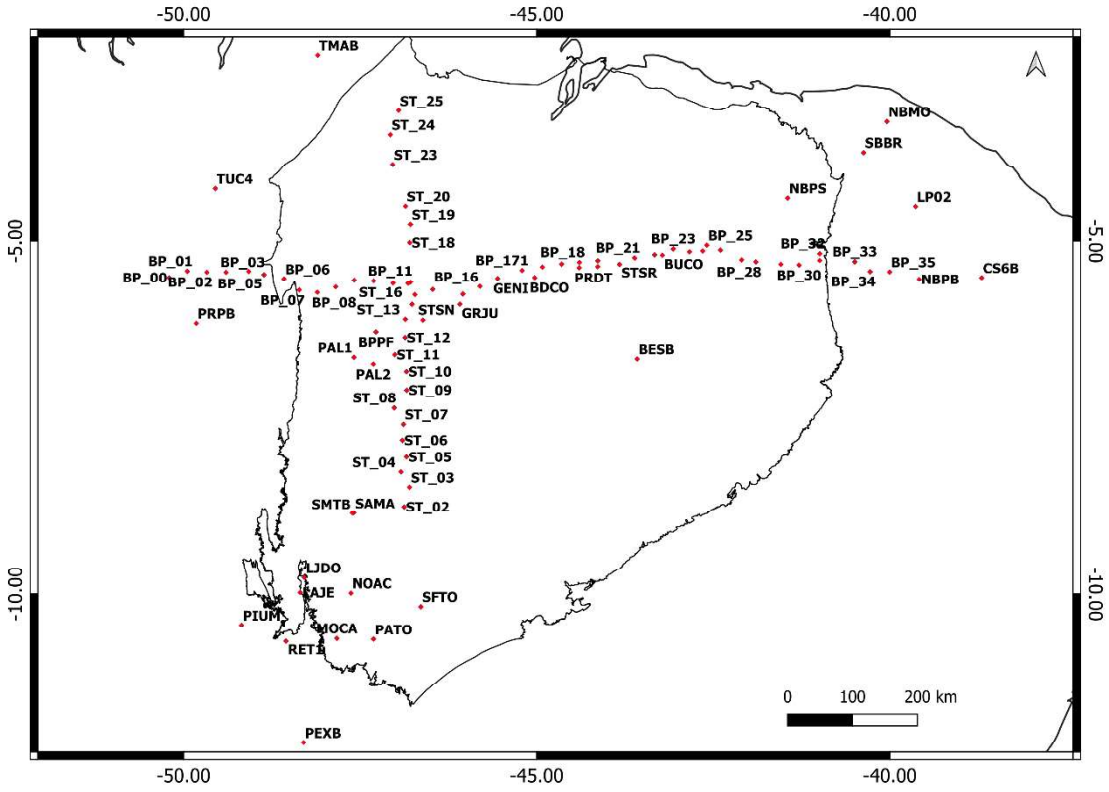


Figure S3. Location map of the seismometers (red diamonds) used to calculate the Moho depth shown in Figure 5b of the main paper. The abbreviations above each station correspond to the names assigned by the respective authors. Refer to Table 1 for more information.

Table 1: Compilation of the location and estimated depth to Moho (H, in km)

Station Name	X (Long)	Y (Lat)	H (km)	Source (Paper references)
PEXB	-48.3006	-12.1056	37,8 ± 1.2	Assumpção et al.,2013
BESB	-43.5774	-6.67307	35.6 ± 1.4	Assumpção et al.,2013
CS6B	-38.6995	-5.51904	30.4 ± 2.5	Assumpção et al.,2013
LJDO	-48.29	-9.77	42.9 ± 0.4	Trindade, 2014
SAMA	-47.59	-8.86	44.1 ± 0.7	Trindade, 2014
NOAC	-47.63	-9.99	44.8 ± 0.9	Trindade, 2014
MOCA	-47.83	-10.63	43.9 ± 0.6	Trindade, 2014
PATO	-47.31	-10.64	44.7 ± 2.7	Trindade, 2014
SFTO	-46.64	-10.18	46.7 ± 14	Trindade, 2014
PIUM	-49.18	-10.44	53 ± 2.3	Trindade, 2014
RET1	-48.55	-10.67	41.3 ± 1.3	Trindade, 2014
NBPS	-41.446	-4.394	39.7 ± 1.1	Luz et al.,2015
NBMO	-40.041	-3.311	34.4 ± 0.3	Luz et al.,2015
NBPB	-39.584	-5.543	36.9 ± 0.6	Luz et al.,2015
SBBR	-40.371	-3.74518	35.5 ± 1.0	Luz et al.,2015
LP02	-39.635	-4.513	30.9 ± 0.6	Luz et al.,2015
TMAB	-48.1	-2.37	38.6 ± 2.8	Albuquerque et al.,2017
PRPB	-49.82	-6.17	37.7 ± 0.4	Albuquerque et al.,2017
TUC4	-49.5499	-4.25792	41.8 ± 2.0	Albuquerque et al.,2017
LAJE	-48.3483	-9.98052	41.7 ± 3.6	Albuquerque et al.,2017
SMTB	-47.6106	-8.86218	36.9 ± 0.4	Albuquerque et al.,2017
PAL1	-47.5868	-6.64928	31.4 ± 2.2	Albuquerque et al.,2017
PAL2	-47.3132	-6.74446	35.4 ± 1.5	Albuquerque et al.,2017
BPPF	-47.2775	-6.29236	45.8 ± 0.2	Coelho et al.,2018
STSN	-46.6113	-6.1258	42.2 ± 0.7	Coelho et al.,2018
GRJU	-46.0878	-5.89975	43.6 ± 0.7	Coelho et al.,2018
GENI	-45.5524	-5.53093	45.1 ± 0.8	Coelho et al.,2018
BDCO	-45.0289	-5.51904	43.7 ± 0.5	Coelho et al.,2018
PRDT	-44.3984	-5.37627	41.1 ± 1.9	Coelho et al.,2018
STSR	-43.8273	-5.32868	40.0 ± 0.4	Coelho et al.,2018
BUCO	-43.2205	-5.19781	39.3 ± 0.5	Coelho et al.,2018

TRZN	-42.6495	-5.13832	40.3 ± 1.1	Coelho et al.,2018
BP_00	-50.20351	-5.51903	37 ± 2.1	Araujo, 2019
BP_01	-49.94781	-5.42512	37.8 ± 3.8	Araujo, 2019
BP_02	-49.67061	-5.44005	38.3 ± 2.1	Araujo, 2019
BP_03	-49.39870	-5.44102	38.1 ± 2.5	Araujo, 2019
BP_04	-49.07796	-5.42786	40.5 ± 3.1	Araujo, 2019
BP_05	-48.86055	-5.47653	49.7 ± 4.6	Araujo, 2019
BP_06	-48.57927	-5.53693	49.5 ± 3.7	Araujo, 2019
BP_07	-48.36077	-5.69813	49.9 ± 2.3	Araujo, 2019
BP_08	-48.10600	-5.73157	44.2 ± 2.5	Araujo, 2019
BP_09	-47.84593	-5.65297	43.4 ± 4.3	Araujo, 2019
BP_10	-47.58424	-5.55614	42.1 ± 2.7	Araujo, 2019
BP_11	-47.30866	-5.56494	41.5 ± 2.8	Araujo, 2019
BP_12	-47.03419	-5.59780	41.2 ± 1.7	Araujo, 2019
BP_13	-46.78689	-5.58506	41.4 ± 4.9	Araujo, 2019
BP_141	-46.47201	-5.68900	41.6 ± 1.1	Araujo, 2019
BP_15	-46.04532	-5.75632	42.7 ± 4.0	Araujo, 2019
BP_16	-45.80336	-5.64585	41.6 ± 2.7	Araujo, 2019
BP_171	-45.20704	-5.41478	42.3 ± 3.6	Araujo, 2019
BP_172	-44.91978	-5.36669	40.7 ± 2.0	Araujo, 2019
BP_173	-44.64743	-5.32479	41.2 ± 3.6	Araujo, 2019
BP_18	-44.39504	-5.29963	38.6 ± 2.0	Araujo, 2019
BP_19	-44.13615	-5.36015	37.4 ± 2.4	Araujo, 2019
BP_20	-44.13615	-5.27665	37.2 ± 3.1	Araujo, 2019
BP_21	-43.61212	-5.23745	37.7 ± 0.2	Araujo, 2019
BP_22	-43.33032	-5.19278	37.7 ± 0.1	Araujo, 2019
BP_23	-43.06687	-5.10947	38.7 ± 1.9	Araujo, 2019
BP_24	-42.83722	-5.15004	38.8 ± 1.7	Araujo, 2019
BP_25	-42.59166	-5.05624	39.2 ± 2.2	Araujo, 2019
BP_26	-42.39786	-5.12597	38.3 ± 1.3	Araujo, 2019
BP_27	-42.09840	-5.26398	40 ± 2.2	Araujo, 2019
BP_28	-41.89689	-5.29237	40.7 ± 0.7	Araujo, 2019
BP_29	-41.54291	-5.32641	38.3 ± 1.9	Araujo, 2019

BP_30	-41.28563	-5.33823	37.4 ± 0.6	Araujo, 2019
BP_31	-40.99248	-5.27260	37.9 ± 0.1	Araujo, 2019
BP_32	-40.99248	-5.17623	37.3 ± 0.4	Araujo, 2019
BP_33	-40.49734	-5.29115	36 ± 0.6	Araujo, 2019
BP_34	-40.27947	-5.43164	35.3 ± 2.3	Araujo, 2019
BP_35	-40.00283	-5.43617	35.4 ± 2.6	Araujo, 2019
ST_02	-46.8764	-8.7728	40.6 ± 3.5	Queiroz, 2019
ST_03	-46.8004	-8.4923	42.4 ± 3.2	Queiroz, 2019
ST_04	-46.9219	-8.2735	41.4 ± 1.1	Queiroz, 2019
ST_05	-46.8428	-8.0603	43.9 ± 0.9	Queiroz, 2019
ST_06	-46.9015	-7.822	40.7 ± 1.7	Queiroz, 2019
ST_07	-46.8863	-7.5988	41.5 ± 0.5	Queiroz, 2019
ST_08	-47.0169	-7.3694	41 ± 2.5	Queiroz, 2019
ST_09	-46.8401	-7.1139	41.9 ± 0.8	Queiroz, 2019
ST_10	-46.8433	-6.8503	43.4 ± 1.7	Queiroz, 2019
ST_11	-47.0096	-6.611	41 ± 1.2	Queiroz, 2019
ST_12	-46.8636	-6.3734	41.7 ± 1.5	Queiroz, 2019
ST_13	-46.8601	-6.1136	39.8 ± 2.3	Queiroz, 2019
ST_14	-46.7658	-5.9016	40.5 ± 2.0	Queiroz, 2019
ST_15	-46.7244	-5.7636	40.6 ± 2.3	Queiroz, 2019
ST_16	-46.8213	-5.6016	43.2 ± 2.2	Queiroz, 2019
ST_18	-46.7975	-5.0212	42.2 ± 2.3	Queiroz, 2019
ST_19	-46.7872	-4.7644	42.3 ± 2.1	Queiroz, 2019
ST_20	-46.857	-4.5081	40.2 ± 5.9	Queiroz, 2019
ST_23	-47.0393	-3.9144	45.3 ± 1.9	Queiroz, 2019
ST_24	-47.0728	-3.4955	45.5 ± 2.8	Queiroz, 2019
ST_25	-46.9542	-3.1543	43.7 ± 4.4	Queiroz, 2019

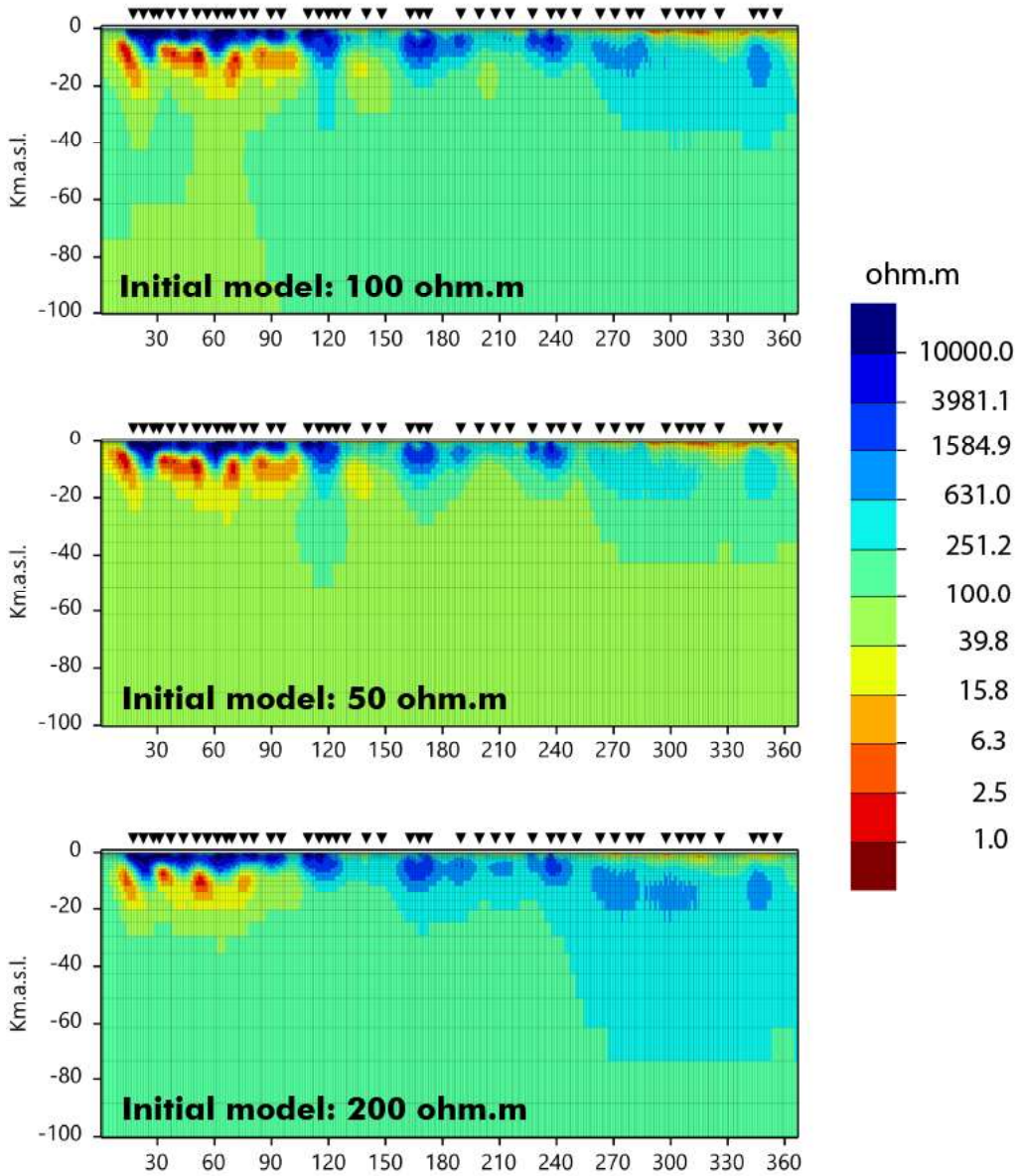


Figure S4. Comparison between the magnetotelluric models obtained for Profile 1 using initial models of 100 ohm.m, 50 ohm.m, and 200 ohm.m.

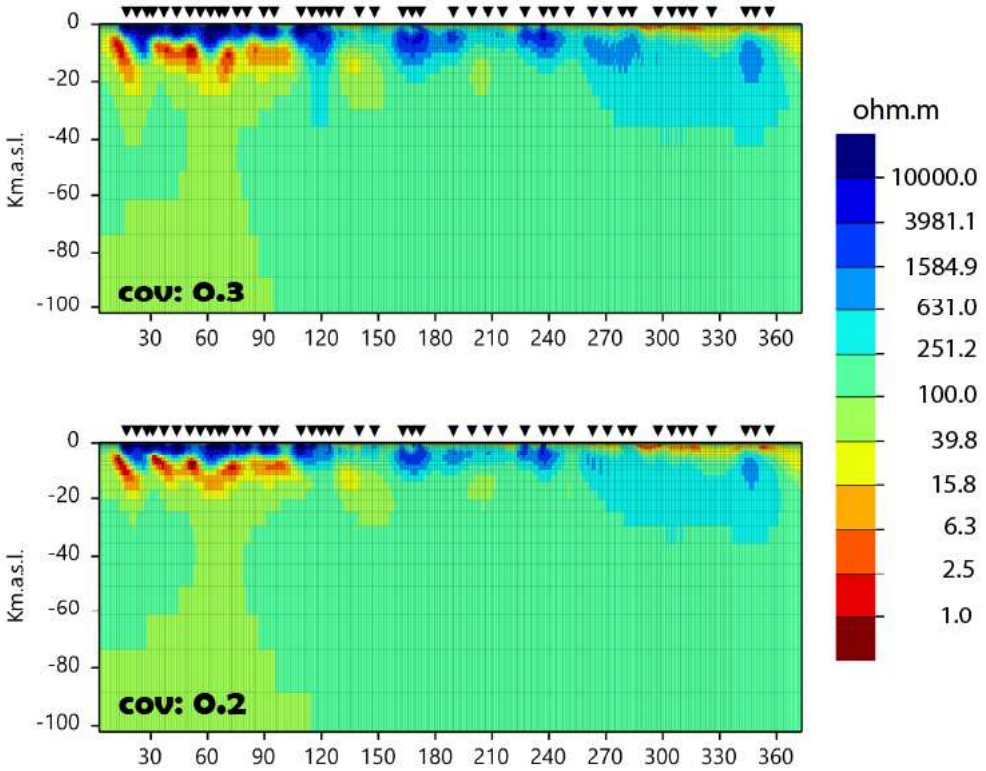


Figure S5. Comparison between the models obtained for Profile 1 with covariance values of 0.3 and 0.2**.**

Text S3. Ocean effect on the MT data

The influence of the ocean on terrestrial magnetotelluric (MT) data has been extensively discussed in the literature (e.g. Fergunson, 2012). This phenomenon caused by the significant resistivity contrast between the electrical resistivities of the sea and land at the coast, resulting in the alteration of geomagnetic fields extending hundreds of kilometers inland. The extent of this influence is primarily determined by the electromagnetic skin depth of the underlying structure affecting the XY and YX polarizations, in distinct ways. In general, the XY characterized by electric fields parallel to the coastline, ρ_{xy} varies smoothly across the coast line. Thus, onshore values of ρ_{xy} are expected to be lower than the electrical conductivity of the continent. Similarly, φ_{xy} values are expected to be higher than 45°. In contrast, the YX polarization characterized by electric fields perpendicular to the coastline, is detect an anomalously high value in electric field. This effect arises from the accumulation of charge at the boundary where there is a contrast in conductivity. This causes ρ_{yx} to increase relative to the electrical resistivity of the continent and φ_{yx} to have values lower than 45°.

We investigated the influence of seawater on MT data along Profile 3, which is closer to the ocean compared to the other two profiles. To achieve this, a forward model was developed using synthetic data distributed along Profile 3. The synthetic model consisted of a homogeneous half-space with a resistivity of 100 ohm.m, incorporating the approximate seawater data, with a resistivity value of 0.3 ohm.m. The initial model used for forward modeling is illustrated in Figure S6. The forward model responses were analyzed for the XY and YX polarizations, with the results shown in Figure S7. As previously discussed, the ocean's influence on MT data manifests as deviations from the responses of a 1D homogeneous model, which would yield apparent resistivities of 100 ohm.m and phase angles of 45° for both XY and YX. For the XY polarization, the ocean's influence is minimal, producing only slight variations in apparent resistivities. In contrast, the YX component, for periods > 100 ohm.m, exhibits more significant variations in apparent resistivity, with more pronounced changes toward the eastern end of the profile at higher frequencies. Additionally, φ_{xy} exhibits values greater than

45°, while φ_{yx} shows lower values. Therefore, based on these results it was decided to include and fix the ocean in each initial inversion model.

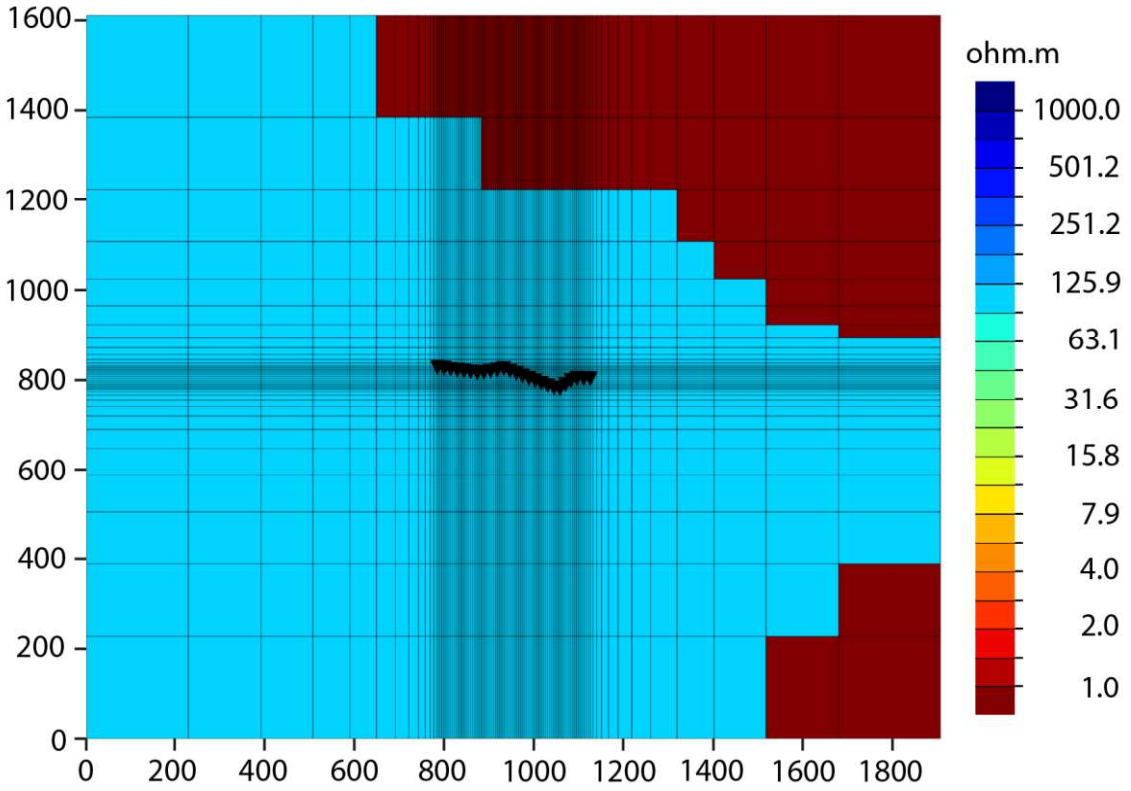


Figure S6. Initial model at zero-meter elevation used to analyse the influence of the ocean on synthetic data along Profile 3. The resistivity value of the ocean (red colour) was set to 0.3 ohm.m.

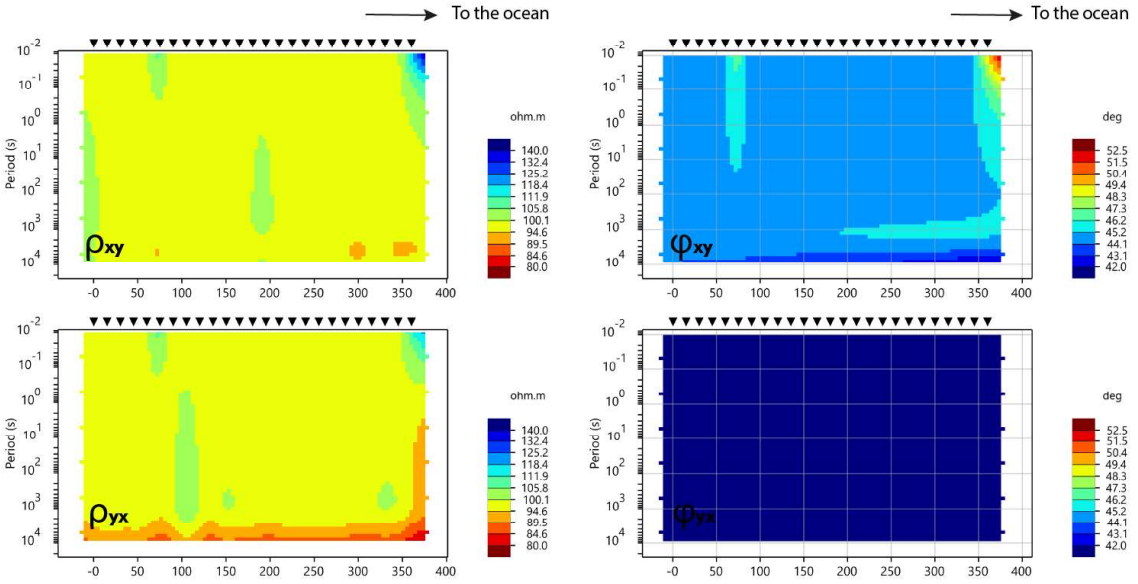


Figure S7. Apparent resistivity (ρ) and phase (φ) responses of the XY and YX polarizations, obtained from the forward modeling of the synthetic model presented in Figure S6, in order to demonstrated the influence of seawater on the magnetotelluric data.

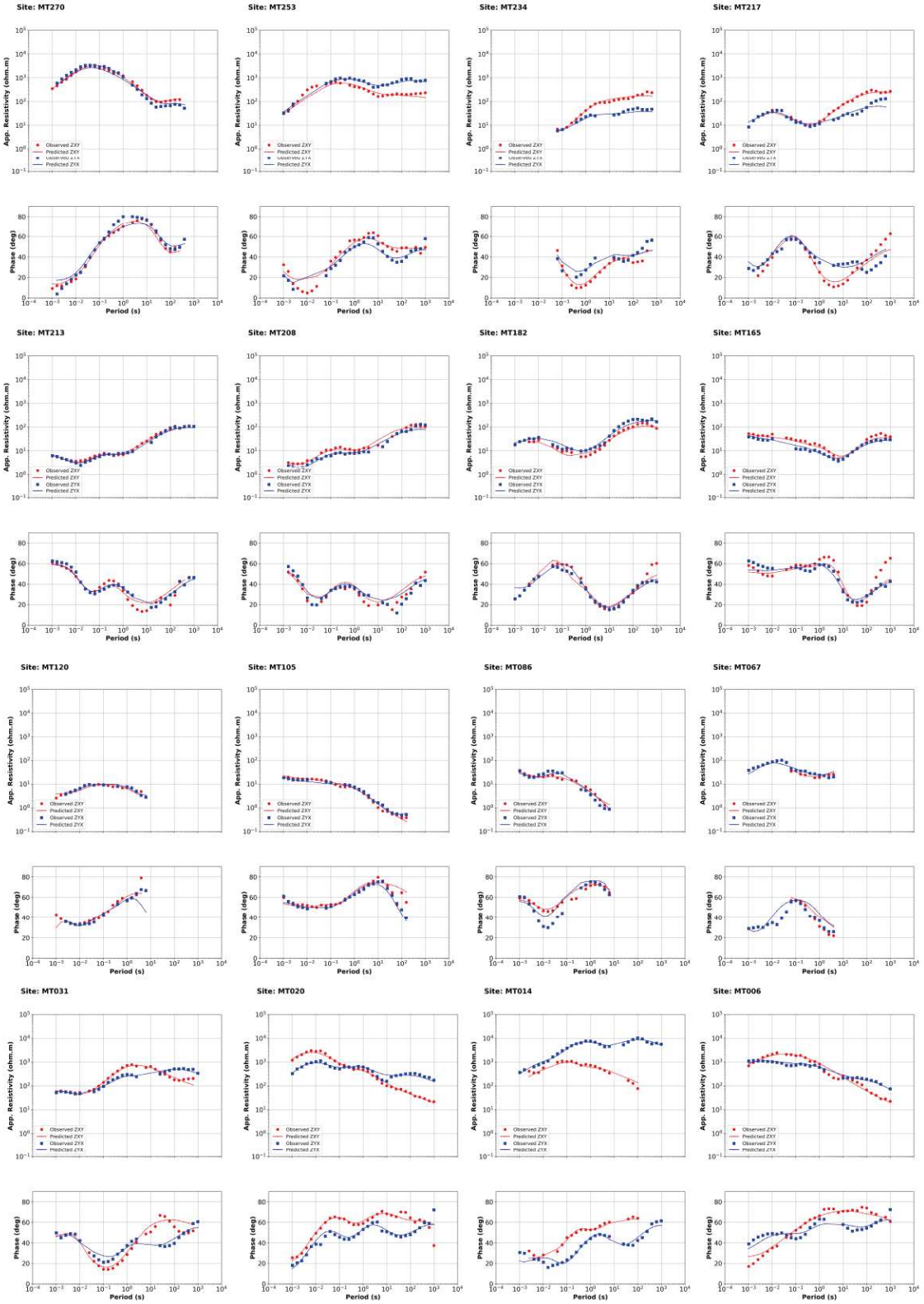


Figure S8. Fit of some representative stations. The data points represent the observed responses for the XY (red) and YX (blue) polarizations, while the solid lines indicate the corresponding predicted curves.

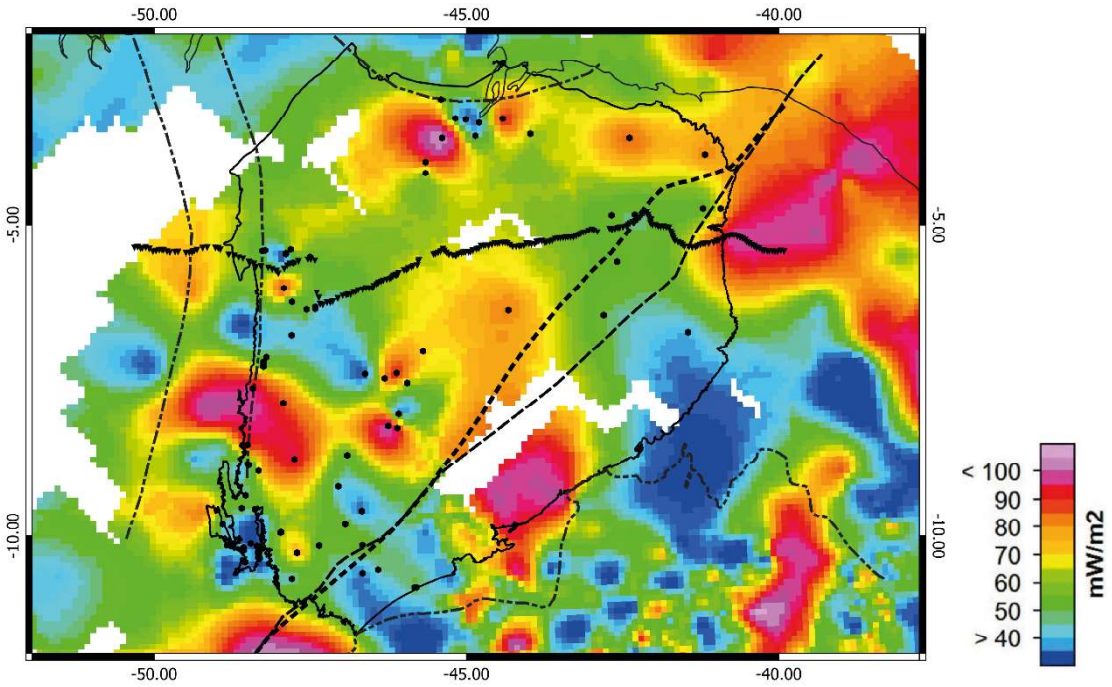


Figure S9. Geothermal map corresponding of the Parnaíba Basin, obtained by Guimarães et al. (2022). The black dots represent well data, which were used to estimate the heat flow.

References:

Albuquerque, D. F., França, G. S., Moreira, L. P., Assumpção, M., Bianchi, M., Barros, L. V., Condori, C., and Oliveira, M. E. (2017). Crustal structure of the Amazonian Craton and adjacent provinces in Brazil. *Journal of South American Earth Sciences*, *79*, 431-442.

Araújo, V.C.M. (2019). Imageamento sísmico da litosfera sob a Bacia do Parnaíba: Estudo de refração profunda e função do receptor com estações de período curto. PhD Thesis. Universidade de Brasilia, Brasilia, Brazil.

Assumpção, M., Bianchi, M., Julià, J., Dias, F. L., França, G. S., Nascimento, R., Drouet, S., Pavão, C.S, Albuquerque, D.F., and Lopes, A. E. (2013). Crustal thickness map of Brazil:

Data compilation and main features. *Journal of South American Earth Sciences*, *43*, 74-85.

Coelho, D. L., Julià, J., Rodríguez-Tribaldos, V., & White, N. (2018). Deep crustal architecture of the Parnaíba basin of NE Brazil from receiver function analysis: implications for basin subsidence. *Geological Society, London, Special Publications*, *472*(1), 83-100.

Ferguson, I. J. (2012). Instrumentation and field procedures. In A. D. Chave and A. G. Jones (Eds.), *The Magnetotelluric Method: Theory and Practice* (pp. 421–479). chapter, Cambridge: Cambridge University Press.

Guimarães, S. N. P., Prado, E. M. G., Vieira, F. P., Lacasse, C. M., da Silva Rocha, N., de Jesus, B. L., and de Souza Filho, O. A. (2022). Updated mapping of terrestrial heat flow in Brazil. *Journal of South American Earth Sciences*, *113*, 103627.

Luz, R. M., Julià, J., and do Nascimento, A. F. (2015). Crustal structure of the eastern Borborema Province, NE Brazil, from the joint inversion of receiver functions and surface wave dispersion: Implications for plateau uplift. *Journal of Geophysical Research: Solid Earth*, *120*(5), 3848-3869.

Queiroz, D.S.D. (2019). Transecta sísmica N-S através do depocentro da Bacia do Parnaíba: Aproximação por função do receptor e CCP. MSc Thesis. Universidade de Brasília, Brasilia, Brazil.

Chapter 5

Structure of the Parnaíba Basin inferred from Bayesian inversion of magnetotelluric data

5.0.1 General Outline

This chapter presents the second publication of this thesis (called here as the "Scientific Paper 2"), entitled as: "structure of the Parnaíba Basin inferred from Bayesian inversion of magnetotelluric data ". This paper was submitted on 5th April 2026 and is currently under review in the journal **Geophysical Journal International**

In this paper, we apply a probabilistic workflow to derive a probabilistic map of the depth to basement of the Parnaiba Basin in Brazil, using magnetotelluric (MT) data along a 1400km long transect. The workflow consists in producing 1D MT Bayesian inversions, that are analysed and further combined with geological a priori information and drill holes data to create a region wide probabilistic map of the depth to basement. This permits to obtain a geologically realistic result while quantifying its uncertainty. The results show a good correlation with existing studies, highlights the value of combining diverse datasets, and showcase the capability of the MT method for this type of application.

5.0.2 Scientific Paper 2

Structure of the Parnaíba Basin inferred from Bayesian inversion of magnetotelluric data.

Gonzalo Romero-Beltran[1], Hoël Seillé[2], Emanuele F. La Terra[1], Liliane P. Panetto[1,3], Gerhard Visser.[2]

[1] National Observatory, Department of Geophysics, Rua Jose Cristino 77, Rio de Janeiro, Brazil

[2] CSIRO Mineral Resources, Kensington, WA, Australia

[3] Federal Rural University of Rio de Janeiro, Department of Petrology and Geotectonics, Seropédica, Rio de Janeiro, Brazil

**Corresponding author (e-mail: gonzalobeltran@on.br)*

Keywords:

Parnaíba Basin; Bayesian inversion; Magnetotellurics; Depth to basement.

Summary

In this study, we apply a probabilistic workflow to image the superficial structure of the Parnaíba Basin, in northeastern Brazil. A dataset composed of 202 magnetotelluric (MT) sites located along a ~1400 km long EW transect profile crossing the basin were inverted, using a trans-dimensional Markov chain Monte Carlo (MCMC) algorithm which considers uncertainties due to non-1D effects present in the data. The resulting 1D model ensembles were analysed and probability distributions on basement depth and a major sedimentary layer were estimated for each MT site. Then, the depth to basement estimations were combined laterally using a Bayesian Estimate fusion algorithm, integrating drillhole and structural data, to construct a probabilistic model of the basement topography. The resulting model indicates that the sedimentary cover reaches depths of ~3 km in the depocenter, with relatively sharp vertical offsets correlated with the Transbrasiliano Lineament and the Araguaia Fault Zone. A conductive domain is also identified in the deep central part of the basin, correlated to

the Poti and Cabeças formations observed downhole, and could be interpreted as the signature of the main hydrocarbon reservoir rocks of the Parnaíba Basin. In the central part of the basin, we tentatively interpret magmatic intrusions and/or post-depositional alteration processes being responsible for the basement geometry. The probabilistic workflow used here represents a powerful complementary tool to traditional deterministic inversion, offering more quantitative and integrated insights to the understanding of the electrical and tectonic architecture of the Parnaíba Basin.

1. Introduction

The Parnaíba Basin is located in northeastern Brazil and represents one of the largest intracratonic basins developed on the South American platform. The deep structure of the basin has recently been the focus of extensive geophysical investigations, based primarily on seismic and potential-field data (Daly *et al.* 2014; Daly *et al.* 2018, Soares *et al.* 2018; Schiffer *et al.* 2021; Tozer *et al.* 2017). This growing interest comes from both its geodynamic and economic relevance, as the basin provides valuable insights into the tectonic processes involved in the assembly of West Gondwana (Porto *et al.* 2022) and accounts for approximately 5% of Brazil's onshore hydrocarbon production (Abelha *et al.* 2018).

The main outcomes of these studies shows that the Parnaíba Basin is composed by three Precambrian tectonic blocks that are limited by Neoproterozoic fold belts: from west to east, these units are the Amazonian Craton, the Parnaíba Block, and the Borborema Province, which underlie the sedimentary sequence filling the basin (Figure 1). The Parnaíba Block is further subdivided into the Teresina and Grajaú domains, which exhibit distinct electrical, seismic and gravimetric properties (Romero-Beltran *et al.* 2025, Soares *et al.* 2018; Porto *et al.* 2022). Most of these studies were part of the PBAP project (Parnaíba Basin Analysis Project), a multidisciplinary effort funded by BP-Brazil to investigate the Parnaíba Basin. Further information about the project can be found in Daly *et al.* (2018).

Recently, as part of the PBAP project, Romero-Beltran *et al.* (2025) characterized the geo-electric structure of the basin at crustal and upper mantle scale using a 3D deterministic inversion process of magnetotelluric (MT) data. Their resistivity models revealed the different resistivity/conductivity anomalies associated with the coupling mechanisms among the units that led to the formation of the basin and their implications on the West Gondwana formation. However, at basin scale, in the first 3/4 kilometers, the sedimentary sequence down to the underlying basement was only coarsely imaged. This model presented limitations in imaging accurately shallow structures such as the depth to basement because of the mesh used for the inversion. The computational cost of a 3D inversion is directly related to the amount of model parameters, or cells. The scope of the study by Romero-Beltran *et al.* (2025) being to image the complete crust, relatively large cells were used, which cannot account for small-scale lateral and vertical variations occurring in the basin. Moreover, the smoothness constraints applied to the inversion do not allow for the recovery of sharp resistivity contrasts, which are expected at the sediment/basement interface.

Another limitation of a 3D deterministic inversion is the characterization of the uncertainty in the final model. In a probabilistic framework, the solution to an inverse problem consists in a full probability distribution over the whole model parameter space (Tarantola 2005). Compared to a deterministic inversion, which provides as a solution a single best model, the solution is therefore an ensemble of models, from which uncertainty can be derived. However, exploring the model space is computationally very expensive, requiring hundreds of thousands to millions of forward simulations. Lately, probabilistic approaches have been increasingly applied to MT inversion problems, particularly in 1D studies (e.g. Conway *et al.* 2018; Xiang *et al.* 2021; Seillé & Visser, 2020; Ardid *et al.* 2021) and, to a lesser extent, to 2D and 3D investigations (Chen *et al.* 2012; Rosas-Carbajal *et al.* 2015, Manassero *et al.* 2020). Even though large-scale probabilistic inversions can now be used in geophysical studies thanks to the increasing amount of computing resources (e.g., Henneking *et al.* 2025) or new sampling approaches are being developed to explore the model space more efficiently (e.g., Magrini & Sambridge, 2025), a full 3D probabilistic MT inversion currently remains impractical. In this study, we use probabilistic inversion of MT data, using a 1D sampler. While the Earth is

inherently 3D, properly accounting for dimensionality effects in the data using an error model has proven to be valuable to image sedimentary basins accurately (Seillé *et al.* 2021).

In this study we apply the workflow presented by Seillé *et al.* (2021), to derive a depth to basement probability map. The workflow consists in 3 successive steps: 1) computing 1D probabilistic inversions for each MT station independently, 2) analyze posterior model ensembles, in particular resistivity layer interface distributions or change points, to derive interface depth probabilities at each MT location and 3) use a Bayesian Estimate Fusion algorithm to combine laterally these estimates, using drillhole information and geological faults information. Following this workflow, our objective is to derive a probabilistic map of the depth to basement and extracting information regarding the nature and location of sedimentary layers along the profile.

The MT data analysed used in this study consists of 202 stations reported in Romero-Beltran *et al.* (2025), along an EW transect profile across the Parnaíba Basin, spanning more than 1400 km. Figure 1 shows the distribution of the MT soundings employed in this study over the simplified geological map and main structural features identified from seismic and potential field data (Daly *et al.* 2014; De Castro *et al.* 2014). Note that the Transbrasiliano Lineament has two distinct interpretations. The first, proposed by Daly *et al.* (2014), interprets it as a shear zone located at the boundary between the Amazonian Craton and the Parnaíba Block, whereas the second, identified by De Castro *et al.* (2014), places it approximately 100 km to the east. Both interpretations are considered and discussed throughout this study.

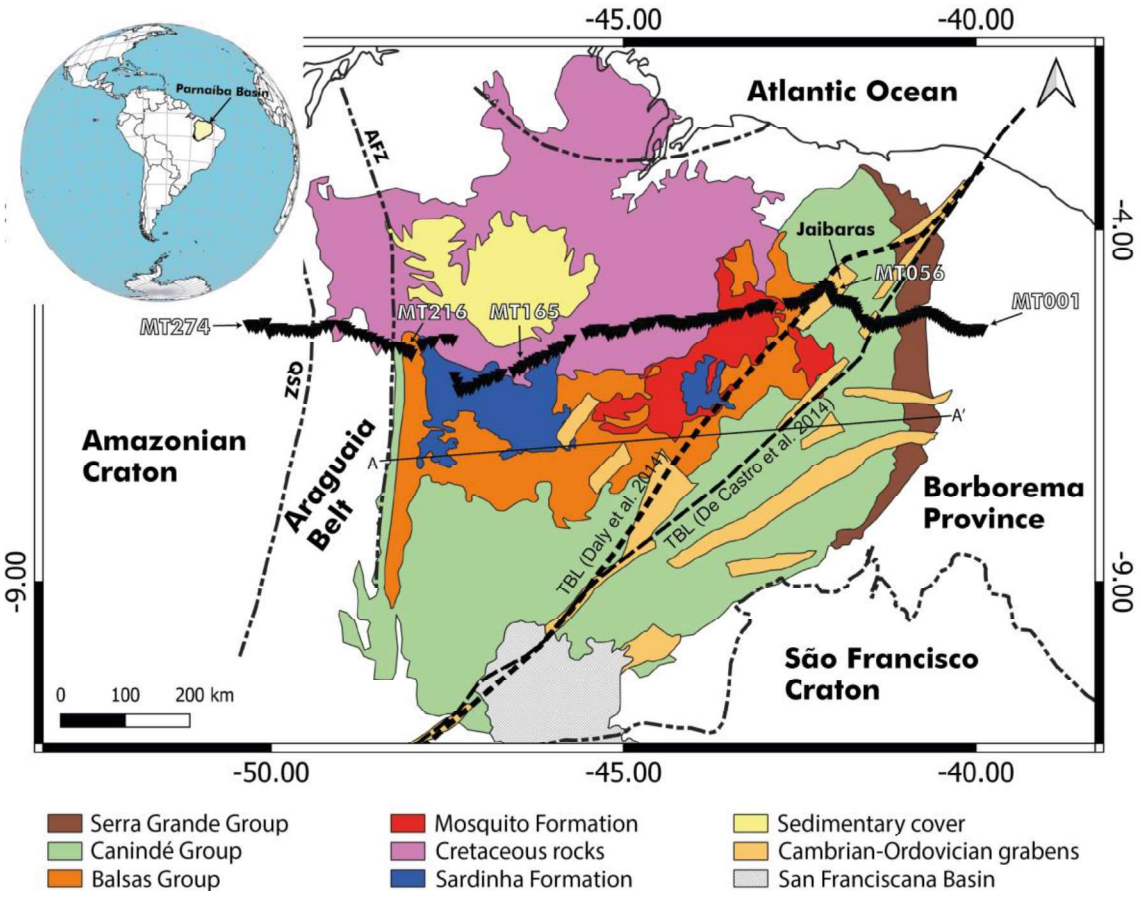


Figure 1. Simplified geological map of the Parnaíba Basin, adapted from De Castro *et al.* (2014). Black triangles indicate the locations of magnetotelluric stations, with five representative stations labeled and discussed in the text. Major sutures and lineaments: QSZ – Quatipuru Suture Zone, AFZ – Araguaia Fault Zone, TBL – Transbrasiliano Lineament. Profile A–A' corresponds to the geological cross-section shown in Figure 2. The inset map shows the location of the Parnaíba Basin in South America.

2. Geological settings

The Paleozoic Parnaiba Basin covers a large area of approximately 600,000 km^2 (Vaz *et al.* 2007). The basin is a circular sag basin with a sedimentary column of approximately 3,500 m thickness in the depocenter (Vaz *et al.* 2007). The successions were deposited from the Silurian to the Cretaceous, whereas the crystallin basement underlying the basin is composed of Precambrian rocks from Araguaia Belt and Borborema Province (Milani & Zalán, 1999).

We identified at least two rift stages overprint on the Parnaíba Basin structural framework. The oldest one is apparently represented by asset of extensive graben -like non-outcropping structures restricted mostly to the basement inliers. The second rifting stage is recorded by a set of Cambrian–Ordovician grabens, which partially outcrop along the basin margins and extend beneath the sedimentary sequence. The distribution of the grabens is concentrated along the Transbrasiliano Lineament and toward the southeastern sector of the basin (Figure 1). Among these structures, the Jaibaras rift represents a precursory stage that was slightly inverted before the initiation of sag deposition in the intracratonic basin (Oliveira & Mohriak, 2003).

The stratigraphic record of the Parnaiba Basin (Figure S1 in the Material Supplementary) encompasses three major Paleozoic and two Mesozoic super sequences (Góes & Feijo, 1994). The basal one, mainly of Silurian age, is represented by rocks of the Serra Grande Group. These strata, up to 900 m thick, consist mainly of conglomerates, pebbly sandstones, diamictites, and limestones (Caputo & Dos Santos, 2020). The second one is the Canindé group, associated with intense seafloor spreading in the evolutionary context of the Gondwana paleocontinent demonstrate that climatic events caused a global trend of rising sea level in the Devonian period (Oliveira & Moura, 2019). The Canindé Group of the Parnaíba basin records one of the most important marine incursions in the South American platform (Góes *et al.* 1990; Vaz *et al.* 2007), where the petroleum system is associated. The Pimenteiras Formation is included as part of this group, which is the main source of the hydrocarbons resources, mainly composed of dark radioactive shales rich in organic matter (Mussa *et al.* 2021) and, which are widely distributed and reach thicknesses greater than 500 m (Góes *et al.* 1990). The third sedimentary sequence is the Balsas Group (Neocarbonifere-Eotriasic). This sequence represents a succession of rocks deposited in a complex shallow-sea clastic/evaporitic environment, gradating to a continental environment dominated by lacustrine and desert systems (Vaz *et al.* 2007).

Two main magmatic events have been identified in the Parnaíba Province, both associated with the rifting processes that led to the breakup of the South American and African continents (Thomaz Filho *et al.* 2000, 2008). These events reflect distinct

episodes of basic to intermediate magmatism that culminated in the fragmentation of the supercontinent Gondwana. The first event corresponds to early Jurassic tholeiitic basic magmatism, represented by the Mosquito Formation, composed mainly of lava flows and, more locally, sills and dikes, linked to the opening of the Central Atlantic. The second magmatic event is the Sardinha Formation, related to the rifting of the South Atlantic (Almeida, 1986; Milani & Thomaz Filho, 2000). This geological unit occurs predominantly as diabase dikes and sills. A simplified geological cross-section of the basin (adapted from Góes *et al.* 1990) is shown in Figure 2, where the main geological units that compose the basin are identified.

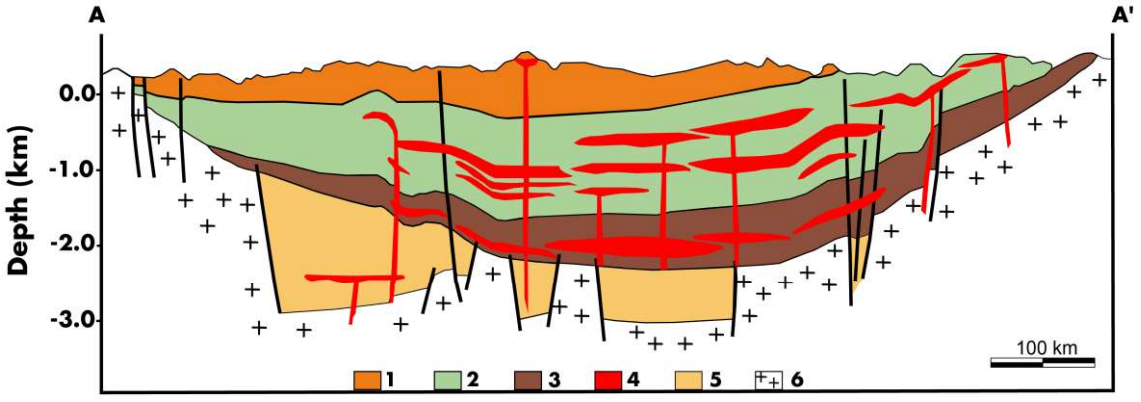


Figure 2. Geological vertical section along profile A–A' shown in Figure 1. Adapted from Góes *et al.* (1990). Legend description: 1-Balsas Group; 2-Canindé Group; 3-Serra Grande Group; 4-Magmatic intrusion; 5 Pre-Silurian rift and 6-Basement.

3. Magnetotelluric data

The MT dataset consists in 202 stations spaced approximately 5 km along a 1400km EW transect across the Parnaiba Basin. The MT method is a passive electromagnetic geophysical technique used to characterize the subsurface electrical resistivity structure (Simpson & Bahr, 2005; Chave & Jones, 2012). This method relies on the principle of electromagnetic induction, where the temporal fluctuations in the Earth's external magnetic field with the electrically conductive rocks induce electrical and magnetic

fields. In the MT measurements, magnetic and electric fields are measured at the surface in the orthogonal directions, x and y. Commonly x , y represent the North-South and East-West orientation, respectively. The MT data processing consists in estimating the magnetotelluric transfer function, called of the Impedance Tensor, Z, which relates electric field (E_x , E_y) and the magnetic field (H_x , H_y) in the frequency domain. This is a $2\ x\ 2$ complex impedance tensor:

$$\begin{pmatrix} E_x \\ E_y \end{pmatrix} = \begin{pmatrix} Z_{xx} & Z_{xy} \\ Z_{yx} & Z_{yy} \end{pmatrix} \begin{pmatrix} H_x \\ H_y \end{pmatrix} \quad (1)$$

Usually, the complex impedance tensor can be interpreted through its magnitude (apparent resistivity) and phase parameters component wise ($ij\ = xx, xy, yx, yy$):

$$\rho_a(\omega)\ = \frac{1}{\mu_0 \omega} \left| Z_{ij}(\omega) \right|^2$$

$$\phi_{ij}(\omega)\ = tan^{-1}\ \frac{Im\ Z_{ij}(\omega)}{Re\ Z_{ij}(\omega)} \quad (2)$$

The apparent resistivity denoted by ρ_a (Ωm) represents the average resistivity in a volume of subsurface at a particular frequency, and the impedance phase ϕ in degrees describes the phase difference between the electric and magnetic field (Simpson & Barh, 2005). Most inversions (including the one used in this study) use the impedance tensor, but the data is displayed as apparent resistivity and phases for interpretation convenience.

MT can resolve structures from tens of meters to several hundred kilometers beneath the Earth's surface (Simpson & Bahr, 2005) and is well suited for imaging sedimentary basins (*et al.* e.g. Vozoff, 1972; Hautot *et al.* 2006; Cai & Zhdanov, 2016) due to the strong resistivity contrast between a conductive sedimentary basin and a resistive basement. In particular, the electrical resistivity of sediments is controlled by factors such as water content, grain size, relative density, and geochemical properties (e.g., Selway, 2014; Levesque *et al.* 2023). Because sediment resistivities span a broad range (see Figure S2 of the Material Supplementary), no unique resistivity value can be

assigned to a specific lithology; instead, bulk conductivity is primarily governed by fluid conductivity, porosity, saturation, and pore connectivity (Glover, 2015).

The MT transfer functions were calculated using the standard robust estimation technique of Egbert (1997). Further details about the processing strategy applied are found in Romero-Beltran *et al.* (2025). The data quality in the central part of the basin, where a higher level of anthropic EM noise is present, is characterized by usable periods that on average are limited to 100 s and by low signal to noise ratio. In contrast, stations located at the ends of the profile generally achieved better data quality, with periods extending up to 1000 s.

3.1. Pseudosections

Pseudosections of the observed apparent resistivity data and phase data are plotted as a function of frequency. Although the relationship between frequency and depth is inherently nonlinear, these plots provide a preliminary view of the subsurface geo-electric structure. They are particularly useful for identifying large-scale resistivity contrasts and inferring major structural features. Figure 3 shows the apparent resistivity and phase pseudosections for the XY and YX polarisations of the MT data projected along an EW profile.

The apparent resistivity plots reveal a typical sedimentary basin architecture, characterized by conductive sedimentary units overlying a resistive crystalline basement, with sediment thickness increasing toward the central depocenter of the basin where it reaches its maximum. This observation aligns well with the geological cross-section presented in Figure 2. In the central portion of the basin, at periods > 10 seconds, both polarizations reveal the presence of highly conductive features (< 10 Ωm), whose interpretation will be discussed later.

On the other hand, the phase response exhibits an inverse relationship with apparent resistivity; that is, an increase in phase generally indicates a decrease in resistivity, and

vice versa. Although absolute apparent resistivity values cannot be directly inferred from the phase alone, this parameter effectively reflects the underlying geoelectric structure and lateral variations. Note, in the central portion of the basin, the phases of both polarizations show a similar behavior, with values ranging between 27° and 72°, delineating an oval-shaped region characterized by higher phase values. This behavior typically indicates that the geological medium exhibits a predominantly stratified structure (1D). Beyond this high-phases transition, the phase values begin to decrease, indicating a corresponding increase in resistivity, which is consistent with the features observed in the apparent resistivity. Overall, the pseudosections permit to observe that the processed data displays the shape of the basin, and the succession of conductive/resistive layers.

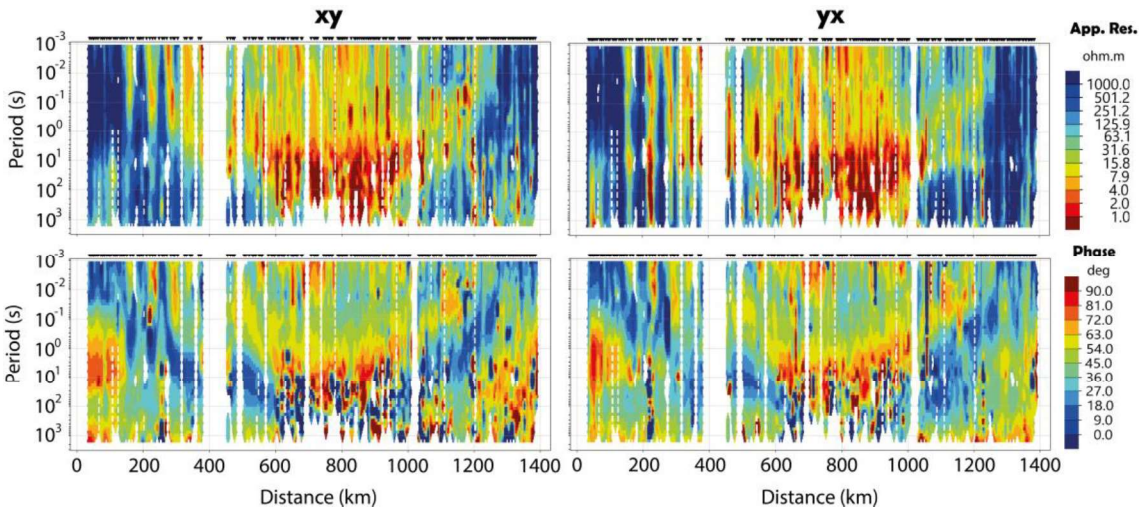


Figure 3. Apparent resistivity and phases pseudosections of the XY and YX polarizations. On top, the inverted black triangles represent the MT stations.

3.2. Dimensionality analysis

One of the most widely used approaches for evaluating the dimensionality of MT data is phase tensor analysis (Caldwell *et al.* 2004). Mathematically, the phase tensor is defined as $\varphi = X^{-1}Y$, where X and Y are the real and imaginary parts, respectively, of the complex impedance tensor, Z. A key advantage of this method is that it is free to galvanic distortion and does not require any assumptions about the underlying

resistivity structure of the subsurface (Caldwell *et al.* 2004). The phase tensor skew angle β, introduced by Caldwell *et al.* (2004), can be used to assess data dimensionality as a function of frequency. It was proposed that values of $|\beta| > 3°$ indicate a three-dimensional (3D) behavior, whereas $|\beta| < 3°$ suggests a predominantly one two-dimensional (1D or 2D) structure. To further support dimensionality assessment, Bibby *et al.* (2005) introduced an additional parameter, the phase tensor ellipticity λ. Values of λ < 0.1, causing phase tensor ellipses to be quasi-circular, are indicative of a 1D behaviour.

Romero-Beltran *et al.* (2025) performed a dimensionality analysis of the MT dataset using phase tensor ellipses, colored by the skew angle, along the entire profile (Figure 4.) The results revealed a predominantly 1D regime at low period associated with the thick sedimentary sequence, and a more complex 3D domain at longer periods, associated to the crystalline basement.

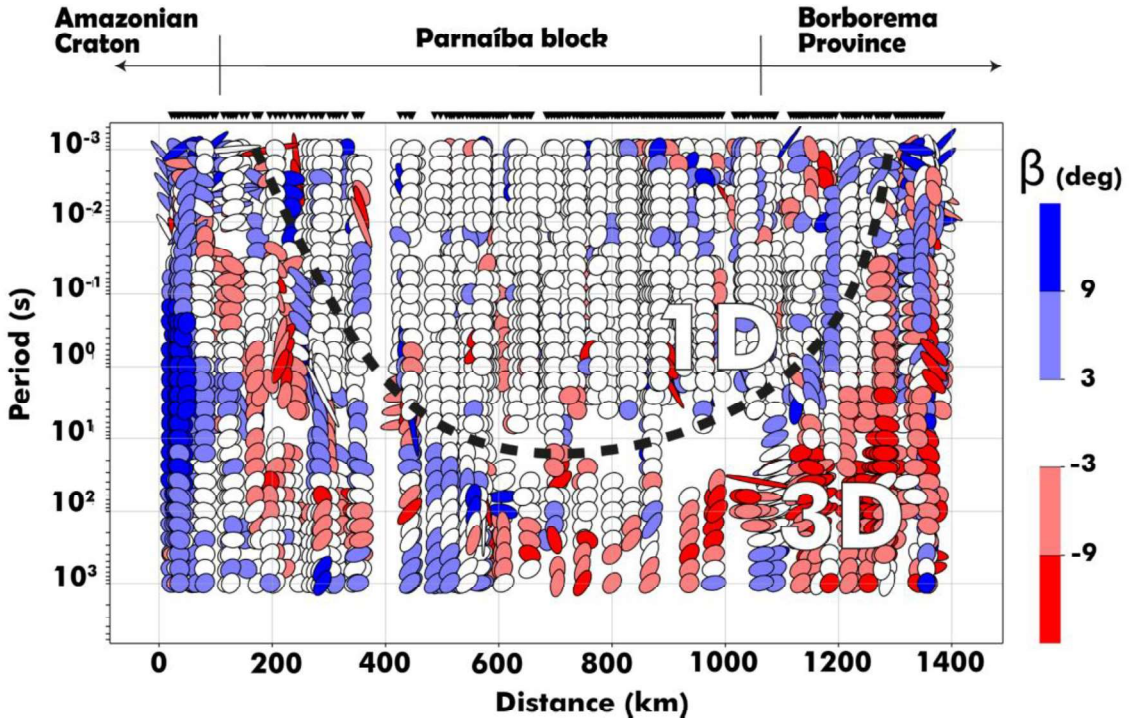


Figure 4. Phase tensor analysis (adapted from Romero-Beltran *et al.* 2025). The ellipses are color-coded according to the *skew* value. The dashed black lines broadly delineate the. predominantly one-dimensional (1D) behavior observed in the data, whereas the underlying domain exhibits a clear transition toward a 3D response.

In this study we are interested in mapping the basin down to the basement. We can therefore expect the 1D assumption that is taken by our algorithm will hold for that purpose. As it will be described in the next section, even if 2D/3D effect are observable, the method we will employ will take it into account using higher errors. Therefore, masking non 1D data is not required for the purpose of this application.

4. Bayesian MT data inversion

4.1. Theory

Within a probabilistic (or Bayesian) inversion framework, both the data (d) and the model parameters (m) are treated as random variables represented by associated probability distributions. The Bayes theorem states that the posterior probability distribution function $p(d|m)$ on the model parameters (m) given the data (d) is given by:

$$p(m|d) = \frac{p(d|m)p(m)}{p(d)} \quad (3)$$

where $p(d|m)$ is the likelihood function, $p(m)$ is the prior model defined on the model parameters m. Considering that $p(d)$ is independent of m, equation 3 can be written as:

$$p(m|d)\ \alpha\ p(d|m)\ p(m) \quad (4)$$

The likelihood function assesses the model's ability to explain the data, with higher likelihood associated with model predictions $f(m)$ that closely match the observed data d. The likelihood function $p(d|m)$ is defined as:

$$p(d|m)\ \alpha\ \exp(-\frac{1}{2}\left(d_{obs} - g(m)\right)^T C_d^{-1}(d_{obs} - g(m))) \quad (5)$$

where d_{obs} denotes the observed data, $g(m)$ is the MT forward operator for model parameters m and C_d^{-1} is the inverse of the data covariance matrix. Inverting the data using a 1D modelling assumption can introduce bias in the results when the assumption is not met. Recently, Seillé & Visser (2020) propose a new method to quantitatively

correct the bias resulting from the 1D Earth assumption. They developed an error model that uses the phase tensor data. When the phase tensor skew angle β and ellipticity λ indicate 2D or 3D effects, the error model will estimate the error required to compensate the error due to the 1-D physics assumption, using a regression tree (Table S1 of the Supplementary Material). We use that method here, having the data covariance matrix C_d as a diagonal matrix defined as: $C_d = C_p + C_{dim}$, with C_p the processing error covariance matrix, and C_{dim} is the dimensionality covariance matrix produced by the decision tree as a function of the dimensionality parameters β and λ. At long periods, C_{dim} is generally greater than C_p, while at high frequencies the processing error C_p can dominate when the data is quite 1D.

For the inversion, we use the 1D trans-dimensional Markov chain Monte Carlo sampler developed by Seillé & Visser (2020), in which the models can have variable number of dimensions, that is, 1D models with varying number of layers.

4.2. Inversion strategy

In 1D inversion processes, whether deterministic or probabilistic, it is common practice to use the determinant of the impedance tensor ($Z_{det} = \sqrt{Z_{xx}Z_{yy} - Z_{xy}Z_{yx}}$), as it is rotation-invariant and contains information from all four tensor components. This property makes it particularly valuable in scenarios where 3D effects are present, even when applying 1D or 2D inversion schemes (Berdichevsky *et al.* 1980; Pedersen & Engels, 2005). However, as indicated in Section 3, the MT data from the Parnaíba Basin exhibit a low signal-to-noise ratio at certain stations located in the central part of the profile. In our case, the noise generally affects one of the two polarizations and could therefore be associated with cultural noise sources that generate an electromagnetic signal that is linearly polarized in a certain direction (Szarka, 1988; Junge, 1996). We therefore applied the following strategy: when both polarizations presented good data, the determinant was used, in other cases, the best polarization was used. In Figure S3 of the Supplementary Material the data that was selected for each station is presented. The determinant is the main data used for the

inversion, whereas the YX polarization is predominantly used at stations located in the eastern sector of the profile. In contrast, the XY polarization is used less frequently than the other two parameters and is mainly concentrated in the central part of the basin. In the case where only one polarization was used, the dimensionality error derived using the method of Seillé & Visser (2020) couldn't be used, because the phase tensor parameters β and λ require the full impedance tensor Z to be calculated. In those cases, we used the errors estimated at the closest station that was using determinant data, considering an error floor of 3%.

Figure 5 presents the apparent resistivity and phase curves for three representative stations along the profile, for which the determinant of Z is used. The error bars for each frequency correspond to the data uncertainty, derived from the diagonal elements of the data covariance matrix C_d. This estimation accounts for the non-1D nature of the data, incorporating variations in geometric dimensionality as indicated by the phase tensor skew angle, β and ellipticity, λ. An example of stations located near the three representative stations that employ XY or YX polarization is shown in Figure S4 of the Supplementary Material. Station MT058, located in the eastern sector of the profile (Borborema Province), exhibits a higher level of error from periods of about 3 s onwards, reflecting the increase in 2D and 3D effects, as indicated by the β and λ phase tensor parameters. A similar behaviour is observed at station MT220, located at the western end of the profile (Amazonian Craton), with non-1D effects starting at lower period, around 1s. Station MT165, situated in the central part of the basin (Parnaíba Block), shows a relatively 1D behaviour up to 10s, with the determinant having therefore assigned low errors.

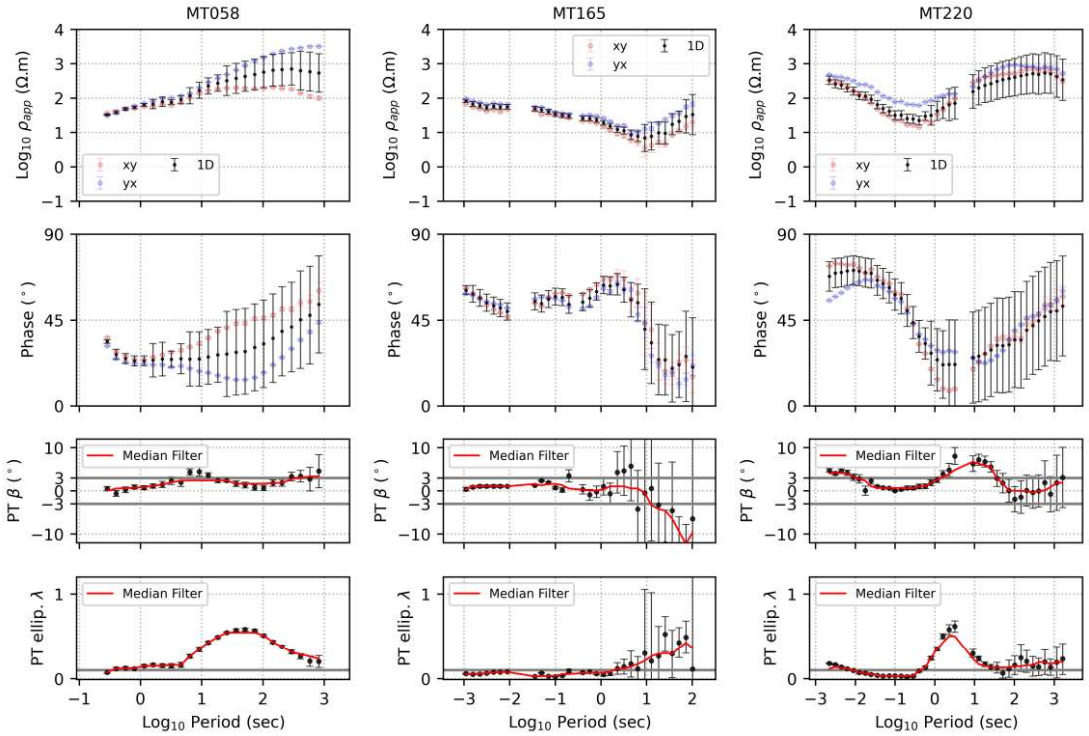


Figure 5. Apparent resistivity and phase curves for three representative soundings along the profile using the determinant of Z. The error bars associated with each frequency are estimated from the dimensionality analysis presented in the lower panels, based on the parameters β and λ.

4.3. Inversion results

4.3.1. Posterior probability density distributions

Each MT sounding was inverted using the probabilistic inversion described in section 4.1. The prior distribution over the resistivity was defined as uniform, spanning a broad range from 10^{-2} to 10^{6} Ωm. For the number of interfaces, a depth-dependent prior was employed, with an expected total of 10 interfaces (i.e., 11 layers) down to 100 km depth, distributed across four depth intervals. A higher layer density was assigned within the 5 to 5,000 m depth range to better capture structural complexity in the shallow subsurface.

For each MT station independently, the inversion was performed using 40 Markov chains, each with 10^6 simulations, ensuring convergence across all chains. The first 75% of each chain was discarded as the burn-in period, to let the chains reach a stationary distribution. This step ensures that only well-converged sample-representatives of the posterior probability distribution were retained for the final statistical analysis and model estimation. An example of the convergence for three representative stations is shown in Figure S5 of the Supplementary Material. From each chain, 100 models were saved. In total, the posterior distribution of model parameters is approximated by 4,000 models for each MT site.

Figure 6a presents the posterior probability distributions for three representative MT stations. The statistics of the posterior, the 50^{th} (median), the 5^{th} and the 95^{th} percentiles are also plotted. The 5^{th} and 95^{th} are used to assess the uncertainty associated with the resistivity values. The 95^{th} percentile illustrates the most resistive models that fit the data, while the 5^{th} percentile highlights the most conductive models. The change-point probability distributions are also plotted, which describes the interface probability as a function of depth. These models show the succession of layers of different resistivity, likely corresponding to distinct geological units of the Parnaíba Basin. For these three models we numbered from 1 to 3 the main observed transitions. Interface 1 observed around 400/500m depth is common for all three models. Interface 3 is common to the 3 models and shows a transition from a conductive to a resistive domain, likely associated to the contact between the sedimentary sequence and the underlying crystalline basement. It appears at different depths, shallower on the edges of the eastern and western ends of the basin (~800 m depth for station MT056 and ~1800m depth for station MT219 respectively), and deeper in the central part of the basin (~2500m for station MT165). For the site MT165 where the sedimentary cover appears to be the more important, another layer is observed, defined by interface 2. This interface associated to a conductive layer is not present in the other two models and is only visible in the central part of the basin, for depth greater than 1000m.

In Figure 6b, the response posterior distributions for apparent resistivity and phase for the three models are shown. A good data fit is achieved at all frequencies. An RMS distribution centred on 1 is achieved for most MT stations.

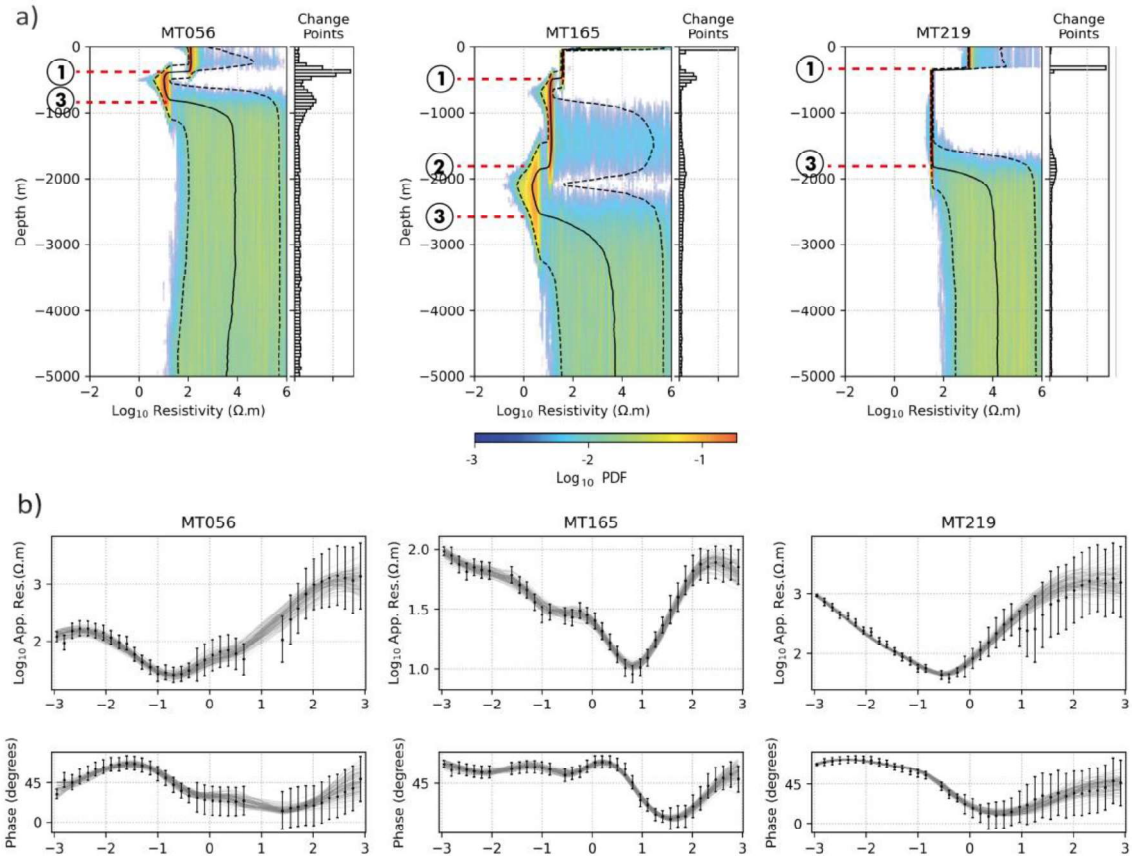


Figure 6. a) Posterior probability density distributions for three MT stations and the corresponding change points distribution. In the posterior density distribution, the solid black line represents the median model, and the black dashed lines the 5th and 95th percentiles defining the uncertainty. The bullet points 1, 2, and 3 correspond to the main resistivity transitions identified in these models. The first two represent transitions within the sedimentary package, whereas transition 3 corresponds to the sediment–basement interface. b) Fit of the apparent resistivity and phase curves. The inverted data is represented as black points with associated error bars.

Figure 7 shows statistics of the stitched 1D model ensembles along the complete EW transect profile. Using the percentiles images in conjunction with the median allows to determine which areas of the model are constrained by the data. When the posterior distribution on resistivity resembles the prior distribution, which is uniform, it means that the model can take any resistivity and that the data has no resolution. The median image shows roughly the shape of the sedimentary basin at depth. The 5^{th} percentile, indicating the lower resistivity allowed by the data, shows that to the west of the profile, to a distance ~500 km, minimum resistivities of around 100 Ωm are required by the data, giving us confidence that the data is sensitive to the basement in this area. Same observation on the eastern end of the basin, from ~800 km onwards. In the deepest area of the basin, between ~500 km and ~800 km, at depths greater than 2 km, the percentiles resemble the prior model, suggesting a lack of resolution to observe the basement. This can be explained by 1) the data quality, which is poorest in this area, having reduced frequency range for most sites and 2) the presence of a thick conductor, which obscures the deeper part of the model, due to the MT skin depth effect. However, the 95^{th} percentile shows that some sites are sensitive to a deep conductor to a certain depth extent, constraining the lower depth at which the basement has to be located. Also, the median plot indicates that some sites are being potentially sensitive to the basement in this area, with higher resistivities. We can therefore conclude that some useful information regarding the basement can be extracted in the central area of the basin, despite the lower sensitivity of the data.

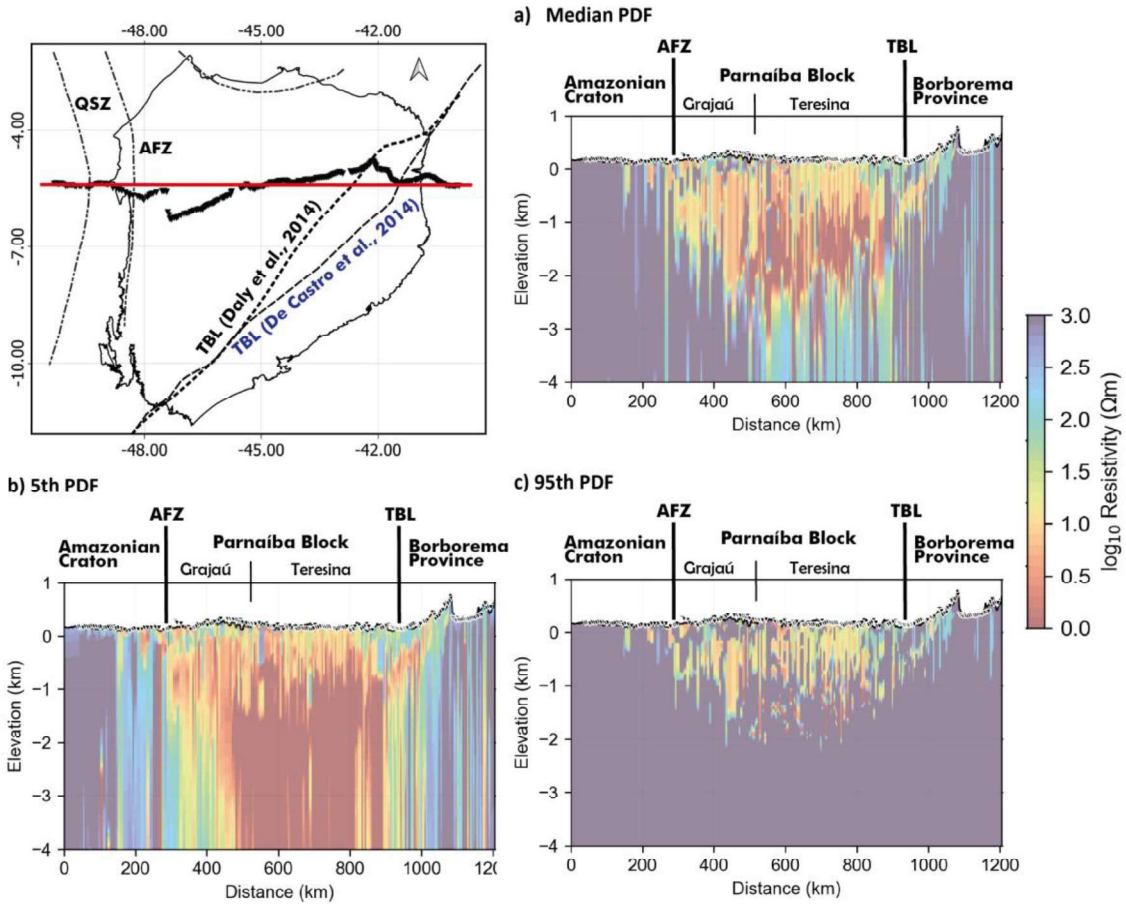


Figure 7. Cross-section of 1D stitched models derived from the probabilistic inversion, along the EW profile defined by the solid red line shown in the reference map in the upper-left corner. a) median resistivity model, b) 5th percentile model, and c) 95th percentile model. At the top of each model, the subdivision of the Parnaíba Basin into its main tectonic blocks is shown. Traces of the TBL - Transbrasiliano Lineament (Daly *et al.* 2014) and the AFZ - Araguaia Fault Zone are indicated for each profile.

4.3.2. Drillhole data analysis

A direct comparison between the 1D inversion models and drillhole data can provide insights regarding the geophysical response of the different lithologies present in the basin. Using a drillhole dataset from the National Petroleum Agency of Brazil, we selected the drillholes located closest to the MT survey. In total, four drillholes were selected, of which only two (2IZST and 2BAC) reach the basement, whereas the other

two (2NGST and 1PD) extend to the Tianguá Formation, the lowermost unit of the Serra Grande Group, which lies immediately above the basement. Table S2 in the Supplementary Material presents the depths of the total geological units identified in each drillhole. Figure 8a shows the location of the drillholes, while Figures 8b–8e present the correlation between the 1D resistivity models closest to each drillhole, the change-point and the corresponding lithostratigraphic columns of each drillhole.

Figure 8b shows the 1D posterior model distribution for site MT205, located 7km away from drillhole 2IZST. The 1D model shows a succession of 4 layers. The top of a conductive interface is visible at ~700 m depth, with values around 10 Ωm. The depth of the top of this conductive layer can be estimated using the change points probability distribution. Around those depths, the pic probability of the change point distribution correlates with the top of the Motuca Formation. This formation, composed mainly of siltstones with intercalations of limestone, evaporites and chert, can explain the resistivity value observed in the model. On the lithological log, the basement is observed at 2150 m depth. We do not observe a clear and sharp transition in the MT model at this depth. Instead, the model shows a progressive transition from a conductive to a resistive domain. However, the inflexion point of the median model appears to match well with the derived basement depth, suggesting a possible correlation. The original change point distribution does not show any particular mode that could indicate a clear layer interface. However, assuming that the basin/basement transition corresponds to a conductive/resistive transition, we will see in the next section that it is possible to isolate from the model ensemble the layer transition satisfying this condition, to estimate the depth to the basement. The absence of other correlations between lithologies and the MT model could have several explanations, the lack of resistivity contrast between lithologies, or the capability of the current MT data to resolve for subtle or thin transitions.

For MT site MT156 (Figure 8c, located 4.3 km away from the drillhole 2NGST), a transition into a conductive layer that appears to match the top the Motuca formation is observed, similar to the observation made for MT205. Similarly to MT140, a deep conductor (<1 Ωm) potentially associated to the Pimienteiras formation is observed,

519 with its top located around 2000m depth. For this site, the basement seems defined at
520 depths greater than 2500m, which is in accordance with the drillhole.
521
522 Figure 8d shows the posterior model probability distribution for MT site MT140, 17 km
523 distant from drillhole 2BAC. The 1D model shows a succession of 5 to 6 layers, which
524 correlate with some stratigraphic units, particularly with Motuca, Pedro de Fogo and
525 Poti. We observe a transition at ~ 600 m into a conductive layer of resistivity equal to 3
526 Ωm, which appear correlated to the top of the Motuca transition. Around 800 m depth
527 a transition into a more resistive layer appears correlated to the top of the Pedra de
528 Fogo formation. The top of a conductive layer with resistivities lower than 1 Ωm is
529 observed between approximately 1000 and 1200 m depth and appear to be associated
530 to the top of the Poti formation, which is composed mainly of sandstones and
531 carbonaceous shales, deposited in a fluvio–estuarine environment (Góes, 1995). The
532 correlation with the basement depth, observed at a depth of 3228 m in the drillhole, is
533 not observable in the MT model. For depths greater than 2300 m, for this MT site, we
534 observe that the posterior model distribution resembles the uniform prior distribution,
535 suggesting a lack of resolution at this depth, making the detection of the basement not
536 possible at this location.
537
538 For MT site 118 (Figure 8e, located 2.6 km away from the drillhole 1PD), we can also
539 observe the presence of a deep conductor (~1 Ωm) which top is roughly located where
540 the Pimienteiras formation appears in the drillhole. Here too, the model presents a
541 transition into a resistive layer that appears to be located at depths greater than 3000m,
542 which is in accordance with the drillhole.
543
544 It is important to note that given the distances between the drillholes and the MT
545 models, a perfect correlation cannot be expected. However, these observations serve
546 as a basis to identify specific resistivity variations trends detectable by the MT method
547 that are consistent across the profile. We have seen that the basement presents a
548 response in the models, coherent with the downhole observations. Also, in the areas
549 where the sedimentary basin appears to be the thicker, in the central part of the basin
550 (MT sites MT156, MT140 and MT118), a conductive layer is observed and could be

related to the Pimenteiras Formation, or potentially other formations within the Canindé sequence. We will therefore focus our effort in mapping the depth to the basement and the top of this conductive layer.

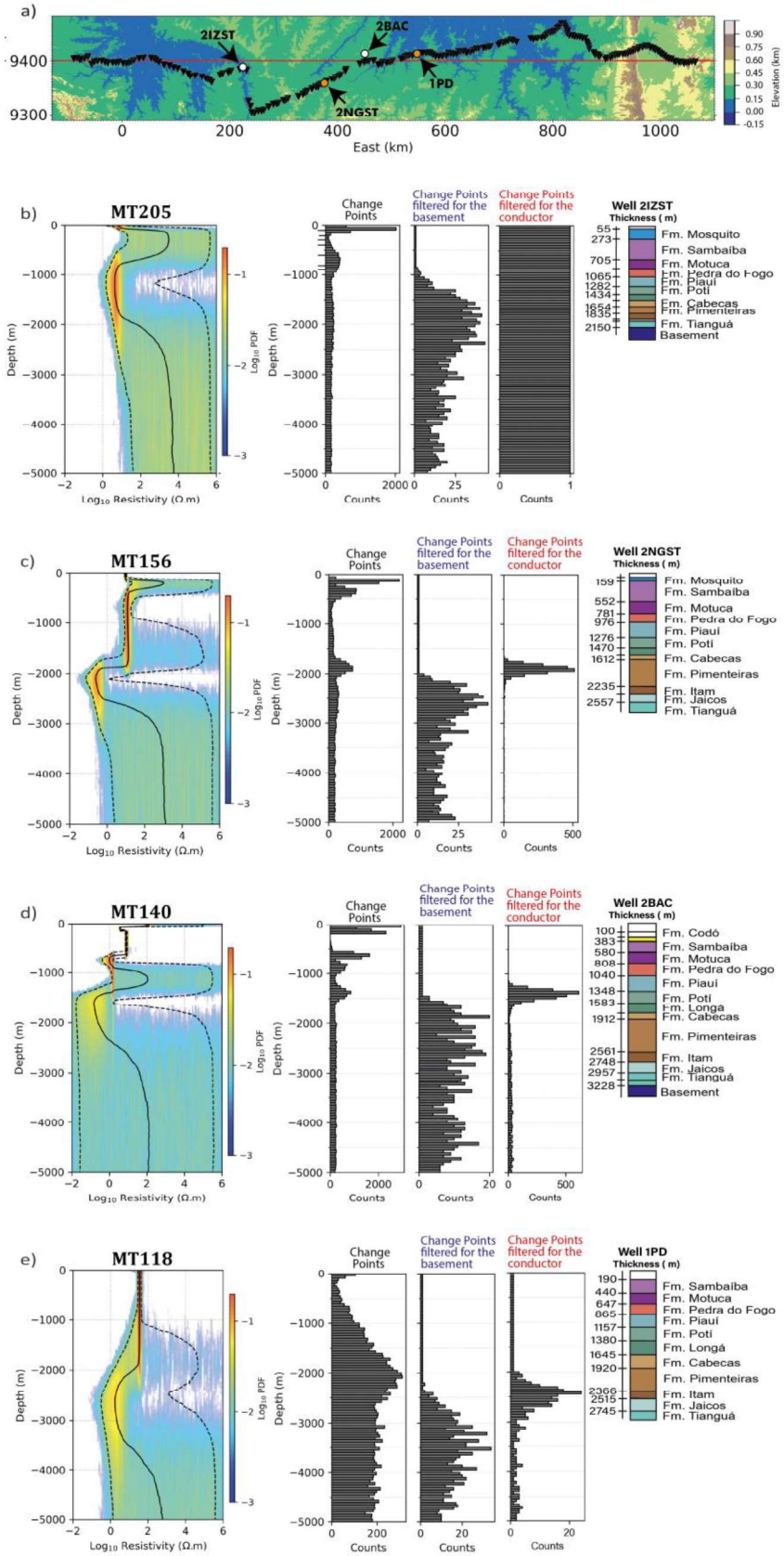


Figure 8. a) Drillhole locations and their respective labels on the topographic map, with the MT station distribution. The white points correspond to drillholes that reach the basement, while the orange ones do not. The figures below show the correlation between the interfaces from the one-dimensional resistivity models, the filtered change point analysis and the stratigraphic formations for b) drillholes 2IZST, c) 2BAC, d) 2NGST and e) 1PD.

4.3.3. Change-points analysis

We have seen in the previous section that the depth to basement and the top of the deep conductive feature are observable in the posterior model distributions, and to some extent in the interface distribution, the change points. The change point distributions are constructed by counting the number of transitions occurring within depth intervals, or bins, for all the models of the ensemble. Shallower layers are generally defined more accurately and with less uncertainty, as well as conductive layers, because of the sensitivity of the MT method. The change point distributions for each site along the profile is shown in Figure 9a. At shallow depths multiple layers with some lateral continuities are visible, most likely corresponding to sedimentary layers. However, a clear and consistent succession of layers cannot be reliably resolved.

The change points analysis consists in extracting from the posterior model ensembles information regarding the probabilities of specific types of interfaces to occur as a function of depth. We focus here on the depth to basement and the top of the deep conductive layer. Among the change points, only a subset corresponds to the transitions of interest. To select the layers associated to each transition, we apply a filtering criteria to remove from the posterior change point distributions the inconsistent transitions. The filtering process consists in analysing each transition of each 1D model from the ensemble. The resistivity of the upper layer is compared to the resistivity of the underlying layer, and the thickness of the underlying layer is also considered. When the resistivity contrast between the two successive layers satisfies a defined criterion, and the underlying is greater than a certain thickness, the transition is kept, otherwise

is filtered out. The resulting marginal distributions represents the probability to each interface as function of depth. These marginal distributions are constructed counting the number of interfaces per depth intervals. For the depth to basement, we record only the transitions that consist in a layer with resistivity < 500 Ωm, transitioning in an underlying layer with resistivity > 500 Ωm, with a minimum thickness of 1000 m (Figure 8 and Figure 9b). This resistivity value used as a criteria for filtering aligns with previous studies to detect depth to basement transitions (Seillé *et al.* 2021, Seillé *et al.* 2024). For the top of the conductive layer, we record only the transitions between layers with resistivity > 0.5 Ωm into a conductive layer of resistivity < 0.5 Ωm, with a minimum thickness of 100 m (Figure 8 and Figure 9c). This value was used after visually inspecting the posterior model ensembles. For the basement, between 1% and 10% of the total number of transitions are used to define the marginal distribution.

In Figure 8 is shown the filtering for individual sites. We observe that for sites MT205, MT140 and MT118, the derived depth to basement distributions present a main mode, with an approximately Gaussian shape, accompanied by long tails toward greater depths, associated with the progressive decrease in data sensitivity with depth. Comparing with, we observe a good match between that the resulting distributions and the drillholes. Site MT140 shows that the resulting depth to basement distribution is relatively flat past ~2000m, indicating a lack of resolution. The stitched posterior distributions (Figure 9b) show a good lateral continuity of the contact between the sedimentary sequence and the crystalline basement. The lack of resolution in the central part of the basin (between 400km and 800km) is visible with lower probabilities, contrasting with higher probability near the margins of the basin.

For the deep conductor, the resulting probability distributions are characterized by lower dispersion compared to those corresponding to the basement. This indicates that the depth of this conductive unit is better constrained by the MT data. Site MT205 does not present any transition satisfying the criteria described earlier, therefore has a quasi-null probability to exist in that location. In Figure 9c we see that the probability of observing this interface is restricted to the center of the basin, where the thicker sequence exists.

The next step consists in combining laterally those distributions, to obtain a probabilistic interface. Given the localised and relatively scattered distribution of the deep conductor, the change points distribution will not be combined and will be interpreted as it is.

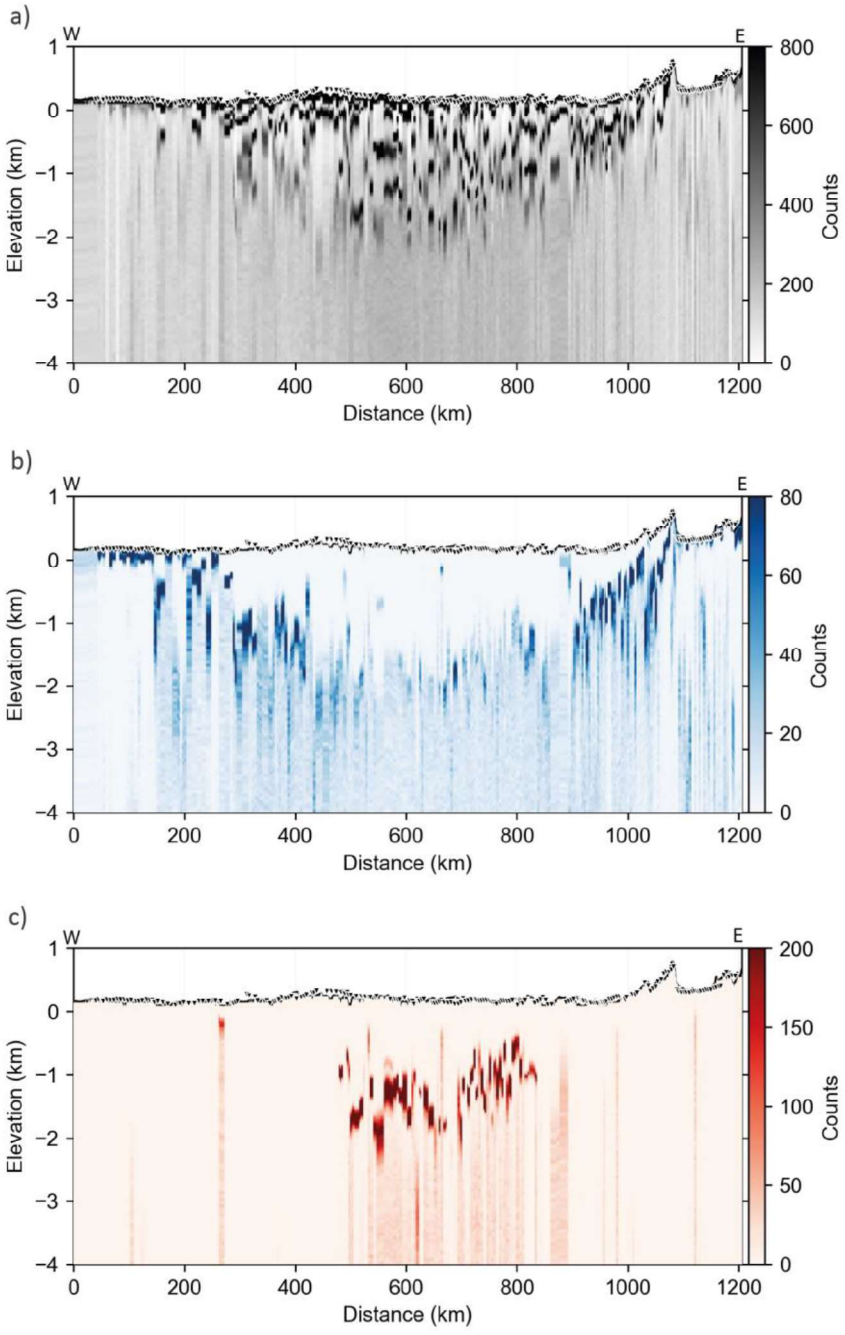


Figure 9. (a) Change-point analysis along the EW profile across the basin. Filtered results showing the interface layers corresponding to the basement (b), and the shallow conductive structure feature (c).

626 ## 5. Bayesian Estimate Fusion

627 ### 5.1. Methodology

628 The change points analysis allowed us to obtain probabilistic estimates of the depth
629 to at the location of each MT sites along the profile. We also have information regarding
630 the depth to basement coming at 4 drillhole locations and structural information. Our
631 goal is to combine those datasets to derive a depth to basement probabilistic map along
632 the profile. In other type of application (Seillé *et al.* 2024), the combination of different
633 probabilistic datasets has shown that it can help reduce uncertainties present in each
634 individual dataset, as well as leveraging the limitations of individual observations. In our
635 case, we observe a good lateral continuity of the MT depth to basement estimates along
636 the profile, but with a lack of resolution in the deeper parts of the basin. On the other
637 hand, we have accurate depth to basement estimates coming from drill hole
638 observations in the deeper part of the basin, but with a very limited coverage (only 4
639 drill holes along the profile). We can see that these datasets complement well each
640 other's to obtain a coherent image along all the profile.
641
642 In this study, we apply the Bayesian Ensemble Fusion (BEF) algorithm (Visser & Markov,
643 2019) to combine these different datasets. It consists in deriving a depth to basement
644 posterior distribution in 3D, approximated by an ensemble of 2D surfaces. The posterior
645 distribution is evaluated using a MCMC sampling method, given the input probabilistic
646 depth estimates. The main advantages of this method over other interpolation methods
647 are its capability to handle multimodality in the input estimates and its robustness in
648 dealing with outliers (Visser & Markov, 2019). This algorithm was successfully used for
649 cover mapping in previous studies (Seillé *et al.* 2021, Seillé *et al.* 2024).
650
651 The MT estimations of the depth to an interface are defined based upon variations of
652 the electrical resistivity. The downhole estimations are direct observations of geology.
653 Both types of observations can be integrated into a common framework to define a
654 single estimation, in that case depth to basement depth, using probability distributions.
655 They can consider discrepancies between different estimates. For the case of the depth
656 to basement for example, if a weathered basement exists, which will have a lower

resistivity than a fresh basement, the match between the geological observation and the geophysical observation will not be exact. These discrepancies can be handled by the uncertainties considered in both datasets. The drill hole interface estimates are therefore defined as Gaussian distributions centered on the interface estimation, with an uncertainty considering this possible discrepancy as well as the existing uncertainty existing in the drill hole interpretation.

To obtain a continuous surface from discrete observations located on a survey or along a profile, interpolations methods such as kriging or the BEF relies on the definition of a variogram model. It defines the spatial continuity between the different estimates, i.e. the expected variation in depths of the different estimates as a function of the distance between them. The BEF algorithm allows to incorporate the location of surface faults to allow for sharp lateral discontinuities, relaxing continuity constraints.

5.2. Depth to basement probabilistic map

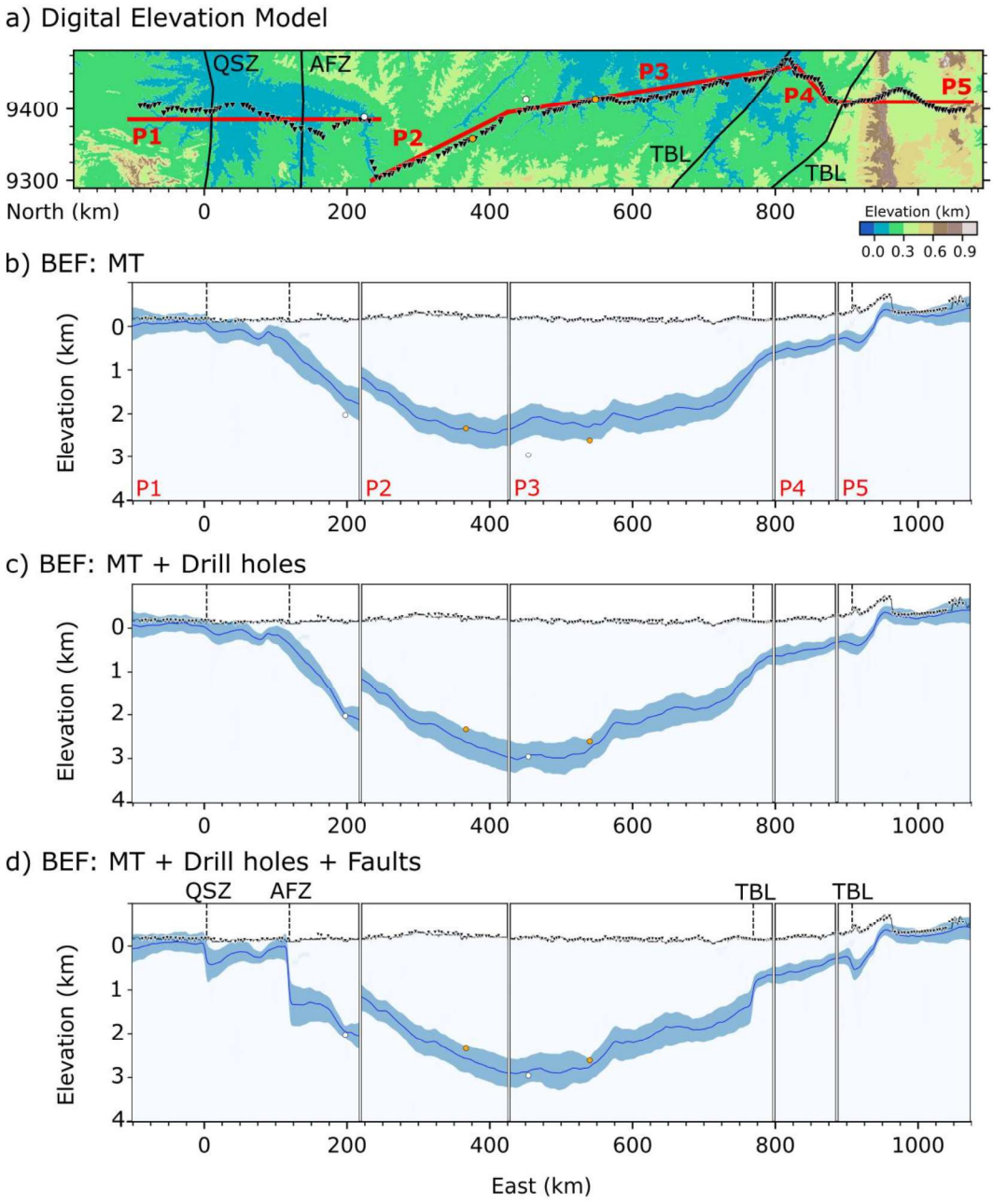
For the depth to basement, we use depth estimates derived from MT, as derived from the change points analysis, four major NS oriented faults crossing the profile, and four drill holes. We considered The Quatipuru and Araguaia suture zones, located west of the profile, and the two interpretations of the Transbrasiliano Lineament situated in the western sector of the profile. Only 2 drill holes reach the basement along the profile. While the other 2 drill holes do not reach the basement, they can be used as an inequality constraint (Visser & Markov 2019). It consists in assigning the deepest recorded value along the drill hole as an upper limit for the depth to basement at this location.

The estimation of the depth to basement using the BEF was carried out combining the data in three different ways: (i) the MT estimates alone, (ii) the MT estimates together with the drill hole estimates and (ii) the MT estimates with both drill hole estimates and structural constraints. The estimate fusion was performed over the area of interest using a regular grid with a horizontal resolution of 2000 m × 2000 m. The grid consists of 671 cells in the E–W direction and 97 cells in the north–south direction, yielding a total of

65087 cells. Although no vertical discretization is applied within the BEF during the interpolation process, the resulting probabilities are evaluated on a vertical grid with a constant spacing of 5m. The fusion was carried out using 50 Markov chains, each comprising 5 million iterations, with the final 30% of the iterations used to approximate the posterior distribution.

The results are presented along the E–W profile (Figure 10) and in plan-view (Figure 11). The image in Figure 10 consists in 5 stitched individual profiles, which closely follow the location of the MT sites. Note that there is no continuity between profile P1 and profile P2. The other profiles have continuity. In Figure 11, the 50^{th} percentile of the posterior depth to basement distribution is shown by a blue line in the models, while the 10^{th} and 90^{th} percentiles are represented by the light-blue shaded band. In Figure 11, the map of the mean depth to basement distribution and its standard deviation is shown. The 3D posterior probability density of the depth to basement can be interpreted using these visualizations. We observe that the lowest uncertainty is localized close to the observations and increases away from the profile. The profile follows closely the profile along 5 different profile and therefore presents the lowest uncertainty.

Overall, the results obtained using the different types of data combinations are relatively similar. Using only MT data (Figure 10b), we observe that the prediction of the depth to basement is only slightly underestimated respect to the existing drillholes, despite the lack of MT resolution existing in the central part of the profile. Adding the drillholes (Figure 10c), the posterior distribution is observed deeper. When adding the faults (Figure 10d), sharper variations on the lateral continuity is observed at the location of the faults. These sharp variations were already visible in the stitched 1D models (Figure 7a) and in the depth to basement change points (Figure 9b). Therefore, relaxing the lateral continuity in those locations allows to match more closely the input MT data, and to produce an image that is more aligned with the geological data.



717

718 **Figure 10.** a) Topography map with 5 profiles displayed. Depth to basement posterior
719 distribution for the combination of (b) the MT estimates alone, (c) MT estimates + drill
720 hole estimates, (d) MT estimates + drill hole estimates + structural constraints. The 10th,
721 50th and 90th percentile are displayed. Drill holes estimates are superimposed on each
722 model, represented by orange and white dots.

723

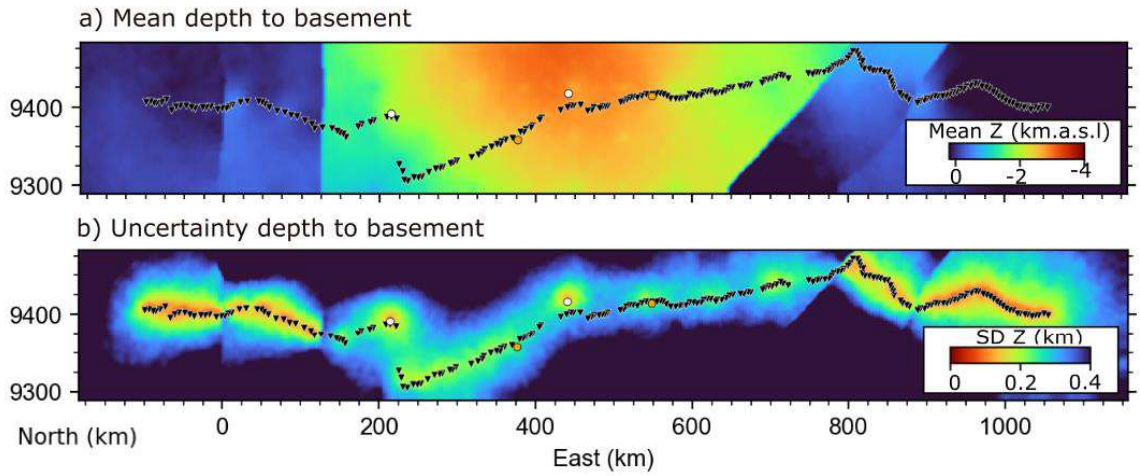


Figure 11. a) Mean basement depth model derived from MT data + drill holes + fault constraints, along with b) its associated uncertainty.

6. Geological interpretation and discussion

6.1. Interpretation of the depth to basement probabilistic model

The shape of the basement geometry, intuited in the pseudosections (Figure 3), and defined roughly in the stitched 1D model medians (Figure 7a) and the filtered change-point (Figure 9b), has gained in reliability thanks to the inclusion of drillhole and geological data. Additionally, our model is consistent with the previously proposed basement model by Daly *et al.* (2018). The latter builds upon the earlier work of Daly et al. (2014), which is based on seismic reflection data, which in turn shows similarity to the model proposed by Soares et al. (2018), derived from seismic refraction data.

Figure 12 shows the superposition of the model of Daly *et al.* (2018) and our model. Although the two models are not exactly coincident, we observe a good match. Our model shows a Phanerozoic sedimentary sequence that reach ~3 km thick in its center and extends across the three Precambrian blocks, along with sharp lateral variations in the basement geometry across the basin. The transition between the Parnaíba Block and the Borborema Province is less abrupt compared to the transition between the Parnaíba Block and the Amazonian Craton to the west, characterized by eastward dipping faults. This asymmetry in basement architecture reflects differences in the tectonic evolution of these domains, with the sharper transition toward the Amazonian Craton interpreted

747 as the result of compressional deformation, possibly associated with thrusting during
748 collisional events. In contrast, the transition toward the east indicates a deformation
749 distributed along the Borborema Province or the reactivation of pre-existing lithospheric
750 structures, possibly associated with at least one of the three reactivation episodes of the
751 Transbrasiliano Lineament (Brito Neves *et al.* 1999).
752
753 The main difference between our model and Daly *et al.* (2018) model lies in the region
754 between the two interpretations of the Transbrasiliano Lineament (TBL). In our model,
755 this area exhibits a pronounced basement elevation, whereas in the model of Daly *et al.*
756 (2018) the basement appears relatively continuous, with smoother topographic
757 variations. This region coincides with the reported occurrence of Cambrian–Ordovician
758 grabens, whose formation has been linked to magmatic processes, particularly
759 lithospheric heating associated with underplating (Oliveira & Mohriak, 2003; Oliveira,
760 2001). In the same location, Romero-Beltran *et al.* (2025) presents a Bouguer anomaly
761 map where a gravity high associated with magmatic intrusions related to the Mosquito
762 formation is observed. The discrepancy between our model and the model derived from
763 seismic data may be attributed to the different sensitivity of the MT and seismic
764 methods to the geological features. In the presence of horizontally extended magmatic
765 intrusions within the sedimentary sequences, the contrast in electrical conductivity
766 could appear at the top of the magmatic intrusion, assuming a resistive behaviour of
767 such intrusion.
768
769 On the western part of the Parnaiba block, in the Grajaú domain, around km 300 (Figure
770 12), our model shows an abrupt jump, which is due to the kink in the MT line: the eastern
771 end of profile P1 (Figure 10a) shows the basement at a depth of ∼2km. On the western
772 end of profile P2 (Figure 10a), the basement appears at ∼1km depth. Those points are
773 separated 100km in the north-south direction. In our model, this transition is smooth
774 towards the north and indicates that the basin is thickening northwards. This behaviour
775 matches deeper observations, where the crustal thickness has been observed to thicken
776 northwards (Porto et al. 2022 and references therein).
777

The Teresina domain in the eastern part of the Parnaiba Block is characterized by a relatively gentle basement slope, in contrast to the Grajaú domain to the east, where basement geometry has a steeper slope. This contrast could reflect the presence of the Grajaú High, a Cretaceous structural feature also referred to as the Grajaú Basin (Goés & Rossetti, 2001), which developed in response to a broad regional uplift during the Aptian–Albian (Ibanez et al. 2017).

Our model does not reveal the presence of an underlying rift system, suggesting that the basement was not significantly affected by extensional processes that could have dominated the formation of the basin. Instead, our results are consistent with the conclusions of Daly et al. (2018), who indicate that no significant extensional deformation occurred. Therefore, lithospheric and thermal subsidence mechanisms likely played a primary role in the formation and evolution of the basin (Watts et al. 2018; Mckenzie & Rodríguez Tribaldos, 2018).

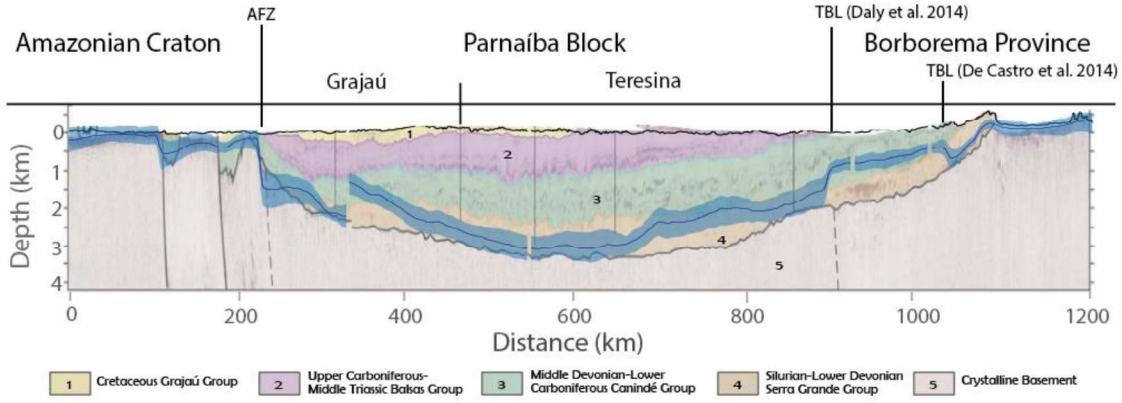


Figure 12. Geological cross-section of the Parnaíba Basin (adapted from Daly et al. 2018), onto which the mean basement model is superimposed, represent by the blue line, together with the associated uncertainty shown as a blue shaded band.

6.2. Interpretation of the Conductivity Anomaly

In the Parnaíba Basin, magmatic activity associated with the Mosquito and Sardinha formations played an important role in the evolution of the petroleum system. This activity involved the emplacement of numerous magmatic intrusions within the sedimentary sequence, which contributed to the thermal maturation of organic-rich units, enhanced hydrocarbon generation and migration, and promoted the development of stratigraphic trapping mechanisms (Rodrigues, 1995). The thermal and mechanical effects produced by these intrusions likely modified the physical properties of the surrounding sedimentary rocks. In particular, the magma emplacement may have induced fracturing and extensional processes within the marine shales of the Poti Formation, increasing their porosity and promoting secondary mineralization and cementation processes. These alterations may significantly modify the electrical properties of these units by facilitating the circulation and accumulation of conductive fluids. These processes may explain the pronounced conductivity anomaly observed at the base of the sedimentary sequence in the central part of the basin (<10 Ωm), particularly within the Teresina Domain. This interpretation is similar to that proposed by Corseri *et al.* (2023, 2024), who identified highly conductive anomalies in the Bjørnøya Basin attributed to marine shales subjected to extensional events. However, an additional increase in conductivity associated with post-sedimentary alteration processes cannot be ruled out. This process may be linked to changes in the location of the depocenter along the sedimentary deposition (Vaz *et al.* 2007), which likely modified the pore-space geometry and connectivity, resulting in a more diffuse boundary between the sedimentary sequences and the basement.

Although these very low resistivity values differ from those typically observed in hydrocarbon reservoirs (< 30 Ωm; Meju, 2002), extensional or compressional tectonic forces can modify basin architecture and the thermal gradient of petroleum systems (Allen & Allen, 2013), thereby influencing the bulk resistivity. Furthermore, this conductive anomaly spatially coincides with the high seismic velocity anomaly (5.5 km s^{-1}) reported by Soares *et al.* (2018), which has been associated with magmatic

intrusions emplaced within the basin and is considered a target of interest for hydrocarbon exploration.

7. Conclusion

A probabilistic depth to basement map across the Parnaíba Basin was derived using a Bayesian Estimate Fusion approach. This approach integrated results from 1D trans-dimensional Bayesian inversions of MT data, drillhole and structural information. The geometry of the basin we obtained is geologically realistic and agrees with existing results derived using seismic data. Furthermore, we identified a conductive anomaly which has been interpreted to be associated with the Poti and Cabeças formations, which are related to hydrocarbon-bearing zones in the central part of the basin.

The Bayesian MT inversions were performed using uninformed priors, ensuring that the results were not biased toward any predefined geological model. A semi-automated change-point analysis was used to extract transitions into conductive or resistive layers, associated to the interface between the sedimentary cover and the crystalline basement or to the top of the conductive feature we studied. The workflow we applied showed that the resolution of the MT models can be improved in the near-surface compared to a 3D deterministic inversion, which can often be limited by coarse mesh discretization, smoothness constraints and starting model assumptions.

Overall, our work shows that combining MT data, drill hole and structural information within a probabilistic framework which rigorously consider input data uncertainties provides a robust and effective strategy to characterize geological features such as the basement geometry or a conductive anomaly. In future studies, inclusion of higher-quality datasets and a larger number of drill holes would allow to further enhance the resolution and reliability of the probabilistic basement-depth model, broadening their potential for structural interpretation and geological exploration.

Acknowledgements

G.R.B gratefully acknowledges the support of the CAPES Sandwich Doctorate Program (Process No. 88881.934129/2024-01**)** which funded the research visit to CSIRO in Australia. We acknowledge the CSIRO High Performance Computing facilities. H.S and G.V thanks CSIRO Mineral Resources for the support during the course of this work.

Data Availability

The data used in this study are privately owned and confidential; therefore, they cannot be publicly disclosed.

References

Abelha, M., Petersohn, E., Bastos, G., & Araújo, D., 2018. New insights into the Parnaíba Basin: results of investments by the Brazilian National Petroleum Agency. *Geological Society, London, Special Publications* 472, 361-366

Allen, P. A., & Allen, J. R., 2013. *Basin analysis: Principles and application to petroleum play assessment*. John Wiley & Sons.

Almeida, F. F., 1986. Distribuição regional e relações tectônicas do magmatismo pós-paleozóico no Brasil. *Revista Brasileira de Geociências*, *16*(4), 325-349.

Ardid, A., Dempsey, D., Bertrand, E., Sepulveda, F., Tarits, P., Solon, F., & Archer, R., 2021. Bayesian magnetotelluric inversion using methylene blue structural priors for imaging shallow conductors in geothermal fields. *Geophysics*, *86*(3), E171-E183.

Berdichevsky, M. N., Vanyan, L. L., Kuznetsov, V. A., Levadny, V. T., Mandelbaum, M. M., Nechaeva, G. P., Okulessky, B.A., Shilovsky, P.P. & Shpak, I. P., 1980. Geoelectrical model of the Baikal region. *Physics of the Earth and Planetary Interiors*, *22*(1), 1-11.

Bibby, H. M., Caldwell, T. G., & Brown, C., 2005. Determinable and non-determinable parameters of galvanic distortion in magnetotellurics. *Geophysical Journal International*, *163*(3), 915-930.

Brito Neves, B. B., Neto, M.C & Fuck, R.A., 1999. From Rodinia to Western Gondwana: An approach to the Brasiliano-Pan African Cycle and orogenic collage, *Episodes*, 22(03), 155–166.

Cai, H., & Zhdanov, M., 2016. Three-dimensional inversion of magnetotelluric data for the sediment–basement interface. *IEEE Geoscience and Remote Sensing Letters*, *13*(3), 349-353.

Caldwell, T. G., Bibby, H. M., & Brown, C., 2004. The magnetotelluric phase tensor. *Geophysical Journal International*, *158*(2), 457-469.

Caputo, M. V., & Santos, R. O. B., 2020. Stratigraphy and ages of four Early Silurian through Late Devonian, Early and Middle Mississippian glaciation events in the Parnaíba Basin and adjacent areas, NE Brazil. *Earth-Science Reviews*, *207*, 103002.

Chave, A. D., & Jones, A. G. (Eds.)., 2012. *The magnetotelluric method: Theory and practice*. Cambridge University Press.

Chen, J., Hoversten, G. M., Key, K., Nordquist, G., Cumming, W., 2012. Stochastic inversion of magnetotelluric data using a sharp boundary parameterization and application to a geothermal site. *Geophysics*, *77*(4), E265-E279.

Conway, D., Simpson, J., Didana, Y., Rugari, J., & Heinson, G., 2018. Probabilistic magnetotelluric inversion with adaptive regularisation using the no-U-turns sampler. *Pure and Applied Geophysics*, *175*(8), 2881-2894.

Corseri, R., Planke, S., Gelius, L.J., Faleide, J.I., Senger, K., & Abdelmalak, M.M., 2023. Magnetotelluric image of a hyper-extended and serpentinized rift system, Earth planet. Sci. Lett., 602, doi:10.1016/j.epsl.2022.117914. 10.1016/j.epsl.2022.117914

Corseri, R., Seillé, S., Faleide, J.I., Planke, S., Senger, K., Abdelmalak, M.M., Gelius, L.J, Mohn, G., & Visser, G., 2024. Deep basin conductor characterization using machine

925 learning-assisted magnetotelluric Bayesian inversion in the SW Barents Sea, *Geophysical*
926 *Journal International*, Volume 238, Issue 1, Pages 420–
927 432, https://doi.org/10.1093/gji/ggae166
928
929 Daly, M. C., Andrade, V., Barousse, C.A., Costa, R., McDowell, K., Piggott, N., & Poole,
930 A.J., 2014. Brasiliano crustal structure and the tectonic setting of the Parnaíba basin of
931 NE Brazil: Results of a deep seismic reflection profile, Tectonics, 33, 2102–2120,
932 doi:10.1002/2014TC003632.
933
934 Daly, M. C., Fuck, R. A., Julià, J., Macdonald, D. I., & Watts, A. B., 2018. Cratonic basin
935 formation: a case study of the Parnaíba Basin of Brazil. *Geological Society, London,*
936 *Special Publications*, (472),1-15. https://doi.org/10.1144/SP472.20
937
938 De Castro, D. L., Fuck, R. A., Phillips, J. D., Vidotti, R. M., Bezerra, F. H., & Dantas, E. L.,
939 2014. Crustal structure beneath the Paleozoic Parnaíba Basin revealed by airborne
940 gravity and magnetic data, Brazil. *Tectonophysics*, *614*, 128-145.
941
942 Egbert, G. D., 1997. Robust multiple-station magnetotelluric data
943 processing. *Geophysical Journal International*, *130*(2), 475-496.
944
945 Glover, P. W. J., 2015. Geophysical properties of the near-surface Earth: Electrical
946 properties. In G. Schubert (Ed.), *Treatise on Geophysics* (2nd ed., Vol. 11, pp. 89–137).
947 Elsevier. https://doi.org/10.1016/B978-0-444-53802-4.00011-3
948
949 Góes, A. M., & Feijó, F. J., 1994. Parnaiba Basin; Bacia do Parnaiba. *Boletim de*
950 *Geociências da PETROBRAS*, *8*.
951
952 Góes, A. M., Souza, J. M. P., & Teixeira, L. B., 1990. Estágio exploratório e perspectivas
953 petrolíferas da Bacia do Parnaíba. *Boletim de Geociencias da PETROBRAS*, *4*(1), 55-64.
954
955 Góes, A.M., & Rossetti, D.F., 2001. Gênese da Bacia de São Luís-Grajaú, Meio-Norte do
956 Brasil. In: Rossetti, D.F., Góes, A.M., & Truckenbrodt, W. (Eds.), O Cretáceo na Bacia de

São Luís-Grajaú, Belém: Museu Paraense Emílio Goeldi, Coleção Friedrich Katzer, p.15-29.

Góes, A. M. (1995), Formação Poti (Carbonífero inferior) da Bacia do Parnaíba, PhD thesis, Universidade de São Paulo, Brazil.

Henneking, S., Venkat, S., Dobrev, V., Camier, J., Kolev, T., Fernando, M., Gabriel, A.A., & Ghattas. O., 2025. Real-Time Bayesian Inference at Extreme Scale: A Digital Twin for Tsunami Early Warning Applied to the Cascadia Subduction Zone. In Proceedings of the International Conference for High Performance Computing, Networking, Storage and Analysis (SC '25). Association for Computing Machinery, New York, NY, USA, 60–71. https://doi.org/10.1145/3712285.3771787

Hautot, S., Whaler, K., Gebru, W., & Desissa, M.,2006. The structure of a Mesozoic basin beneath the Lake Tana area, Ethiopia, revealed by magnetotelluric imaging. Journal of African Earth Sciences, 44(3), 331-338.

Ibanez, D. M., Pestilho, A. L., Turra, B. B., Destro, N., Miranda, F. P., Riccomini, C., Lammonglia, T., Dubois, D.S, & Schmidt, J. S., 2017. Stress variability in the Parnaíba Basin, Brazil, during Cretaceous rifting. Tectonophysics, 699, 1-15.

Junge, A., 1996. Characterization of and correction for cultural noise. *Surveys in Geophysics*, *17*(4), 361-391.

Magee, C., & Jackson, C., 2020. Can we relate the surface expression of dike-induced normal faults to subsurface dike geometry? *Geology* 49 (4): 366–371. doi: https://doi.org/10.1130/G48171.1

Magrini, F., & Sambridge, M., 2025. Transport-Map Proposals for Efficient Markov Chain Monte Carlo. Geophysical Journal International, ggag002.

Manassero, M.C., Afonso, J.C., Zyserman, F., Zlotnik, S., & Fomin, I., 2020. A reduced order approach for probabilistic inversions of 3-D magnetotelluric data I: general formulation, *Geophysical Journal International*, 223, (3), 1837-1863, https://doi.org/10.1093/gji/ggaa415

McKenzie, D. & Rodríguez Tribaldos, V., 2018. Lithospheric heating by crustal thickening: a possible origin of the Parnaíba Basin. *In*: Daly M.C., Fuck R.A., Julià J., Macdonald D.I.M. & Watts A.B. (eds) *Cratonic Basin Formation: A Case Study of the Parnaíba Basin of Brazil*. Geological Society, London, Special Publications, 472. First published online June 7, 2018, https://doi.org/10.1144/SP472.7

Meju, M. A., 2002. Geoelectromagnetic exploration for natural resources: models, case studies and challenges. *Surveys in Geophysics*, *23*(2), 133-206.

Milani, E. J., & Zalán, P. V., 1999. An outline of the geology and petroleum systems of the Paleozoic interior basins of South America. *Episodes Journal of International Geoscience*, *22*(3), 199-205.

Milani, E. J., & Tomaz Filho, A., 2000. Sedimentary basin of South America. *In:* Tectonic evolution of South America. Publisher: 31. International Geological Congress. p.389-352. Rio de Janeiro-Brasil.

Mussa, A., Kalkreuth, W., Mizusaki, A. M. P., & Bicca, M. M., 2021. Geochemical characterization of selected organic-rich shales from the Devonian Pimenteiras Formation, Parnaíba Basin, Brazil–Implications for methane adsorption capacity. *Journal of South American Earth Sciences*, *112*, 103507.

Oliveira, D. C., & Mohriak, W. U., 2003. Jaibaras trough: an important element in the early tectonic evolution of the Parnaıba interior sag basin, Northern Brazil. *Marine and Petroleum geology*, *20*(3-4), 351-383.

Oliveira, C. V., & Moura, C. V., 2019. Provenance of detrital zircons of the Canindé group (Parnaíba Basin), northeastern Brazil. *Journal of South American Earth Sciences*, *90*, 162-180.

Oliveira, D. C. (2001). Reavaliação da evolução tectono-magmática do Graben de Jaibaras (nordeste do Brasil). Acta Geologica Hispanica, 36(1/2), 53–95

Pedersen, L. B., & Engels, M., 2005. Routine 2D inversion of magnetotelluric data using the determinant of the impedance tensor. *Geophysics*, *70*(2), G33-G41.

Porto, A., Carvalho, C., Lima, C., Heilbron, M., Caxito, F., La Terra, E., & Fontes, S. L., 2022. The Neoproterozoic basement of the Parnaíba Basin (NE Brazil) from combined geophysical-geological analysis: A missing piece of the western Gondwana puzzle. *Precambrian Research*, *379*, 106784.

Rodrigues, R., 1995. A geoquímica orgânica na Bacia do Parnaíba. PhD thesis. Universidade Federal do Rio Grande do Sul, Porto Alegre, Brasil.

Romero-Beltran, G., La Terra, E. F., Panetto, L. P., & Seillé, H., 2025. Magnetotelluric imaging of the Parnaíba Basin: Implications to the West Gondwana formation. *Tectonophysics*, 230777.

Rosas-Carbajal, M., Linde, N., Peacock, J., Zyserman, F. I., Kalscheuer, T., & Thiel, S., 2015. Probabilistic 3-D time-lapse inversion of magnetotelluric data: application to an enhanced geothermal system. *Geophysical Supplements to the Monthly Notices of the Royal Astronomical Society*, *203*(3), 1946-1960.

Schiffer, C., de Lima, M. V., Soares, J. E., Stephenson, R., de Araújo, V. C., Lima, F. T., Rocha, A.S., Trindade, C.R., & Fuck, R. A., 2021. Vp/Vs ratios in the Parnaíba Basin from joint active-passive seismic analysis–Implications for continental amalgamation and basin formation. *Tectonophysics*, *801*, 228715.

Selway, K. (2014). On the causes of electrical conductivity anomalies in tectonically stable lithosphere. Surveys in Geophysics, 35(1), 219-257.

Seillé, H., & Visser, G., 2020. Bayesian inversion of magnetotelluric data considering dimensionality discrepancies. *Geophysical Journal International*, 223(3), 1565–1583. https://doi.org/10.1093/gji/ggaa391

Seillé, H., Visser, G., Markov, J., & Simpson, J., 2021. Probabilistic Cover-Basement Interface Map in Cloncurry, Australia, Using Magnetotelluric Soundings. *Journal of Geophysical Research: Solid Earth*, *126*(7), e2021JB021883.

Seillé, H., Thiel, S., Brand, K., Mulè, S., Visser, G., Fabris, A., & Munday, T., 2024. Bayesian fusion of MT and AEM probabilistic models with geological data: examples from the eastern Gawler Craton, South Australia. *Exploration Geophysics*, *55*(Special Issue: Lithospheric to deposit scale magnetotellurics advancements, including AusLAMP in Australia), 486-505.

Simpson, F., & Bahr, K., 2005. *Practical magnetotellurics*. Cambridge University Press.

Soares, J.E.P., Stephenson R., Fuck, R.A., de Lima M., de Araújo, V., Lima, F.T, Rocha, F., & da Trindade, C. R., 2018. Structure of the crust and upper mantle beneath the Parnaíba Basin, Brazil, from wide-angle reflection–refraction data. *In*: Daly M.C., Fuck R.A., Julià J., Macdonald D.I.M. & Watts A.B. (eds) *Cratonic Basin Formation: A Case Study of the Parnaíba Basin of Brazil*. Geological Society, London, Special Publications, 472. First published online April 13, 2018, https://doi.org/10.1144/SP472.9

Szarka, L. (1988). Geophysical aspects of man-made electromagnetic noise in the earth—A review. *Surveys in Geophysics*, *9*(3), 287-318.

Tarantola, A. 2005. *Inverse problem theory and methods for model parameter estimation*. SIAM. https://doi.org/10.1137/1.9780898717921

Thomaz Filho, A., Mizusaki, A. M., Milani, E. J., & De Cesero, P., 2000. Rifting and magmatism associated with the South America and Africa break up. *Revista Brasileira de Geociências*, *30*(1), 017-019.

Thomaz Filho, A., Mizusaki, A. M. P., & Antonioli, L., 2008. Magmatism and petroleum exploration in the Brazilian Paleozoic basins. *Marine and petroleum geology*, *25*(2), 143-151.

Tozer, B., Watts, A.B., & Daly, M.C., 2017. Crustal structure, gravity anomalies, and subsidence history of the Parnaíba cratonic basin, Northeast Brazil. *J. Geophys. Res. Solid Earth*, 122, 5591–5621, doi:10.1002/2017JB014348.

Vaz, P. T., Wanderley Filho, J. R., & Travassos, W. A. S., 2007. Bacia do Parnaíba. *Boletim de Geociências da PETROBRAS*, *15*(2), 253-263.

Visser, G., & Markov, J., 2019. Cover thickness uncertainty mapping using Bayesian estimate fusion: Leveraging domain knowledge. *Geophysical Journal International*, 219(3), 1474–1490. https://doi.org/10.1093/gji/ggz358

Vozoff, K.,1972. The magnetotelluric method in the exploration of sedimentary basins. Geophysics, 37(1), 98-141.

Watts, A.B., Tozer, B., Daly, M.C. & Smith, J., 2018. A comparative study of the Parnaíba, Michigan and Congo cratonic basins. *In*: Daly M.C., Fuck R.A., Julià J., Macdonald D.I.M. & Watts A.B. (eds) *Cratonic Basin Formation: A Case Study of the Parnaíba Basin of Brazil*. Geological Society, London, Special Publications, 472. First published online February 22, 2018, https://doi.org/10.1144/SP472.6

Supporting Material for

Structure of the Parnaíba Basin inferred from Bayesian inversion of magnetotelluric data.

Gonzalo Romero-Beltran[1], Hoël Seillé[2], Emanuele F. La Terra[1], Liliane P. Panetto[1,3], Gerard Visser.[2]

[1] National Observatory, Department of Geophysics, Rua Jose Cristino 77, Rio de Janeiro, Brazil

[2] CSIRO Mineral Resources, Kensington, WA, Australia

[3] Federal Rural University of Rio de Janeiro, Department of Petrology and Geotectonics, Seropédica, Rio de Janeiro, Brazil

Contents of this file:

Table S1 to S2

Figure S1 to S5

Introduction

This document includes additional texts and figures that explain and justify the magnetotelluric data analysis presented in the main paper.

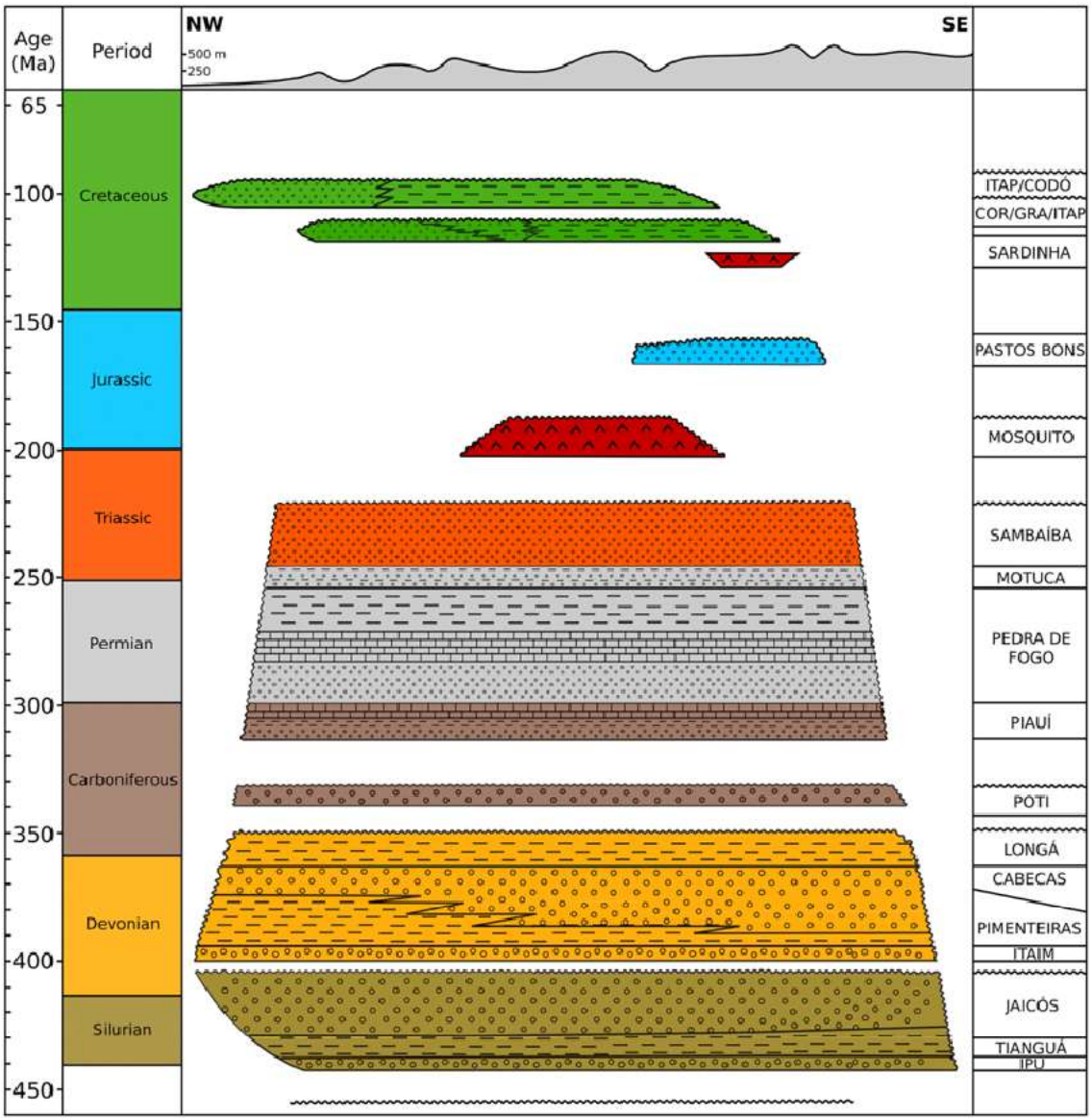


Figure S1. Lithostratigraphic column of the Parnaiba Basin. From Klöcking et al. (2018)

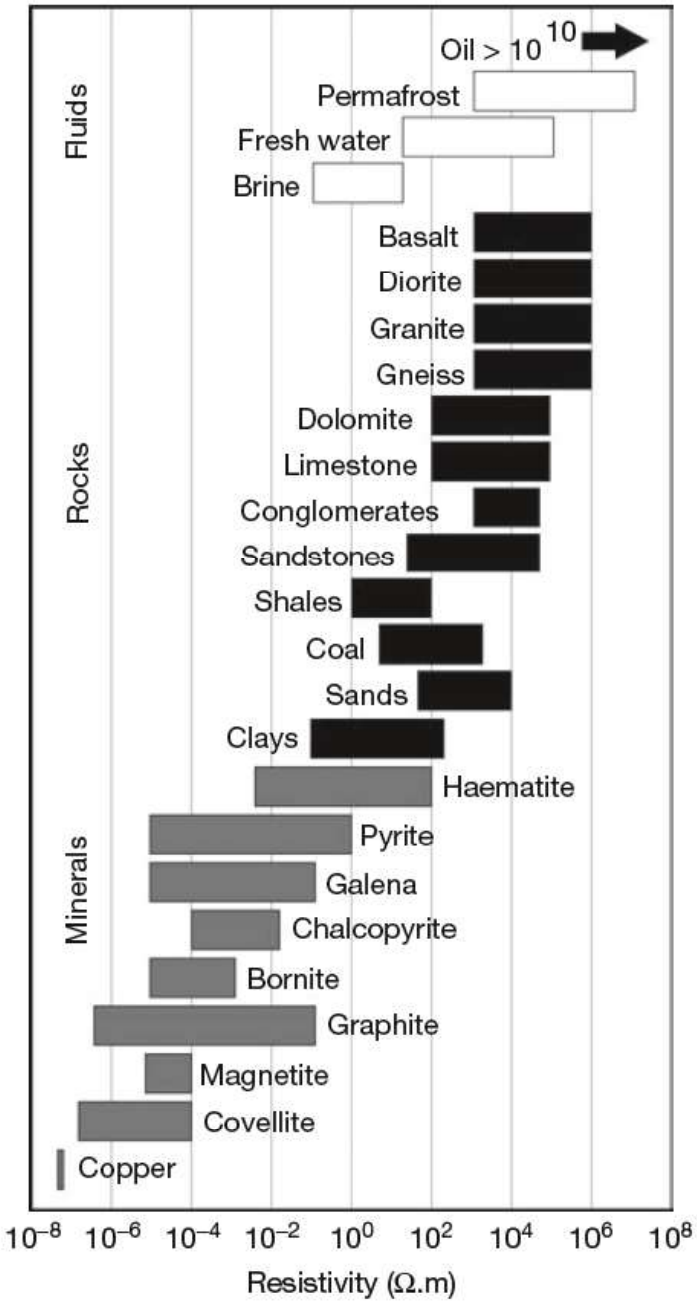


Figure S2. Electrical resistivity of several geomaterial. From Glover et al. (2015)

Table S1. Attribute features of the decision tree from Seillé & Visser (2020)

$\|\beta\|$	λ	$\mathrm{Log}(\|Z_{xy} - Z_{yx}\|)$
$\|\beta\| < 2$	$\lambda < 0.1$	$\mathrm{Log}(\|Z_{xy} - Z_{yx}\|) < 0.1$
$2 < \|\beta\| < 3$	$0.1 < \lambda < 0.2$	$0.1 < \mathrm{Log}(\|Z_{xy} - Z_{yx}\|) < 0.3$
$3 < \|\beta\| < 5$	$0.2 < \lambda < 0.3$	$0.3 < \mathrm{Log}(\|Z_{xy} - Z_{yx}\|) < 0.5$
$5 < \|\beta\| < 7$	$0.3 < \lambda < 0.4$	$\mathrm{Log}(\|Z_{xy} - Z_{yx}\|) > 0.5$
$7 < \|\beta\| < 9$	$0.4 < \lambda < 0.5$	–
$\|\beta\| > 9$	$0.5 < \lambda < 0.75$	–
–	$\lambda > 0.75$	–

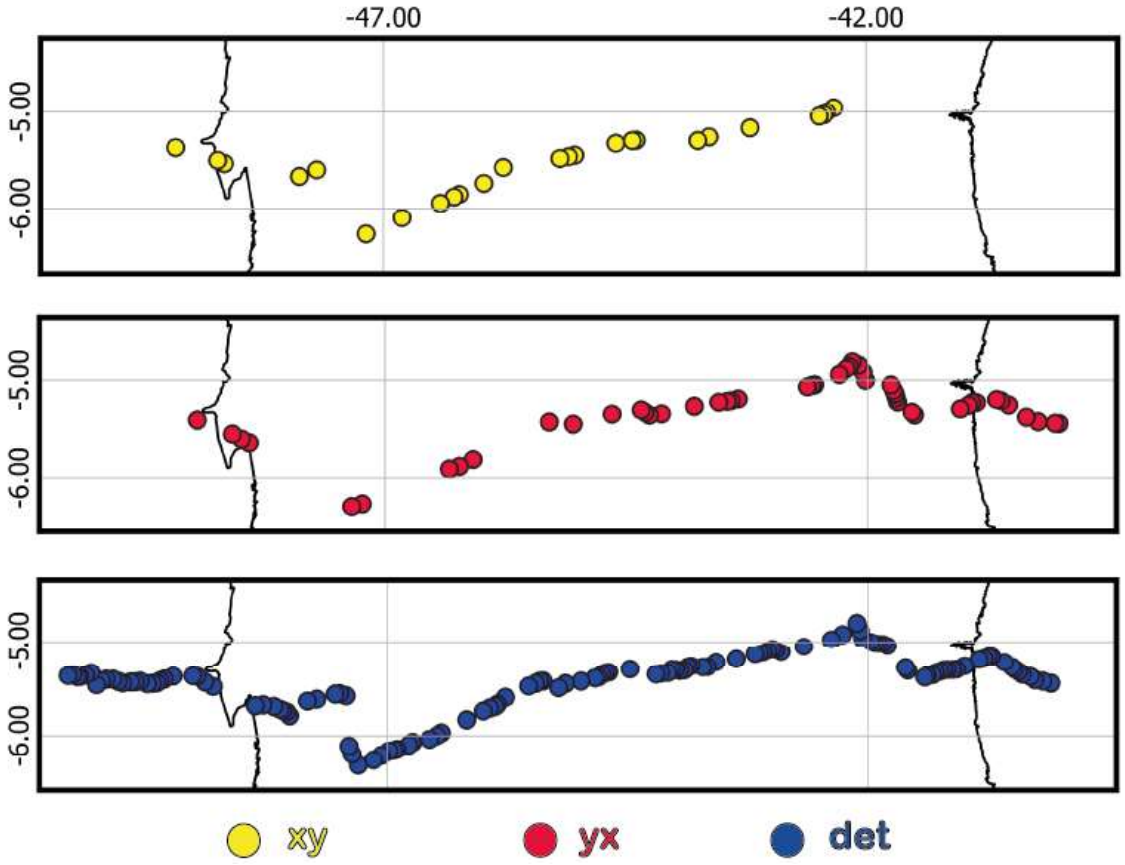


Figure S3. Distribution of the MT soundings, indicating the polarization selected for each station based on data quality.

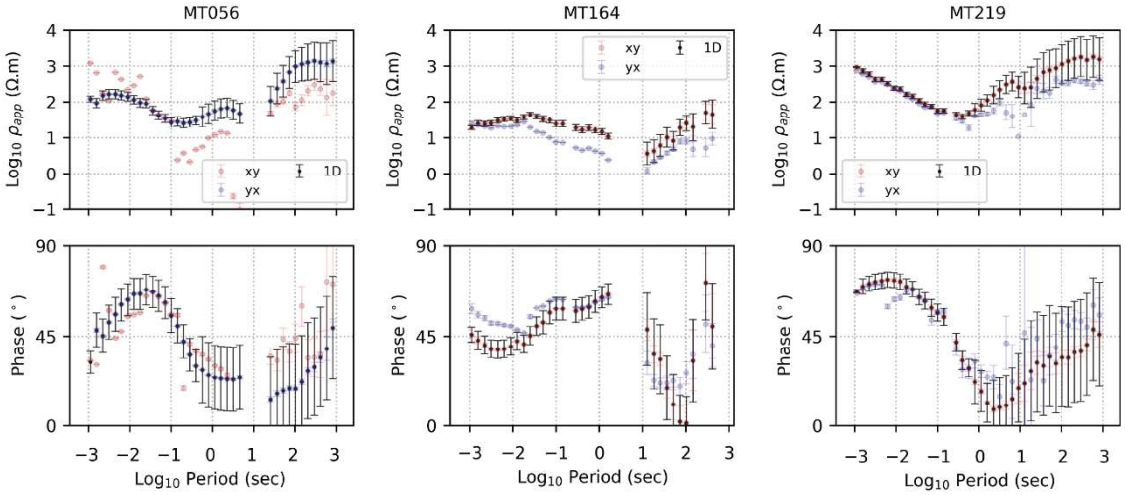


Figure S4. Apparent resistivity and phase curves, in which one of the two polarizations is used. These station are located near those described in section 4.2 of the main text.

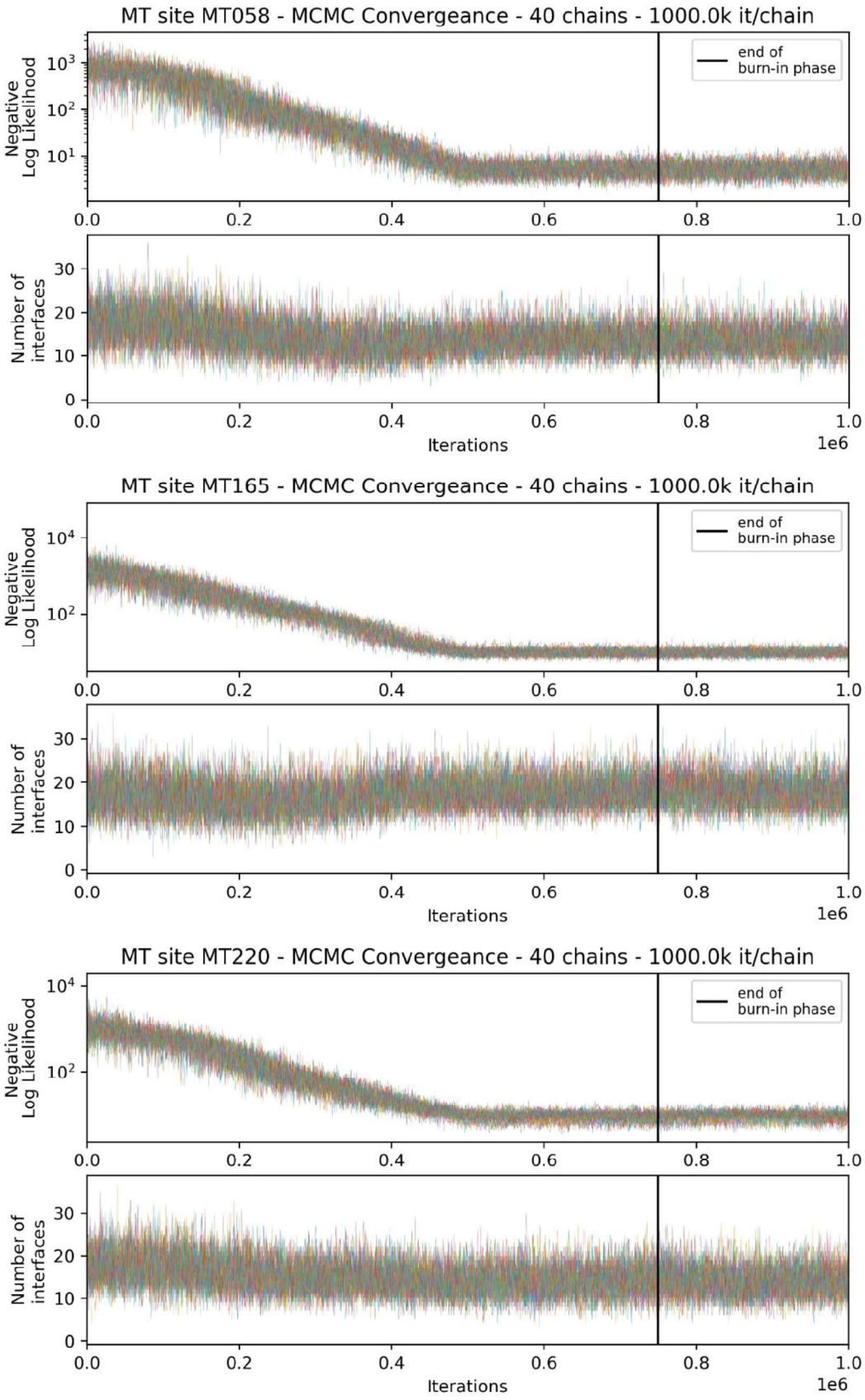


Figure S5. Convergence of stations MT059, MT148 and MT220 discussed in section 4.3.1 of the main text

Table S2. Depth of the geological units identified in the four wells.

		Well depth log (in metres)			
Group	**Formation**	**NGST**	**2BAC**	**2ISZST**	**1PD**
	Codo		102	27	3
	Grajaú	4			
	Corda	14	277		115
	Mosquito	31		55	
Balsas	Sambaiba	159	383	273	190
	Motuca	552	580	705	440
	Pedra de Fogo	781	808	895	647
	Piaui	976	1040	1065	865
	Poti	1276	1348	1282	1157
	Longá	1470	1583	1434	1380
Canindé	Cabecas	1612	1794	1565	1645
	Pimenteiras	1702	1912	1654	1919
	Itam	2235	2561	1835	2366
Serra Grande	Jaicos	2372	2748	1971	2515
	Tianguá	2557	2967	2094	2745
	Ipu		3101		
	Basement		3228	2150	

Reference

Glover, P.W.J., 2015. Geophysical properties of the near surface earth: Electrical properties. In: Schubert, G. (Ed.), *Treatise on Geophysics*, 2nd ed., Vol. 11. Elsevier, pp. 89–137.

Klöcking, M., White, N., & MacLennan, J., 2018. Role of basaltic magmatism within the Parnaíba cratonic basin, NE Brazil.

Seillé, H., & Visser, G., 2020. Bayesian inversion of magnetotelluric data considering dimensionality discrepancies. *Geophysical Journal International*, 223(3), 1565–1583. https://doi.org/10.1093/gji/ggaa391

Chapter 6

Discussion, conclusion and future work

The results presented in the previous chapters have significantly contributed to a better understanding of the geodynamic mechanisms and processes that led to the present-day configuration of the Parnaíba Basin.

In the following discussion, the results obtained at both crustal and shallow scales are jointly compared and analyzed, with the aim of evaluating the consistency between the different methodological approaches employed. This comparison highlights the validity, complementarity, and advantages of each methodology applied to the study of the Parnaíba Basin, as well as their respective limitations in subsurface characterization.

6.1 3D deterministic and 1D probabilistic models

In order to discuss and analyze the differences between the model derived in this study and the resistivity models obtained from the 3D MT inversion performed by Romero-Beltran et al. (2025). Figure 6.1 shows cross-sections of both models for the central part of the basin, displayed using the same depth and resistivity scales. Although this comparison cannot be considered strictly direct, as the models were developed to address different modelling objectives, it still allows several important conclusions to be drawn. In the 3D model, the mesh discretization employed a cell size of 1500 m in the north and east directions, and an initial vertical cell thickness of 25 m, with cell sizes increasing with depth. In contrast, our model focuses on the uppermost part of the subsurface but achieves substantially higher resolution, using cells of 200 m $\times$ 200 m $\times$ 5 m in the north, east, and vertical directions, respectively, with a constant vertical discretization.

The regularization applied in the 3D inversion enforces strong smoothness constraints, which hampers the identification of sharp boundaries between sediments and basement (Figure 6.1a). By contrast, the 1D model exhibits a better resistivity contrast and a more sharply defined interface between these units (Figure 6.1b). However, the main discrepancy between the two approaches becomes evident in the deeper part of the basin, where a highly conductive unit is present. Both models identified the low resistivity features (< 10 Ωm), but in the 1D bayesian model, this conductive layer is characterized by a relatively uniform thickness of approximately 1 km. In contrast, the 3D model depicts this unit as laterally heterogeneous and locally discontinuous, reflecting differences in resolution, regularization, and model parameterization between the two approaches.

Although deterministic 3D MT inversion models are often affected by intrinsic non-uniqueness. Previous studies have shown that inversion parameters, particularly the resistivity assigned to the initial or prior model, can strongly influence the final solution Robertson et al. (2020). Thus, Bayesian results can be used to define more informed starting models for deterministic inversions, thereby reducing bias and improving the robustness of the solutions (Chen et al., 2008)

In this framework, the results presented here, while not providing direct estimates of resistivity, offer independent constraints that can be used to validate geological interpretations and to guide the definition of initial models for 2D and 3D MT inversions.

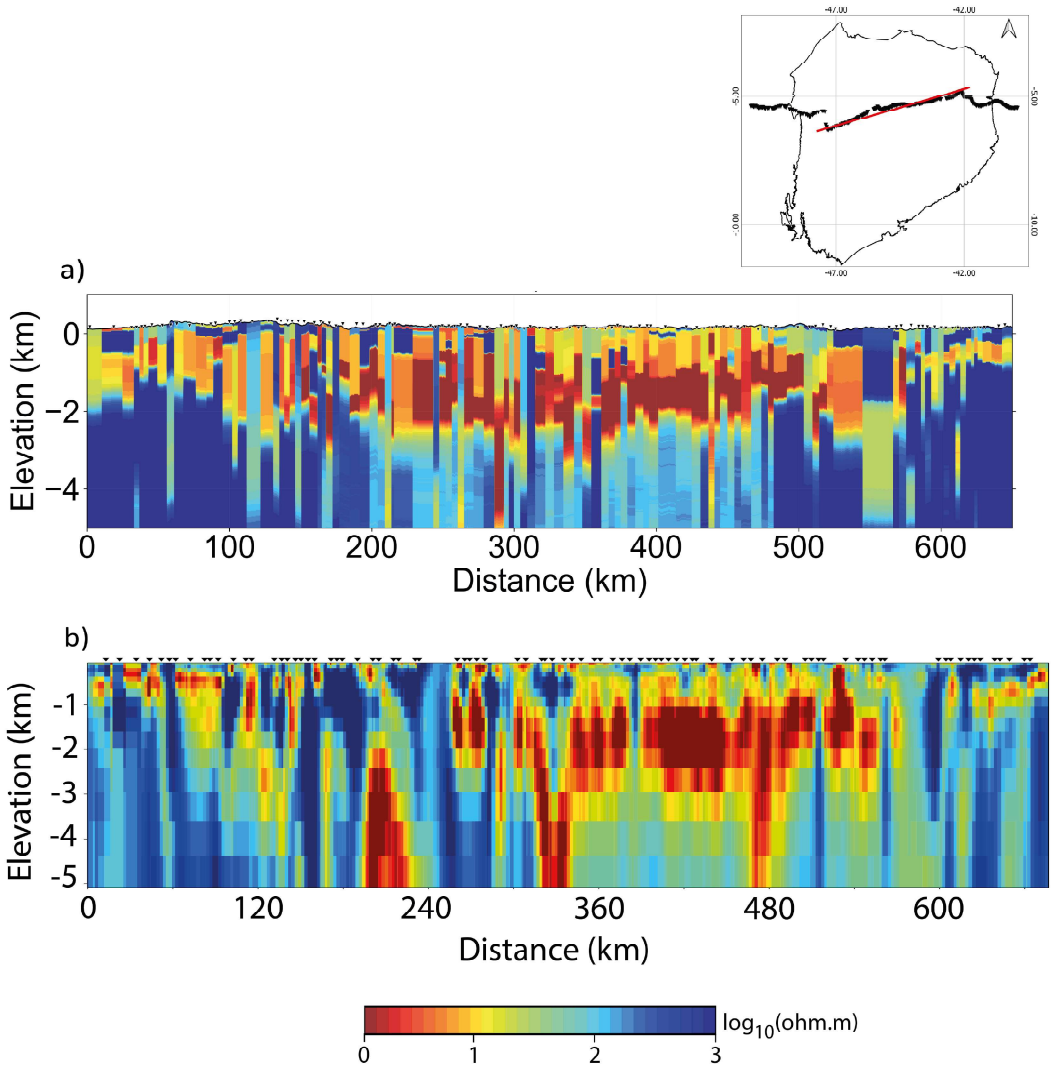


Figure 6.1: Comparison between the resistivity model obtained from the 1D Bayesian inversion performed in this study (a) and the 3D inversion presented by Romero-Beltran et al. (2025) (b). Both vertical cross-sections correspond exclusively to the central part of the basin, along the red line shown in the reference map in the upper right.

6.2 Conclusion

This study provided a new geophysical and geological insights into the structure and evolution of the Parnaíba Basin through the integration of 3D deterministic inversion and 1D probabilistic Bayesian inversion. The main contributions are:

The combination of 3-D deterministic MT inversion with probabilistic Bayesian approaches provides a comprehensive framework to investigate the deep and shallow structure basin architecture, improving model robustness and reducing interpretation uncertainty.

The magnetotelluric (MT) models reaffirm the presence of lateral heterogeneities at crust and the upper mantle depths, associated with the juxtaposition of the main tectonic domains: the Amazonian Craton, the Parnaíba Block, and the Borborema Province. This observation is consistent with the identification of theses tectonic units and the crustal boundaries between these blocks, previously identified from DSR data (Daly et al., 2014), WARR data (Soares et al., 2018), and MT data (Solon et al., 2018)..

The resistivity contrast between the Grajaú and Teresina domains demonstrates that the Parnaíba Block is tectonically heterogeneous rather than a stable cratonic unit. The Grajaú domain preserves a more resistive signature linked to limited magmatic reworking, whereas the Teresina domain reflects stronger magmatic and post-collisional modification, consistent with seismic and potential field observations. This interpretation is consistent with the enhanced conductivity observed in the crust and upper mantle beneath the Parnaíba Basin (Padilha et al., 2015), where this behavior is directly related to these geological events.

A conductive anomaly between the Grajaú and Teresina domains is interpreted as a paleofossil suture zone, providing important constraints on regional tectonics and supporting an eastward subduction polarity during the Paleoproterozoic.

The MT results support a geodynamic model in which the Parnaíba Basin formed through the amalgamation of allochthonous terranes, followed by magmatic reworking (Oliveira et al. (2018); (Heilbron et al., 2018)) and long-lived mechanical subsidence (Tozer et al. (2017), Daly et al. (2018). However, the absence of clear evidence for lithospheric stretching has led to alternative models, including lithospheric heating associated with crustal thickening followed by thermal contraction (McKenzie and Rodríguez Tribaldos (2018)). These contrasting interpretations highlight that

the mechanisms driving subsidence in the basin remain debated and require further investigation.

The Parnaíba Basin developed over a complex orogenic system, formed by successive collisions between different continental blocks and their interaction with oceanic domains of varying ages (Schmitt et al. (2018), Caxito et al. (2020)). These results are consistent with the idea that most of these tectonic systems evolved following a Wilson cycle (Daly et al., 2019).

The probabilistic inversion enhances near-surface resolution, allowing a more reliable definition of the sediment–basement interface, and interface and the identification of a conductive layer associated with the Poti and Cabeças formations. These features are linked to hydrocarbon-bearing zones in the central basin, highlighting the relevance of the proposed methodology for resource exploration, particularly given that the Parnaíba basin accounts for approximately 5% of Brazil's onshore hydrocarbon production (Abelha et al., 2018).

6.3 Future Work

The results presented in this thesis demonstrate that the integration of deterministic 3D magnetotelluric inversion with probabilistic 1D Bayesian approaches provides a robust framework to investigate both the deep and shallow structure of the Parnaíba Basin. While the 3D inversion captures large-scale electrical heterogeneities associated with major tectonic domains, the probabilistic 1D inversion enhances the resolution of near-surface structures and provides a quantitative assessment of uncertainty.

Despite these advances, several methodological and data-related limitations remain. Addressing these limitations represents a critical step toward improving the reliability of the electrical models and strengthening the geological interpretations derived from them. The following sections outline specific directions for future research, directly motivated by the results and constraints identified in this study.

One of the main limitations identified in this study is the reduced data quality in the central portion of the basin, where electromagnetic noise significantly limits the usable period range, often restricting it to approximately 10–100 seconds. This limitation directly affects the ability to resolve deeper structures in the region where sedimentary thickness is greatest.

Future work should prioritize advanced reprocessing strategies to improve data quality in these areas. In particular, the application of remote reference techniques, using high-quality magnetic field recordings from stations located at the basin margins, could significantly enhance the signal-to-noise ratio. Additionally, robust statistical estimators, could be employed to reduce the influence of outliers and improve the stability of the transfer function estimates. Complementary to reprocessing efforts, the acquisition of new long-period magnetotelluric data in the central basin would be highly beneficial, allowing for improved imaging of the lower crust and upper mantle.

The Bayesian Ensemble Fusion (BEF) approach applied in this study has proven effective for mapping the sediment–basement interface by integrating 1D probabilistic inversion results with borehole and geological data. Nevertheless, the current implementation assumes lateral independence between individual soundings.

Future developments should aim to incorporate spatial correlations into the BEF framework, allowing for the construction of fully three-dimensional probabilistic models of subsurface interfaces. This would improve the continuity and geological realism of the reconstructed surfaces and enable the identification of structural features such as faults and basement highs with greater confidence.Furthermore, extending the BEF methodology to deeper interfaces, including intra-crustal boundaries and the Moho, represents a promising direction for future research.

Although comparisons with seismic and gravity data were performed, the integration remains largely qualitative. Future work should aim to develop quantitative joint or cooperative inversion approaches that combine magnetotelluric data with other geophysical datasets (Moorkamp et al., 2011). Such integration is particularly important in regions affected by magmatic intrusions, where individual geophysical methods may have limited resolution. Joint interpretation frameworks can help reduce ambiguity and provide a more consistent model of subsurface structure.

Bibliography

Abelha, M., Petersohn, E., Bastos, G., and Araújo, D. (2018). New insights into the Parnaíba Basin: Results of investments by the Brazilian National Petroleum Agency. *Geological Society, London, Special Publications*, 472:SP472.13.

Ardid Segura, A., Dempsey, D., Bertrand, E., Sepulveda, F., Solon, F., Tarits, P., and Archer, R. (2021). Bayesian magnetotelluric inversion using methylene blue structural priors for imaging shallow conductors in geothermal fields. *Geophysics*, 86:1–66.

Assis, A. P., Porto, A. L., Schmitt, R. S., Linol, B., Medeiros, S. R., Correa Martins, F., and Silva, D. S. (2019). The Ordovician-Silurian tectonostratigraphic evolution and paleogeography of eastern Parnaiba Basin, NE Brazil. *Journal of South American Earth Sciences*, 95:102241.

Bahr, K. (1988). Interpretadon of the magnetotelluric impedance tensor: regional induction and local telluric distortion. *Journal Geophys.*, 62:119–127.

Baksi, A. K. and Archibald, D. (1997). Mesozoic igneous activity in the maranha˜o province, northern brazil: 40ar/ 39ar evidence for separate episodes of basaltic magmatism. *Earth and Planetary Science Letters*, 151(3):139–153.

Brito Neves, B., Fuck, R., Cordani, U., and Thomaz F°, A. (1984). Influence of basement structures on the evolution of the major sedimentary basins of brazil: A case of tectonic heritage. *Journal of Geodynamics*, 1(3):495–510. Precambrian crustal evolution.

Brodie, R. and Jiang, W. (2018). Trans-dimensional monte carlo inversion of short period magnetotelluric data for cover thickness estimation. *ASEG Extended Abstracts*, 2018:1.

Cagniard, L. (1953). Basic Theory of the magneto-telluric method of geophisical prospecting. *Geophysics*, 18(3):605–635.

Caldwell, T. G., Bibby, H. M., and Brown, C. (2004). The magnetotelluric phase tensor. *Geophysical Journal International*, 158(2):457–469.

Campanyá, J. (2013). *Innovation of the Magnetotelluric method and its application to the characterization of the Pyrenean lithosphere*. Tese de D.Sc., Departamento de Geodinámica i Geofísica - Universitat de Barcelona, Barcelona, Spain.

Castro, D., Bezerra, F., Fuck, R., and Vidotti, R. (2016). Geophysical evidence of pre-sag rifting and post-rifting fault reactivation in the parnaíba basin, brazil. *Solid Earth*, 7:529–548.

Caxito, F.d., A. F. (2023). The role of v-shaped oceans and ribbon continents in the brasiliano/panafrican assembly of western gondwana. *Sci Rep*, 13:1568.

Caxito, F. d. A., Santos, L. C. M. d. L., Ganade, C. E., Bendaoud, A., Fettous, E.-H., and Bouyo, M. H. (2020). Toward an integrated model of geological evolution for ne brazil-nw africa: The borborema province and its connections to the trans-saharan (benino-nigerian and tuareg shields) and central african orogens. *Brazilian Journal of Geology*, 50(02):e20190122.

Chave, A. and Jones, A., editors (2012). *The Magnetotelluric Method: Theory and Practice*. Cambridge University Press.

Chave, A. D. and Thomson, D. J. (1989). Some comments on magnetotelluric response function estimation. *Journal of Geophysical Research*, 94:14215–14225.

Chave, A. D. and Thomson, D. J. (2004). Bounded influence magnetotelluric response function estimation. *Geophysical Journal International*, 157(3):988–1006.

Chave, A. D. and Weidelt, P. (2012). *The theoretical basis for electromagnetic induction*, page 19–49. Cambridge University Press.

Chen, J., Hoversten, G. M., Key, K., Nordquist, G., and Cumming, W. (2012). Stochastic inversion of magnetotelluric data using a sharp boundary parameterization and application to a geothermal site. *GEOPHYSICS*, 77(4):E265–E279.

Chen, J., Kemna, A., and Hubbard, S. S. (2008). A comparison between gauss-newton and markov-chain monte carlo–based methods for inverting spectral induced-polarization data for cole-cole parameters. *Geophysics*, 73(6):F247–F259.

Cherevatova, M., Smirnov, M., Korja, T., Pedersen, L., Ebbing, J., Gradmann, S., and Becken, M. (2015). Electrical conductivity structure of north-west fennoscandia from three-dimensional inversion of magnetotelluric data. *Tectonophysics*, 653:20–32.

Conway, D., Simpson, J., Didana, Y., Rugari, J., and Heinson, G. (2018). Probabilistic magnetotelluric inversion with adaptive regularisation using the no-u-turns sampler. *Pure and Applied Geophysics*, 175.

Cordani, U. G., Brito Neves, B. B. d., Fuck, R. A., Porto, R., Thomaz Filho, A., and Cunha, F. M. B. (1984). Estudo preliminar de integração do pré-cambriano com os eventos tectônicos das bacias sedimentares brasileiras. *Ciência. Técnica. Petróleo. Seção: exploração de petróleo.*

Cordani, U. G., Brito Neves, B. B. d., and Thomaz Filho, A. (2009). Estudo preliminar de integração do pré-cambriano com os eventos tectônicos das bacias sedimentares brasileiras (atualização). *Boletim de Geociências da Petrobrás.*

Cordani, U. G., Pimentel, M. M., Ganade De Araújo, C. E., Basei, M. A. S., Fuck, R. A., and Girardi, V. A. V. (2013). Was there an ediacaran clymene ocean in central south america? *American Journal of Science*, 313(6):517–539.

Daly, M. C., Andrade, V., Barousse, C. A., Costa, R., McDowell, K., Piggott, N., and Poole, A. J. (2014). Brasiliano crustal structure and the tectonic setting of the Parnaíba basin of NE Brazil: Results of a deep seismic reflection profile. *Tectonics*, 33(11):2102–2120.

Daly, M. C., Fuck, R. A., Julià, J., Macdonald, D. I. M., and Watts, A. B. (2018). Cratonic basin formation: a case study of the parnaíba basin of brazil. In *Cratonic Basin Formation: A Case Study of the Parnaíba Basin of Brazil.* Geological Society of London.

Daly, M. C., Tozer, B., and Watts, A. B. (2019). Cratonic basins and the wilson cycle: a perspective from the parnaíba basin, brazil. *Geological Society, London, Special Publications*, 470(1):463–477.

de Castro, D. L., Fuck, R. A., Phillips, J. D., Vidotti, R. M., Bezerra, F. H., and Dantas, E. L. (2014). Crustal structure beneath the paleozoic parnaíba basin revealed by airborne gravity and magnetic data, brazil. *Tectonophysics*, 614:128–145.

De Castro, D. L., Fuck, R. A., Phillips, J. D., Vidotti, R. M., Bezerra, F. H., and Dantas, E. L. (2014). Crustal structure beneath the paleozoic parnaíba basin revealed by airborne gravity and magnetic data, brazil. *Tectonophysics*, 614:128–145.

de Wit, M. J., Stankiewicz, J., and Reeves, C. (2008). Restoring pan-african-brasiliano connections: more gondwana control, less trans-atlantic corruption. *Geological Society, London, Special Publications*, 294(1):399–412.

Delgadillo, F. (2019). *Determinación estable del rumbo magnetotelúrico utilizando los criterios de fórmulas analíticas*. Msc. thesis, CICESE, Mexico.

Egbert, G. D. and Booker, J. R. (1986). Robust estimation of geomagnetic transfer functions. *Geophysical Journal International*, 87(1):173–194.

Feng, M., Lee, S., and Assumpcao, M. (2007). Upper mantle structure of south america from joint inversion of waveforms and fundamental mode group velocities of rayleigh waves. *Journal of Geophysical Research*, 112.

Filho, A., Mizusaki, A., and Antonioli, L. (2008a). Magmatismo nas bacias sedimentares brasileiras e sua influência na geologia do petróleo. *Rev. Bras. Geoc.*, 38.

Filho, A., Nizuzaki, A., Milani, E., and CESERO, P. (2008b). Rifting and magmatism associated with the south america and africa breakup. *Brazilian Journal of Geology*, 30.

Fuck, R. A., Dantas, E. L., Pimentel, M. M., Botelho, N. F., Armstrong, R., Laux, J. H., Junges, S. L., Soares, J. E., and Praxedes, I. F. (2014). Paleoproterozoic crust-formation and reworking events in the tocantins province, central brazil: A contribution for atlantica supercontinent reconstruction. *Precambrian Research*, 244:53–74. Precambrian Supercontinents.

Garcia, X., Julià, J., Nemocón, A. M., and Neukirch, M. (2019). Lithospheric thinning under the Araripe Basin (NE Brazil) from a long-period magnetotelluric survey: Constraints for tectonic inversion. *Gondwana Research*, 68:174–184.

Goés, A. and Feijó, F. (1994). Bacia do parnaíba. *Boletim de Geociências Petrobrás*, (8):57–67.

Groom, R. W. and Bailey, R. C. (1989). Decomposition of magnetotelluric impedance tensors in the presence of local three-dimensional galvanic distortion. *Journal of Geophysical Research: Solid Earth*, 94(B2):1913–1925.

Góes, A., Souza, J., and Teixeira, L. (1990). Estágio exploratório e perspectivas petrolíferas da bacia do parnaíba. *Boletim de Geociências da Petrobrás*, (4(1)):55–64.

Góes, A. M. (1995). *Formação Poti (Carbonífero inferior) da Bacia do Parnaiba*. Phd thesis, Instituto de Geociências, Universidade de São Paulo, São Paulo, Brasil.

Heilbron, M., Guedes, E., Mane, M., Valeriano, C. d. M., Tupinambá, M., Almeida, J., Silva, L. G. d. E., Paschoal Duarte, B., Favera, J. C. D., and Viana, A. (2018). Geochemical and temporal provinciality of the magmatism of the eastern parnaíba basin, ne brazil. *Geological Society, London, Special Publications*, 472(1):251–278.

Kelbert, A., Meqbel, N., Egbert, G., and Tandon, K. (2014). ModEM: A modular system for inversion of electromagnetic geophysical data. *Computers & Geosciences*, 66:40–53.

Larsen, J. C., Mackie, R. L., Manzella, A., Fiordelisi, A., and Rieven, S. (1996). Robust smooth magnetotelluric transfer functions. *Geophysical Journal International*, 124(3):801–819.

Li, Z., Bogdanova, S., Collins, A., Davidson, A., De Waele, B., Ernst, R., Fitzsimons, I., Fuck, R., Gladkochub, D., Jacobs, J., Karlstrom, K., Lu, S., Natapov, L., Pease, V., Pisarevsky, S., Thrane, K., and Vernikovsky, V. (2008). Assembly, configuration, and break-up history of rodinia: A synthesis. *Precambrian Research*, 160(1):179–210. Testing the Rodinia Hypothesis: Records in its Building Blocks.

Manasero, M. (2019). *A Reduced Order Approach for Probabilistic Inversions of 3D Magnetotelluric Data*. Phd thesis, Department of Earth and Environmental Sciences - Macquarie University, Sydney-Australia,.

Manassero, C., Afonso, J., Zyserman, F., Zlotnik, S., and Fomin, I. (2020). A reduced order approach for probabilistic inversions of 3d magnetotelluric data i: General formulation. *Geophysical Journal International*.

Martí, A., Queralt, P., and Ledo, J. (2013). WALDIM: A code for the dimensionality analysis of magnetotelluric data using the rotational invariants of the magnetotelluric tensor. *Computers & Geosciences*, pages 2295–2303.

McKenzie, D. and Rodríguez Tribaldos, V. (2018). Lithospheric heating by crustal thickening: a possible origin of the Parnaíba Basin. In *Cratonic Basin*

Formation: A Case Study of the Parnaíba Basin of Brazil. Geological Society of London.

Mcneice, G. and Jones, A. (2001). Multisite, multifrequency tensor decomposition of magnetotelluric data. *Geophysics*, 66:158–173.

Moorkamp, M., Heincke, B., Jegen, M., Roberts, A. W., and Hobbs, R. W. (2011). A framework for 3-d joint inversion of mt, gravity and seismic data. *Geophysical Journal International*, 187(2):505–522.

Newman, G. A. and Alumbaugh, D. L. (2000). Three-dimensional magnetotelluric inversion using non-linear conjugate gradients. *Geophysical Journal International*, 140(2):410–424.

Ngwira, C. M. and Pulkkinen, A. A. (2019). *An Introduction to Geomagnetically Induced Currents*, chapter 1, pages 1–13. American Geophysical Union (AGU).

Oliveira, A. L., Pimentel, M. M., Fuck, R. A., and Oliveira, D. C. (2018). Petrology of jurassic and cretaceous basaltic formations from the parnaíba basin, ne brazil: correlations and associations with large igneous provinces.

Oriolo, S., Oyhantçabal, P., Wemmer, K., and Siegesmund, S. (2017). Contemporaneous assembly of western gondwana and final rodinia break-up: Implications for the supercontinent cycle. *Geoscience Frontiers*, 8(6):1431–1445.

Padilha, A. L., Vitorello, Í., Antunes, C. E., and Pádua, M. B. (2015). Imaging three-dimensional crustal conductivity structures reflecting continental flood basalt effects hidden beneath thick intracratonic sedimentary basin. *Journal of Geophysical Research: Solid Earth*, 120(7):4702–4719.

Patro, P. and Egbert, G. (2011). Application of 3d inversion to magnetotelluric profile data from the deccan volcanic province of western india. *Physics of The Earth and Planetary Interiors - PHYS EARTH PLANET INTERIORS*, 187:33–46.

Porto, A. (2021). *The Neoproterozoic-Early Paleozoic Tectonic Evolution of the Northeast of Brasil: An Integrated Geological-Geophysical Analysis of the Pre-Silurian Basement of Parnaíba Basin*. Phd thesis, Post-Graduated Departament of Geophysics, Nacional Observatory, Rio de Janeiro, Brasil.

Porto, A., Carvalho, C., Lima, C., Heilbron, M., Caxito, F., La Terra, E., and Fontes, S. L. (2022). The neoproterozoic basement of the parnaíba basin

(ne brazil) from combined geophysical-geological analysis: A missing piece of the western gondwana puzzle. *Precambrian Research*, 379:106784.

Rikitake, T. (1948). Notes on electromagnetic induction within the Earth. *Bull. Earthquake Res. Inst.*, 24:1–9.

Robertson, K., Thiel, S., and Meqbel, N. (2020). Quality over quantity: on workflow and model space exploration of 3d inversion of mt data. *Earth, Planets and Space*, 72(1):2.

Romero-Beltran, G., La Terra, E. F., Panetto, L. P., and Seillé, H. (2025). Magnetotelluric imaging of the parnaíba basin: Implications to the west gondwana formation. *Tectonophysics*, 909:230777.

Rosas-Carbajal, M. (2014). *Time-lapse and probabilistic inversion strategies for plane-wave electromagnetic data*. These de doctorat, Faculté des géosciences et de l'environnement Institut des Sciences de la Terre - Université de Lausanne, Laussane, Switzerland.

Rosas-Carbajal, M., Linde, N., Kalscheuer, T., and Vrugt, J. (2014). Two-dimensional probabilistic inversion of plane-wave electromagnetic data: Methodology, model constraints and joint inversion with electrical resistivity data. *Geophysical Journal International*, 196:1508–1524.

Rosas-Carbajal, M., Linde, N., Peacock, J., Zyserman, F., Kalscheuer, T., and Thiel, S. (2015). Probabilistic 3-d time-lapse inversion of magnetotelluric data: Application to an enhanced geothermal system. *Geophysical Journal International*, 203:1946–1960.

Scalzo, R., Kohn, D., Olierook, H., Houseman, G., Chandra, R., Girolami, M., and Cripps, S. (2019). Efficiency and robustness in monte carlo sampling for 3-d geophysical inversions with obsidian v0.1.2: setting up for success. *Geoscientific Model Development*, 12(7):2941–2960.

Schiffer, C., de Lima, M. V., Soares, J. E., Stephenson, R., de Araújo, V. C., Lima, F. T., Rocha, F. A., Trindade, C. R., and Fuck, R. A. (2021). Vp/vs ratios in the parnaíba basin from joint active-passive seismic analysis – implications for continental amalgamation and basin formation. *Tectonophysics*, 801:228715.

Schmitt, R., Trouw, R. A., Silva, E., de Jesus, J. V., Da Costa, L. F., and Passarelli, C. (2023). The role of crustal scale shear zones in southwest gondwana consolidation - transatlantic correlation. *Geological Society, London, Special Publications*, 531.

Schmitt, R. d. S., Fragoso, R. d. A., and Collins, A. S. (2018). Suturing gondwana in the cambrian: the orogenic events of the final amalgamation. In *Geology of southwest Gondwana*, pages 411–432. Springer.

Seillé, H., Thiel, S., Brand, K., Mulè, S., Visser, G., Fabris, A., and Munday, T. (2024). Bayesian fusion of mt and aem probabilistic models with geological data: examples from the eastern gawler craton, south australia. *Exploration Geophysics*, 55(Special Issue: Lithospheric to deposit scale magnetotellurics advancements, including AusLAMP in Australia):486–505.

Seillé, H. and Visser, G. (2020). Bayesian inversion of magnetotelluric data considering dimensionality discrepancies. *Geophysical Journal International*, 223(3):1565–1583.

Simpson, F. and Bahr, K. (2005). Practical Magnetotellurics.

Siripunvaraporn, W. and Egbert, G. (2000). An efficient data-subspace inversion method for 2-d magnetotelluric data. *GEOPHYSICS*, 65(3):791–803.

Siripunvaraporn, W. and Egbert, G. (2009). Wsinv3dmt: Vertical magnetic field transfer function inversion and parallel implementation. *Physics of the Earth and Planetary Interiors*, 173(3):317–329.

Siripunvaraporn, W., Egbert, G., Lenbury, Y., and Uyeshima, M. (2005). Three-dimensional magnetotelluric inversion: data-space method. *Physics of the Earth and Planetary Interiors*, 150(1):3–14. Electromagnetic Induction in the Earth.

Siripunvaraporn, W., Egbert, G., and Uyeshima, M. (2005). Interpretation of two-dimensional magnetotelluric profile data with three-dimensional inversion: synthetic examples. *Geophysical Journal International*, 160(3):804–814.

Smaï, F. and Wawrzyniak, P. (2020). Razorback, an open source python library for robust processing of magnetotelluric data. *Frontiers in Earth Science*, 8:296.

Soares, J. E. P., Stephenson, R., Fuck, R. A., de Lima, M. V. A. G., de Araújo, V. C. M., Lima, F. T., Rocha, F. A. S., and da Trindade, C. R. (2018). Structure of the crust and upper mantle beneath the Parnaíba Basin, Brazil, from wide-angle reflection–refraction data. *Geological Society, London, Special Publications*, 472(1):67–82.

Solon, F. F., Fontes, S. L., and La Terra, E. F. (2018). Electrical conductivity structure across the Parnaíba Basin, NE Brazil. *Geological Society, London, Special Publications*, 472(1):109–126.

Tarantola, A. (2005). Inverse problem theory and methods for model parameter estimation. *SIAM*, page 50 p.

Tarantola, A. and Valette, B. (1981). Inverse problems = quest for information. *Journal of Geophysics*, 50(1):159–170.

Tikhonov, A. (1950). On investigation of electrical characteristics of the deep layers of the earth's crust. *Dokl. Akad. Nauk SSSR*, 73:295–297.

Torsvik, T. H. and Cocks, L. R. M. (2013). Gondwana from top to base in space and time. *Gondwana Research*, 24(3):999–1030.

Torsvik, T. H., Van der Voo, R., Preeden, U., Mac Niocaill, C., Steinberger, B., Doubrovine, P. V., van Hinsbergen, D. J., Domeier, M., Gaina, C., Tohver, E., Meert, J. G., McCausland, P. J., and Cocks, L. R. M. (2012). Phanerozoic polar wander, palaeogeography and dynamics. *Earth-Science Reviews*, 114(3):325–368.

Tozer, B., Watts, A. B., and Daly, M. C. (2017). Crustal structure, gravity anomalies, and subsidence history of the parnaíba cratonic basin, northeast brazil. *Journal of Geophysical Research: Solid Earth*, 122(7):5591–5621.

Unsworth, M. (2007). *Magnetotellurics*, pages 670–673. Springer, Berlin, Germany, 1 edition.

Van Leeuwen, W. A. (2016). *Geothermal exploration using the magnetotelluric method*. Department of Earth Sciences. Faculty of Geosciences - Utrecht University, Netherlands.

Vaz, P., Rezende, V., Wanderley Filho, J., and Travassos, W. (2007). Bacia do parnaíba. *Boletim de Geociências da Petrobrás*, (15):253–263.

Visser, G. and Markov, J. (2019). Cover thickness uncertainty mapping using bayesian estimate fusion: leveraging domain knowledge. *Geophysical Journal International*, 219(3):1474–1490.

Vozoff, K. (1991). The magnetotelluric method, in electromagnetic methods in applied geophysics. *Society of Exploration Geophysics, Tulsa, OK*, chap. 8.

Weaver, J. T., Agarwal, A. K., and Lilley, F. E. M. (2000). Characterization of the magnetotelluric tensor in terms of its invariants. *Geophysical Journal International*, 141(2):321–336.

Zhdanov, M. (2018). Chapter 13 - magnetotelluric and magnetovariational methods. In Zhdanov, M., editor, *Foundations of Geophysical Electromagnetic Theory and Methods (Second Edition)*, pages 495–584. Elsevier, second edition edition.

Zhdanov, M., Dmitriev, V., Fang, S., and Hursan, G. (2000). Quasi-analytical approximation and series in 3d electromagnetic modeling. *Geophysics*, 65:1746–1757.